Master thesis and internship[BR]- Master's thesis : A Wall Model for LES of Flows with Laminar-Turbulent Transition[BR]- Integration Internship : TU Delft

Auteur : Dujardin, Nicolas
Promoteur(s) : Terrapon, Vincent
Faculté : Faculté des Sciences appliquées
Diplôme : Master en ingénieur civil en aérospatiale, à finalité spécialisée en "aerospace engineering"
Année académique : 2022-2023
URI/URL : http://hdl.handle.net/2268.2/18179

University of Liège
Faculty of Applied Sciences
Academic Year 2022-2023

A Wall Model for LES of Flows with Laminar-Turbulent Transition

Master thesis submitted to the department of aerospace and mechanical engineering of the University of Liège in partial fulfillment of the requirements for the degree of Master in Aerospace Engineering

Author:	Nicolas Dujardin	
Thesis Supervisors:	Prof. Vincent E. Terrapon	Uliège (promoter)
	Prof. Stefan Hickel	TU Delft

Research project conducted within the Faculty of Aerospace Engineering of Technische Universiteit Delft

Abstract

Large Eddy Simulations (LES) offer a better reliability than the Reynolds-Averaged Navier-Stokes method and a more acceptable computational cost compared to Direct Numerical Simulations. Nevertheless, with such an approach, wall-bounded flows at high Reynolds numbers require an excessively fine mesh resolution to fully resolve the energetic turbulent structures within the inner boundary layer. Consequently, the related computational cost is a major obstacle for most practical engineering settings. To overcome this, Wall-Modeled Large Eddy Simulations (WMLES) estimate instead of resolve the effect of the inner layer. Considering the wall-stress modeling approach, this is achieved by providing the wall-shear stress as a Neumann boundary condition and enforcing the impermeability instead of imposing a no-slip condition over the wall. In this context, a wall-stress model is built for incompressible flows including laminar-turbulent transition. As a first step, a laminar wall model (LWM) is established by assuming a self-similar boundary layer based on the Falkner-Skan equation. The model is able to provide a friction estimate from the knowledge of the pressure at the wall vicinity. A validation with respect to wall-resolved solutions is then carried out by considering a flat plate and the Hiemenz flow. The robustness and accuracy of the LWM are demonstrated in both cases, except near the leading edge of the flat plate where the self-similarity assumption is not appropriate.

Then, a method for calculating distances on irregular triangular meshes is developed in order to apply the LWM to curved surfaces. The resulting algorithm provides the shortest distance over the surface with respect to an imposed set of stagnation points. A succession of convergence studies for different test cases demonstrates that the process leads to a distance field with a sufficiently good accuracy and smoothness for wall-modeling applications.

A hybrid wall model (HWM) is finally built by combining the LWM with a turbulent wall model based on the general wall function. In order to validate it, different flows over an extruded wing are considered: the NACA0012 with ($Re = 10.25 \cdot 10^6$; AoA $= 0°$) and the A-airfoil with ($Re = 3.1 \cdot 10^6$; AoA $= 3.4°$) and ($Re = 2.1 \cdot 10^6$; AoA $= 13.3°$). The HWM is first applied by hard-coding the transition between the two wall functions. The resulting wall-shear stress shows a good match with the empirical data for fully attached flows. Lastly, a sensor measuring the turbulent kinetic energy is used at each point of the surface to automatically determine the type of regime and impose the wall treatment accordingly. As long as the imposed sensor threshold is suitable and the mesh resolution sufficiently fine, the sensor is able to predict a transition corresponding relatively well with the experiment. However, the results show that these sensor parameters are case dependent.

Acknowledgments

First and foremost, I would like to thank Professor Stefan Hickel for welcoming me in his team. He gave me the opportunity to access the lab facilities and supervised my work. Without that, it would not have been possible to carry out such an interesting research project.

I would also like to thank Ata Baskaya for his spontaneous help and his continuous support, which was particularly useful throughout my internship.

I am grateful to my promoter in Uliège, Professor V.E. Terrapon, for giving me the opportunity to carry out my work at TU Delft. I would like to thank him for his availability and his advice all along this project.

Thanks should also go to my friends in Belgium and elsewhere for helping me to keep my motivation.

Finally, none of this would have been possible without the unconditional support of my family, who has always believed in me and done everything possible to help me with my projects. Many thanks to them.

Contents

List of Figures

List of Tables

Nomenclature

Acronyms

AGS	Average Gradient on Star
AMR	Adaptive Mesh Refinement
BVP	Boundary Value Problem
DNS	Direct Numerical Simulation
FS	Falkner-Skan
GWF	General Wall Function
HWM	Hybrid Wall Model
ILES	Implicit Large Eddy Simulation
IVP	Initial Value Problem
LES	Large Eddy Simulation
LLM	Logarithmic Law Mismatch
LR	Linear Regression
LSDD	Least Squares Fit of Directional Derivatives
LWM	Laminar Wall Model
ODE	Ordinary Differential Equation
RANS	Reynolds-Averaged Navier–Stokes
SFS	Sub-Filter Scales
SGS	Sub-Grid Scales
STL	Standard Triangle Language
TWM	Turbulent Wall Model
WMLES	Wall-Modeled Large Eddy Simulation
WM	Wall-Modeled
WR	Wall-Resolved

Roman symbols

$\mathbf{u}$	Velocity vector	$[\mathrm{m\ s^{-1}}]$

$\mathbf{x} \equiv (x, y, z)$	Three dimensional Cartesian coordinate system	[m]
AoA	Angle of attack	[°]
c	Chord length	[m]
E	Truncation error	
h_n	Step size	
h_w	Wall model height	[m]
$h_{w,p}$	Wall model height of extraction for the pressure	[m]
$h_{w,u}$	Wall model height of extraction for the wall-tangential velocity	[m]
k	Turbulent kinetic energy	[$\mathrm{m^2\ s^{-2}}$]
K	External flow velocity proportionality constant	[$\mathrm{s^{-1}}$]
N_{x_n}	Number of grid points in the wall-normal direction	[-]
N_{x_s}	Number of grid points in the wall-tangent direction	[-]
p	Static pressure	[$\mathrm{m^{-1}\ kg\ s^{-2}}$]
p_∞	Free-stream static pressure	[$\mathrm{m^{-1}\ kg\ s^{-2}}$]
$s_{\mathrm{w,thr}}$	Sensor threshold	[-]
s_w	Sensor value	[-]
T	Sensor averaging time	[s]
t	Time	[s]
u	Velocity in x-direction	[$\mathrm{m\ s^{-1}}$]
U_e	External flow velocity in the wall-tangent direction.	[$\mathrm{m\ s^{-1}}$]
U_∞	Free-stream velocity norm	[$\mathrm{m\ s^{-1}}$]
v	Velocity in y-direction	[$\mathrm{m\ s^{-1}}$]
$x_1 \equiv x_s$	Streamwise coordinate	[m]
$x_2 \equiv x_n$	Wall-normal coordinate	[m]
x_3	Spanwise coordinate	[m]
x_t	Laminar-turbulent transition x-coordinate	[m]
x_{st}	Stagnation point x-coordinate	[m]

Greek symbols

α	Shooting angle	[-]
$\bar{\varepsilon}_r$	Mean relative error	[-]
β, β_0	Falkner-Skan constants	[-]
Δt	Time step length	[s]
δ^*	Boundary layer displacement thickness	[m]
Δ_{min}	Minimum cell size	[m]

$\Delta_{x,y,z}$	Grid cell size	[m]
η	Similarity variable	[-]
η_∞	Truncated infinite similarity variable	[-]
μ	Dynamic viscosity	[m^{-1} kg s^{-1}]
ν	Kinematic viscosity	[m^2 s^{-1}]
ϕ	Signed-distance function w.r.t. an interface	[m]
Φ	Level-set function	[m]
ρ	Density	[m^{-3} kg]
τ	Sensor time factor	[-]
τ_w	Wall-shear stress	[m^{-1} kg s^{-2}]
θ	Boundary layer momentum thickness	[m]
ε	Small number	
ε_r	Relative error	[-]

Non-dimensional numbers

c_f	Skin friction coefficient averaged in time and in the spanwise direction
$c_{f,l}$	Local skin friction coefficient averaged in time and in the spanwise direction
c_p	Pressure coefficient averaged in time and in the spanwise direction
Re	Reynolds number

Subscripts

$\{.\}_0$	At the initial time
$\{.\}_{\max}$	Maximum value
$\{.\}_{\min}$	Minimum value
$\{.\}_{ref}$	Reference solution
$\{.\}_r$	Relative
$\{.\}_t$	Related to the triangle t
$\{.\}_v$	Related to the vertex v
$\{.\}_w$	At the wall

Superscripts

$\{.\}^+$	In viscous unit
$\{.\}'$	Fluctuating component
$\{.\}'$	Residual component

Other symbols

$\lvert\{.\}\rvert$	Absolute value
$\Delta_r\{.\}$	Relative change
$\lVert\{.\}\rVert_\infty$	Infinity norm
$L^2\{.\} \equiv \lVert\{.\}\rVert$	Euclidean norm
$\langle\{.\}\rangle$	Averaged over a characteristic time
$\overline{\{.\}}$	Volume average
$\widehat{\{.\}}$	Filtered in physical space

Chapter 1

Introduction

Large Eddy Simulation (LES) is nowadays increasingly used and becomes more affordable due to the rise of the computing performances. The method consists in resolving only the large scales while modeling the small ones. It therefore enables to obtain a better accuracy and a higher fidelity compared to the Reynolds-Averaged Navier-Stokes (RANS) approach. On the other side, it provides a more acceptable computational cost for complex applications contrary to Direct Numerical Simulation (DNS). Although being an interesting trade-off between RANS and DNS, the LES resolution required for wall-bounded flows remains, however, a significant barrier for most of the practical engineering settings. To quantify that, Chapman (1979) [1] estimated that the required number of grid points to resolve the outer layer has to be scaled as $(N_x N_y N_z)_{\text{ol}} \sim Re^{0.4}$, while the inner layer has to be scaled at least as $(N_x N_y N_z)_{\text{il}} \sim c_f Re^2 \sim Re^{1.8}$ with c_f the friction coefficient. This stronger constraint for the inner layer comes from the fact that the physical dimensions of the eddies diminish much faster than the boundary layer thickness as the Re increases. Finally, Piomelli [2] quantified the total cost by taking into account the integral time scales enabling to obtain converged statistics. Considering that the time step is imposed by the CFL condition, the total cost is scaled as $Re^{0.6}$ for the outer layer and as $Re^{2.4}$ for inner layer. Hence, it is obvious that the wall-bounded LES is only efficient at moderate Reynolds numbers due to the inner layer resolution.

In order to bypass this near-wall problem, many solutions have been proposed in the literature, all aiming to avoid the resolution of the inner layer. In this work, the focus is on the wall modeled LES (WMLES). This consists in modeling the effect of the inner layer, i.e. about 10-20% of the boundary layer thickness, while resolving the outer layer. According to Larsson et al. [3] and Hickel et al. [4], the WMLES can be split into two main categories: the hybrid LES/RANS and the wall-stress models.

In the first class, the inner layer is simply solved using a RANS solver up to an interface at a wall distance h_w, while the rest of the flow is solved by a LES solver, see Fig 1.1. The unsteady equations involving an eddy viscosity term are thus solved in the whole domain. The eddy viscosity is approximated by a RANS model in the inner layer and by a subgrid scale model in the rest of the domain. In practice, the interface between the two zones can be critical and lead to the logarithmic law mismatch (LLM), i.e. to a log layer displaced upwards. Relying on Baggett [5], such an error is due to the lack of resolved eddies in the interface region: the eddies immediately above the RANS zone maintain the RANS characteristic length scales and the smaller ones only appear very far away from the wall. Piomelli et al. [6] and Keating et al. [7] revealed that the introduction of stochastic forcing enables to accelerate the generation of resolved eddies and thus reduce the LLM. Eventually, Radhakrishnan et al. [8] brought out that the mean flow perturbations also enable to improve the accuracy of the hybrid method without adding any stochastic forcing but directly thanks to the resulting unstable flow conditions.

Regarding the wall-stress modeled LES, the filtered Navier–Stokes equations are solved in the entire domain. As shown in Fig 1.2, the difference with respect to traditional LES lies in the boundary conditions. Instead of imposing a no-slip condition at the wall, the impermeability condition is combined with a Neumann condition prescribing the wall-shear stress. To do so, a model is fed with instantaneous data in h_w from the LES solution and returns an estimate of the wall-shear stress. In the case where the energy equation is solved, there is an additional estimate of the heat flux from the knowledge of the temperature.

The difference between the wall-stress models and the hybrid LES/RANS lies mainly in the coupling with the LES region. Compared to the hybrid case, the exchange of information between a wall-stress model and the LES solution is relatively weak. In terms of performance, Piomelli [2] stated that none of these two methods is clearly superior to the other. In this work, only the wall-stress models are considered and the hybrid LES/RANS is out of the scope.

Relying on Chapman's estimations (1974) [1] mentioned above, the WMLES should have been commonly used by the 1990s for practical 3D applications. According to Slotnick et al. (2014) [9], such a prediction has not been achieved in practice and was too optimistic due to the underestimation of the computational work related to the LES. Choi and Moin [10] revisited Chapman's estimate and obtained a required resolution for WMLES in the turbulent region scaled asymptotically with the Reynolds number, i.e. $(N_x N_y N_z)_{\text{ol}} \sim Re$, while Chapman had obtained $(N_x N_y N_z)_{\text{ol}} \sim Re^{0.4}$. It is important to underline that neither of these two estimates takes into account the cost related to the laminar part. In practice, although this region represents a small part of the boundary layer, it is much thinner than the turbulent region and therefore implies a significant computational cost. As an order of magnitude, Slotnick et al. [9] concluded that the computational cost in the laminar region can be 10 to 100 times larger than the one required to solve the modeled turbulent boundary layer.

Such a problem is commonly encountered in the aerodynamic applications presenting a turbulent transition. The flow around a wing generally presents a very thin laminar region at the leading edge vicinity extending on a few percent of the chord length. Gonzalez et al. [11] demonstrated the importance of this latter by modeling the flow around a NACA0012 for different resolutions at the leading edge. The simulations revealed that the under-resolution of this region significantly impacts the entire flow due to the propagation of the error downstream. That typically leads to spurious flow separation and affects the estimation of the lift, drag and pressure distribution. Subsequently, Goc et al. [12] investigated WMLES for a realistic aircraft model in landing configuration. The study revealed that a targeted grid refinement focused on the thin leading edge boundary layers on the slat, on the main element and on the flap enables to recover some fundamental flow features observed with the empirical data. From these two examples, it is thus possible to conclude that, although representing a weak part of the entire flow, the laminar boundary layer at the leading edge vicinity has all its importance for the global accuracy of the solution.

In response to that, different works have been carried out in order to develop models treating laminar boundary layers. Dauricio et al. [13] and Gonzalez et al. [11] both established a laminar model based on a local self-similar solution of the boundary layer. To do so, the local wall-shear stress is deduced from the Falkner-Skan equation and imposed as a boundary condition. There are, however, only a few works in the literature dealing with the laminar boundary layer modeling.

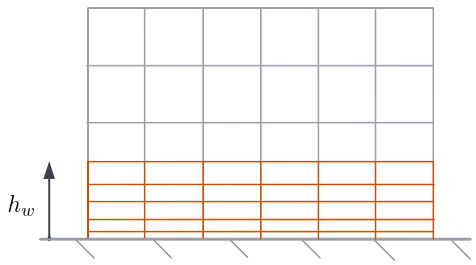

Figure 1.1: Schematic representation of the hybrid RANS/LES. The LES grid is represented in grey and the RANS one in orange.

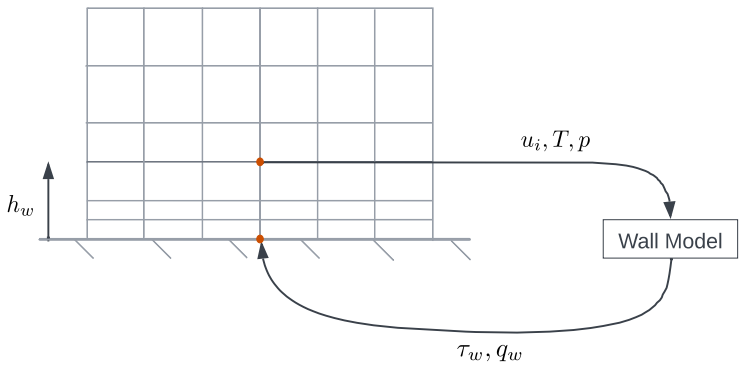

Figure 1.2: Schematic representation of the wall-stress modeling. Adapted from Larsson et al. [3].

1.1 LES and WMLES

The distribution of the turbulent kinetic energy among the eddies is described by the energy spectrum [14]. As shown in Fig 1.3, the spectrum represents the energy density $E_k(k)$ with respect to the wave number k. The wave number being inversely proportional to the size of the eddies, it brings out that the energy is mainly contained in the largest scales. Due to the instability of these turbulent structures, the latter successively break down into smaller scales through an energy cascade before being dissipated as heat on smaller scales. Relying on this spectral description, LES splits the flow into two parts by introducing a cut-off wavenumber $k_c = \pi/\Delta_c$ through a low-pass filtering operation with Δ_c being the filter width. The large scales such that $|k| < k_c$ are resolved during the simulation and the mesh resolution is sufficiently fine to represent their spatial and temporal evolution. The rest of the spectrum, composed of the sub-grid scales (SGS) and sub-filter scales (SFS), remains unresolved and must therefore be modeled. Indeed, on the one hand, the mesh can only represent the eddies of size comparable to the cell size, thus neglecting the SGS. On the other hand, the SFS are partially or completely removed by the filtering process. Note that there is a range of unresolved scales represented by the grid only if the mesh size Δ is finer than the filter width Δ_c.

As an order of magnitude, the filter and the grid have to be sufficiently fine to resolve at least 80% of the energy spectrum everywhere in the domain [15] in such a way that the cut wavenumber is located within the inertial range. If this condition is not verified, a significant part of the energy resides in the unresolved range. In the literature, a clear distinction is made for this latter case by introducing the name very-large-eddy simulation (VLES) [15, 16].

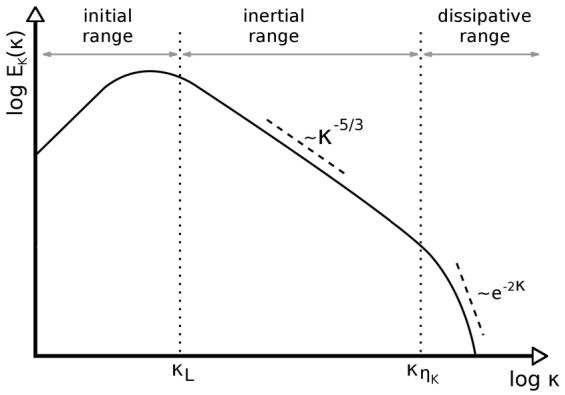

Figure 1.3: Energy spectrum of turbulence. From Ries [17].

According to Pope [15], the LES can be summarized in four conceptual steps:

1. A filtering operation in physical space to decompose the velocity $\mathbf{u}(\mathbf{x},t)$ into a filtered (or resolved) part $\hat{\mathbf{u}}(\mathbf{x},t)$ and a residual component $\mathbf{u}'(\mathbf{x},t)$ such that

$$\mathbf{u}(\mathbf{x},t) = \hat{\mathbf{u}}(\mathbf{x},t) + \mathbf{u}'(\mathbf{x},t). \tag{1.1.1}$$

2. The filtered Navier-Stokes equations are then derived to express the evolution of the filtered velocity field. In the case of an incompressible flow and considering a homogeneous filter, the system of equations is written as

$$\begin{aligned} &\partial_j \hat{u}_j = 0, \\ &\partial_t \hat{u}_i + \partial_j \hat{u}_j \hat{u}_i = -\frac{1}{\rho}\partial_i \hat{p} + \nu \nabla^2 \hat{u}_i - \partial_j \tau_{ij}^{\mathrm{SGS}}, \end{aligned} \tag{1.1.2}$$

   with $\hat{p}$ being the filtered static pressure and ν the molecular kinematic viscosity. The effect of the residual motion, i.e. the motion of the unresolved scales, is represented by the residual-stress tensor noted τ_{ij}^{SGS}.

3. Afterwards, the system of equations is closed using a SGS model to compute τ_{ij}^{SGS}.

4. Finally, the resulting modeled filtered equations are solved numerically to obtain the filtered solution $\hat{\mathbf{u}}$ approximating the large-scale motion.

The unresolved range is mainly involved in the molecular diffusion and in the dissipation of the energy coming from the larger scales. The fundamental role of the subgrid-scale modeling is thus to substitute that. To that end, several models are available in the literature like the Smagorinsky model [18] and the wall-adapting local eddy viscosity (WALE) model [19]. They generally present a more universal character, which is in line with the universality of the small turbulent scales. Alternately, the implicit LES (ILES) models the unresolved physics solely through the truncation error. There is thus no need to introduce an explicit model since the unresolved physics is approximated within the discretization scheme. Due to the absence of physical motivations, the implicit SGS models have been considered as inferior to the explicit models [20]. Despite that, ILES has proven itself in terms of computational efficiency and generality in many areas [21, 22]. In this context, a systematic approach for a general nonlinear discretization framework has been introduced by Hickel et al. [23]. The so-called adaptive local deconvolution method (ALDM) is based on the approximate deconvolution concept [24] and incorporates a physically consistent implicit SGS model by recovering the subgrid-scale energy transfer in agreement with theoretical predictions for isotropic turbulence. The validity of the method has been assessed and demonstrated for a wide range of complex flows [23, 25, 26].

Both for explicit and implicit LES, the so-called near-wall problem remains, i.e. the excessive computational cost due to the inner layer resolution. To overcome that, the WMLES is investigated in this work by focusing on the wall-stress models as introduced above and illustrated in Fig 1.2. Most of them assume a fully turbulent regime and are based on the principle of momentum conservation in a nearly parallel shear flow [2, 3, 27, 28]. In order to avoid the resolution of any turbulence in the inner layer, the momentum conservation equations are applied considering either a low-pass filter in the wall-parallel directions or ensemble-averaged. Considering an incompressible flow, the general form in the Cartesian coordinates of the filtered momentum conservation equations is expressed in the streamwise direction as [3]

$$\frac{\partial}{\partial x_2}\left[\left(\nu + \nu_{t,wm}\right)\frac{\partial u_1}{\partial x_2}\right] = \frac{1}{\rho}\frac{\partial p}{\partial x_1} + \frac{\partial u_1}{\partial t} + \frac{\partial}{\partial x_j}u_1 u_j, \tag{1.1.3}$$

with x_1, x_2 and x_3 being the streamwise, wall-normal and spanwise directions and u_1, u_2 and u_3 the related velocity components. Regarding the computation of the eddy viscosity $\nu_{t,wm}$, the wall-stress models generally use a zero-equation mixing-length model.

Solving these PDEs requires a separate near-wall grid with a full connectivity in all coordinate directions. In addition, it is necessary to ensure the quality of the grid in the wall-normal direction as is the case for a

RANS grid. These constraints imply a strong limitation for complex geometries and therefore restrict the applicability of a model using the PDEs as they are expressed in Eqn 1.1.3.

The most common models assume an equilibrium in such a way that the pressure term, the temporal term and the convective term are neglected, i.e. the right-hand side of Eqn 1.1.3 is set to zero. Such a simplification thereby leads to a linear tangential velocity profile in the viscous sublayer and to the log-law [29] in the overlap region as

$$u_1^+ \approx x_2^+ \quad \text{for } x_2^+ \lesssim 5 \qquad \text{and} \qquad u_1^+ \approx \ln\left(x_2^+\right)/\kappa + B \quad \text{for } x_2^+ \gtrsim 30, \tag{1.1.4}$$

with $\{.\}^+$ designating the wall units, $\kappa \simeq 0.41$ and $B \simeq 5.0$. Hence, with the extraction of the tangential speed from the LES solution in $x_2 = h_w$, it is possible to algebraically compute the wall-shear stress by solving the log-law with respect to the friction velocity. It is also possible to numerically solve the ODE

$$\left(\nu + \nu_{t,wm}\right) \frac{\partial u_1}{\partial x_2} = c^{st}. \tag{1.1.5}$$

In this case, the velocity profile is approximated through the entire inner layer and the wall-shear stress approximation remains correct if the grid approaches the traditional LES resolution with resolved viscous sublayer and buffer layer. Although less sensitive to the grid refinement below the log layer, this approach implies a significantly higher cost and the log-law algebraic approach is often preferred.

At first glance, one could think that the equilibrium assumption has to be avoided for any flow presenting non-equilibrium effects but it is less restrictive in practice. To justify that, Larsson [3] reminds that only the inner layer is modeled. There is thereby about 80% of the boundary layer which is fully resolved and which is able to capture the non-equilibrium effects. To complete this explanation, Larsson states that it is likely that the inner layer is close to equilibrium even in the case of a non-equilibrium flow. This can be justified by the fact that the turbulent time scale k/ε is approximately proportional to the wall distance x_2 in the inner layer and, consequently, most of the inner layer dynamics are much faster than all large-scale dynamics in the outer layer. Subsequently, Hickel et al. [4] studied two reference databases about an adverse pressure-gradient turbulent boundary layer and a shock/boundary layer interaction. In both cases, it revealed that the instantaneous convective terms were almost perfectly balanced by the instantaneous pressure gradient above the viscous layer. Based on these elements, it is therefore possible to conclude that the equilibrium assumption is relatively accurate even for non-equilibrium flows. Although the balance between the pressure and convective terms only holds above the viscous layer, the time scale of the viscous subpart pleads for a quasi-equilibrium state. The work about the confinement effects in shock wave/turbulent boundary layer interactions achieved by Bermejo-Moreno et al. [30] justifies *a posteriori* these words. Despite the use of an equilibrium wall-stress model and the presence of a significant pressure gradient, a good agreement with the experimentation was observed.

Although the equilibrium models are less restrictive than expected, different works have been carried out in order to include non-equilibrium terms in the purpose of obtaining a better accuracy for flows presenting separation, significant pressure gradient, etc. Balaras et al. [31] showed that retaining all the non-equilibrium terms enables to improve the agreement with the empirical data compared to the log-law for a rotating channel and for a flow in a square duct. Additionally, Catalano et al. [32] and Wang et al. [33] estimated the wall-shear stress components from the simplified version of Eqn 1.1.3 by dropping the last two terms of the right-hand side and retaining only the pressure gradient term. Considering a flow around a NACA4412 at high Reynolds number, Frère et al. [34] compared this last method with respect to an equilibrium approach. According to the authors, including only the pressure term deteriorates the performances and it is more interesting to use an equilibrium model. In this context, it seems relevant to remind the notion of consistency between the different non-equilibrium terms. To do so, the focus is on the region far from the wall where the flow verifies the Euler equation. After integration along a streamline, Bernoulli's equation enables to understand the link between the convective term and the pressure gradient term: a non-zero pressure gradient implies an acceleration/deceleration and therefore a change in the convective term. It is thus inconsistent to take into account the pressure gradient but not the convective term and conversely. Additionally, both temporal and convective terms describe the acceleration of a particle in its Lagrangian frame. Once again, for consistency considerations, both terms have to be either included or neglected conjointly. Consequently, if one of these three terms has to be retained, it is necessary to take all of them into account to ensure consistency.

For the sake of consistency, the non-equilibrium wall-stress models should therefore solve the PDEs as expressed in Eqn 1.1.3. As mentioned above, this implies a strong limitation for complex geometries due to the required grid connectivity in all directions. In order to get around that, Hickel et al. [4] proposed two convective parametrizations using the LES data to include the non-equilibrium effects in a consistent way while solving only the wall-normal ODEs. The first parametrization is based on the almost perfect balance between the pressure gradient term and the convective term out of the viscous sublayer, whereas the second one involves the velocity profile itself and the LES velocity gradient. Given that the pressure gradient is constant through the wall modeled layer and is directly provided from the LES solution, this term does not require any parametrization. Hence, the required connectivity is just in the wall-normal and temporal directions, which is in practice easily implemented for irregular geometries.

This section thereby enables to understand the basis of the LES and the role of both explicit and implicit SGS modeling. The near-wall problem is then investigated through the turbulent wall-stress models by aiming to understand the different ways to proceed, the limitations and the possible alternatives. On the one hand, it is first possible to assume an equilibrium in the inner layer, which can potentially lead to accurate results even for non-equilibrium flows. On the other hand, certain models take into account some or all of the three non-equilibrium terms in the right-hand side of Eqn 1.1.3. In this case, the consistency is ensured only if all of the three terms are neglected or considered conjointly. The integration of the convective term is particularly problematic in the case of complex geometries due to the introduction of wall-parallel derivatives. To overcome that, it is for example possible to use a convective parametrization and thus getting rid of the wall-parallel derivatives. It is good to keep in mind that this review is not exhaustive and acts only as an introduction to WMLES. The existing works about the turbulent wall models are numerous in the literature.

1.2 Immersed Boundary Method

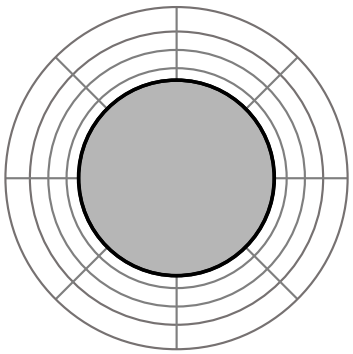

Figure 1.4: Body-fitted mesh.

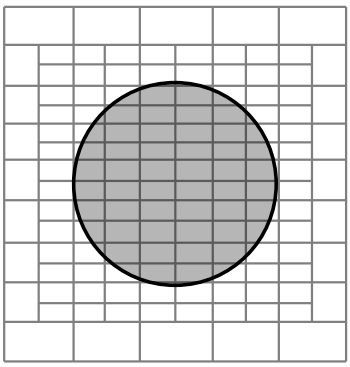

Figure 1.5: Immersed boundary method.

In real applications, simulating the flow around a body can be particularly challenging due to the complexity of the geometry. A conventional approach is the use of a body conforming grid, which enables to impose the boundary conditions at the body interface in a direct way, see Fig 1.4. In return, for an unstructured grid, it may imply a higher number of cells, a lower computational efficiency and a larger numerical truncation error [35]. Subsequently, such a method is extremely time-consuming and can lead to a severe degradation of the results quality for a moving interface. In order to overcome these limitations, Peskin [36] introduced the immersed boundary method to deal with complex geometries and moving interfaces. As shown in Fig 1.5, it consists in solving the flow field in a Cartesian mesh generated independently of the body surface. This greatly facilitates the grid generation and enables to obtain a mesh quality which does not depend on the geometry complexity. In practice, it enables to significantly reduce the user effort related to the grid generation compared to the body conforming method. However, it is now no longer possible to impose the boundary conditions in a straightforward way. The body surface does not match with the grid, which leads to cells composed of a solid and a fluid part. There are different procedures in the literature to treat such cells. According to Mittal et al. [37], the different methods can be grouped into two main categories: continuous

and discrete forcing approaches.

Both forcing techniques introduce a forcing function in the governing equations to reproduce the effect of the interface. In the continuous case, a source term is imposed directly in the momentum equations and the resulting system is then discretized on a Cartesian grid [38, 39, 40, 41]. The forcing term is thus independent of the spatial discretization process, which makes the implementation relatively simple. Nonetheless, this approach generally presents spurious loss or production of mass, momentum and energy at the interface [42, 43]. This drawback is particularly problematic for typical LES grid resolution [35]. In the discrete case, the equations are first discretized neglecting the immersed boundary effect. Only then is an adjustment achieved by a discrete forcing function. Considering such a methodology, Mohd-Yusof [44] and Verzicco et al. [45] proposed a predictor-corrector formulation to impose a wall boundary condition with a discrete forcing function injected in the momentum equations. Although the method is able to provide an accurate representation of the boundary, a lack of conservativity is also observed.

The conservativity problem can be avoided by using another discrete forcing approach, the so-called cut cell method, initially introduced by Clarke et al. [46] and Gaffney et al. [47] for an inviscid flow. The technique represents a consistent extension of the finite volume method, verifying thereby the conservation laws locally and globally. As a general process, the control volumes at the interface are reshaped locally to fit with the boundary surface. However, in practice, that can lead to instabilities in the case of explicit time integration, as well as to poor convergence for implicit schemes due to the risk of a very small fluid fraction in certain cut cells. To overcome that, stabilization processes are used to ensure a stable time integration. Ye et al. [48] and Bayyuk et al. [49] proposed a cell-merging technique by combining the fluid part of the cut cells whose center is located within the solid part with adjacent fluid cells. The main drawback of such a process is the additional complexity introduced by the merging since the computational stencil of the merged cells and their adjacent cells differs from the ones of regular internal cells. To avoid that, alternatives have been developed, such as the cell linking method [50] and the flux redistribution [51, 52]. Combining both methods, Hu et al. [53] introduced the mixing length procedure for two dimensions and a compressible flow in which a cut cell is mixed with one or several neighboring cells in a conservative way. A revision and an extension to multidimensional problems were then proposed by Lauer et al. [54]. Still using a mixing procedure, Meyer et al. [55, 56] have built a second-order accurate conservative immersed interface method based on a cut cell method for incompressible flow. It has been demonstrated that the process offers good performance and accuracy for both laminar and turbulent flows.

1.3 Objectives and Motivations

Most of the industrial and aerodynamic applications at high Reynolds numbers present a wall-bounded flow. In practice, a RANS approach is generally used in order to obtain a relatively interesting computational cost. In return, the flow is only resolved in the averaged sense and the fluctuations are modeled. The fundamental limitations in this approach have been highlighted during the Turbulence Modeling Workshop in Michigan [57] by introducing the notion of "ultimate barrier" with respect to RANS turbulence modeling. This means that the RANS modeling accuracy is limited by an upper-bound due to the RANS approach itself and that many current applications may be close to this limit. However, according to Bush et al. [58], this concept is not universally accepted. In the literature, some state that if the limit exists, this latter is problem-dependent and others claim that current RANS models can be significantly improved to extend the accuracy and affordability of the RANS approach.

The RANS limitations have sparked a deeper interest in LES and DNS fields. Both of them remain, however, generally too expensive for complex applications. In response to that, a major effort has been made on the WMLES field in order to obtain a better accuracy while avoiding the excessive computational cost related to the inner layer resolution. Nevertheless, most of the existing wall models assume a fully turbulent flow and only few works in the literature have aimed to develop laminar modeling. Considering a flow over a wing, this simplification introduces a significant error at the leading edge vicinity, which can strongly impact the accuracy of the whole solution as concluded above. The first objective of this work is thus to develop a laminar wall model (LWM) based on the Falkner-Skan equation as carried out by Dauricio et al. [13] and Gonzalez et al. [11].

For the sake of generality and efficiency, the LWM will be developed to be applied to immersed boundaries. More specifically, the cut cell method with the mixing procedure proposed by Meyer et al. [55, 56] will be used in order to avoid the conservativity problem encountered with the other approaches. Thereby, it will be possible to efficiently handle complex geometries and moving interfaces. In practice, this means that it is necessary to be able to calculate distances with respect to stagnation points on irregular triangular meshes. To that end, the reinitialization process used by Lauer [59] for the signed-distance function in a Cartesian mesh will be adapted.

The next step is to carry out a hybrid model by combining the established LWM with an existing turbulent wall model to approximate flows with laminar-turbulent transition. The transition location will first be taken from the literature and imposed to switch between the two models. Finally, a sensor measuring the turbulent kinetic energy [3] will be implemented to automatically detect the type of regime and choose one of the two models accordingly.

Once the hybrid model established, different test cases considering an extruded wing will be investigated in order to answer the following questions:

> *How accurate is the wall-shear stress predicted by the hybrid wall model compared to experimental data, and what are the main physical limitations of the model?*
>
> *Is the sensor able to reliably predict a laminar-turbulent transition for typical wall-modeled LES resolution and how robust is it?*

Chapter 2

Incompressible Navier-Stokes Solver

The development environment is INCA [35, 60, 61], a general-purpose multi-physics Computational Fluid Dynamics (CFD) solver mainly applied in the fields of turbulence research and aerospace engineering. This one can be used either as a solver for Direct Numerical Simulation (DNS) or for Large Eddy Simulation (LES). The implementation is written in the programming language Fortran. Additionally, the solver performance can be easily improved using a MPI and OpenMP parallelization. To do so, it is enough to carry out a pre-processing aiming to split the domain into several sub-blocks. Finally, the simulations are performed on the supercomputer DelftBlue [62] created and developed at Technische Universiteit Delft.

In this work, the INCA's conservative, second-order accurate immersed interface method for LES of incompressible flows [55] is used with staggered Cartesian grids. Such a method is based on a finite-volume discretization of the incompressible Navier–Stokes equations with a local modification in cells that are cut by the interface. The convective terms are discretized by the Adaptive Local Deconvolution Method (ALDM) [23] and a second-order accurate central difference scheme is employed to discretize the pressure gradient and the viscous terms. In case of non-turbulent flows, the ALDM simply corresponds to a standard central second-order finite-volume scheme, whereas in case of turbulent flows, it models the subgrid scales implicitly through the truncation error. In addition, the time progression is carried out using a third-order explicit three step Runge–Kutta scheme [63] and the time step is dynamically adapted to satisfy the Courant-Friedrichs-Lewy (CFL) condition as CFL = 1.0. Regarding the frequency spectrum, no explicit LES filtering operation is applied, the cut-off frequency is only imposed by the grid resolution.

Finally, for the sake of efficiency, the mesh generation is achieved using the adaptive mesh refinement (AMR) method. To that end, a uniform Cartesian mesh of resolution $N_x \cdot N_y \cdot N_z$ is first provided to the module. Then, a succession of refinement steps are applied to obtain a finer mesh at the immersed boundary vicinity while keeping a smooth cell size variation.

2.1 Governing Equations

The motion of the fluid is described by the Navier-Stokes equations on a domain denoted Ω. The latter can be expressed using a generic conservation equation as

$$\frac{\partial \mathbf{U}}{\partial t} + \nabla \cdot \mathbf{F}(\mathbf{U}) = 0, \tag{2.1.1}$$

with $\mathbf{U}$ corresponding to the conserved quantity and $\mathbf{F}(\mathbf{U})$ to a flux function. Considering an incompressible flow, the conserved quantity vector $\mathbf{U}$ equals the velocity vector $\mathbf{u} = [u_1, u_2, u_3]^T$ and the flux is expressed as

$$\mathbf{F} = \mathbf{uu} + \mathbf{I}p - \nu \nabla \mathbf{u}, \tag{2.1.2}$$

where ν being the kinematic viscosity, p the static pressure and $\mathbf{I}$ the unity tensor. Subsequently, mass conservation on Ω is ensured by

$$\nabla \cdot \mathbf{u} = 0. \tag{2.1.3}$$

Applying a finite volume discretization of Eqn 2.1.1 and a time integration from step t_n to t_{n+1} with a time step $\Delta t = t_{n+1} - t_n$, it comes to

$$\frac{1}{V_{i,j,k}\Delta t}\int_{t_n}^{t_{n+1}} dt \int_{V_{i,j,k}\cap\Omega} dxdydz \left(\frac{\partial \mathbf{u}}{\partial t} + \nabla\cdot\mathbf{F}\right) = 0, \tag{2.1.4}$$

where $V_{i,j,k}\cap\Omega$ being a computational cell (i,j,k) of the Cartesian grid. Afterwards, using an Euler forward scheme, which is a substep of the third order Runge-Kutta scheme used in this work, the discretized formulation of Eqn 2.1.4 is

$$\frac{\overline{\mathbf{u}}^{n+1}_{i,j,k} - \overline{\mathbf{u}}^{n}_{i,j,k}}{\Delta t} = \frac{1}{V_{i,j,k}}\int_{V_{i,j,k}\cap\Omega} \nabla\cdot\mathbf{F}\left(\overline{\mathbf{u}}^n, \overline{p}^n\right)_{i,j,k} dxdydz, \tag{2.1.5}$$

with the volume-averaged quantity $\overline{\mathbf{u}}_{i,j,k}$ expressed as

$$\overline{\mathbf{u}}_{i,j,k} = \frac{1}{V_{i,j,k}}\int_{V_{i,j,k}\cap\Omega} \mathbf{u}_{i,j,k} dxdydz. \tag{2.1.6}$$

The divergence-free condition 2.1.3 is then enforced using a fractional-step method involving the intermediate velocity

$$\overline{\mathbf{u}}^{\star}_{i,j,k} = \overline{\mathbf{u}}^{n}_{i,j,k} + \frac{\Delta t}{V_{i,j,k}}\int_{V_{i,j,k}\cap\Omega} \nabla\cdot\mathbf{F}\left(\overline{\mathbf{u}}^n, \overline{p}^n\right)_{i,j,k} dxdydz, \tag{2.1.7}$$

with $\mathbf{F}\left(\overline{\mathbf{u}}^n_{i,j,k}, \overline{p}^n\right)$ including a predictor for the pressure gradient from the pressure at time step n. The divergence-free velocity field $\overline{\mathbf{u}}^{n+1}_{i,j,k}$ is obtained by solving a Poisson equation

$$\nabla^2\overline{\phi}_{i,j,k} = -\nabla\cdot\overline{\mathbf{u}}^{\star}_{i,j,k} \tag{2.1.8}$$

leading to

$$\overline{\mathbf{u}}^{n+1}_{i,j,k} = \overline{\mathbf{u}}^{n}_{i,j,k} - \nabla\overline{\phi}_{i,j,k}. \tag{2.1.9}$$

Eventually, an update of the pressure is achieved as

$$\overline{p}^{n+1}_{i,j,k} = \overline{p}^{n}_{i,j,k} + \frac{\overline{\phi}_{i,j,k}}{\Delta t}. \tag{2.1.10}$$

Using the Gauss theorem, the right-hand side of Eq 2.1.7 can be expressed as

$$\begin{aligned}\overline{\mathbf{u}}^{\star}_{i,j,k} =& \overline{\mathbf{u}}^{n}_{i,j,k} \\ &+ \frac{\Delta t}{\Delta x}\left[\overline{\mathbf{F}}_{i+1/2,j,k} - \overline{\mathbf{F}}_{i-1/2,j,k}\right] \\ &+ \frac{\Delta t}{\Delta y}\left[\overline{\mathbf{F}}_{i,j+1/2,k} - \overline{\mathbf{F}}_{i,j-1/2,k}\right] \\ &+ \frac{\Delta t}{\Delta z}\left[\overline{\mathbf{F}}_{i,j,k+1/2} - \overline{\mathbf{F}}_{i,j,k-1/2}\right],\end{aligned} \tag{2.1.11}$$

where $\overline{\mathbf{F}}_{i\pm1/2,j,k}, \overline{\mathbf{F}}_{i,j\pm1/2,k}, \overline{\mathbf{F}}_{i,j,k\pm1/2}$ are the face-averaged fluxes at the cell faces. These latter are computed by applying the ALDM [23].

2.2 Staggered Mesh

The governing equations are discretized on a Cartesian staggered grid. Harlow and Welsh [64] introduced this arrangement to take advantage of the fact that there is no need to use a single grid for all variables as shown in Fig 2.1. Contrary to a collocated mesh, it enables to calculate several terms without any interpolation. Considering the momentum equations, both pressure and diffusive terms can thus be directly obtained from the values at their respective nodes. Subsequently, relying on Ferziger et al. [64], this type of grid offers a

strong coupling between the velocities and the pressure. In practice, this enables to avoid some types of convergence issues and oscillations in pressure and velocity fields.

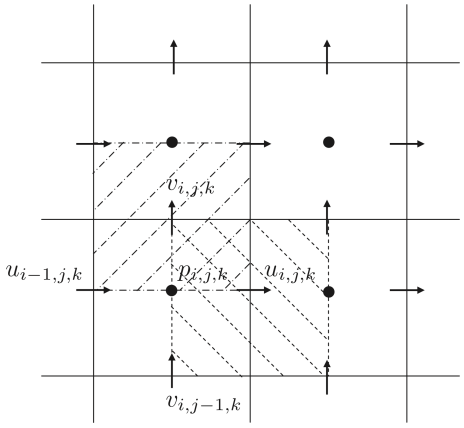

Figure 2.1: Staggered grid in 2D with u control volume (dashed line), v control volume (dash-dotted line) and p control volume of a cell; arrows indicate locations of velocity components, circles locations of pressure. From Meyer et al. [55].

2.3 Conservative Immersed Interface Method (CIIM)

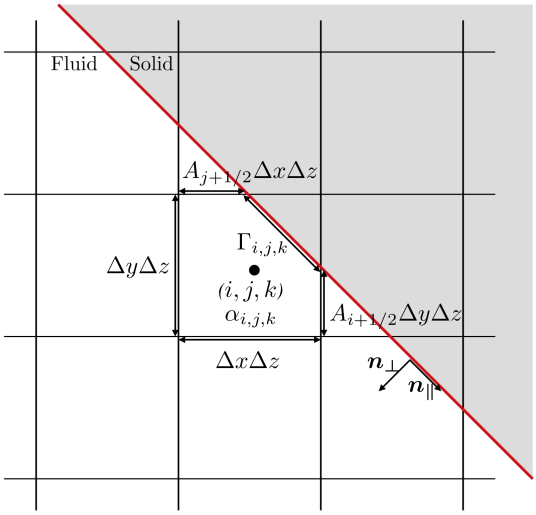

Figure 2.2: Two-dimensional sketch of a cut cell $(i,\ j,\ k)$. From Meyer et al. [55].

Now that the standard finite-volume discretization has been expressed in Eqn 2.1.11, it is necessary to adapt it for a cut cell $(i,\ j,\ k)$, as illustrated in Fig 2.2. For such a cell, the solid and fluid parts are separated by an interface $\Gamma_{i,j,k}$. The fluid volume fraction is denoted as $\alpha_{i,j,k}$ with $0 \leqslant \alpha_{i,j,k} \leqslant 1$ and the wetted segment of the cell faces is expressed as $A_{i\pm1/2j,k}\Delta y\Delta z$, $A_{i,j\pm1/2,k}\Delta x\Delta z$, and $A_{ij,k\pm1/2}\Delta x\Delta y$, where $0 \leqslant A_{l,m,n} \leqslant 1$ being the face aperture. Using this notation, the fluid volume is expressed as $V_{i,j,k} = \alpha_{i,j,k}\Delta x\Delta y\Delta z$ and the intermediate velocity as

$$
\begin{aligned}
\overline{\mathbf{u}}^{\star}_{i,j,k} = \overline{\mathbf{u}}^{n}_{i,j,k} & \\
&+ \frac{\Delta t}{\alpha_{i,j,k}\Delta x}\left[A_{i+1/2,j,k}\overline{\mathbf{F}}_{i+1/2,j,k} - A_{i-1/2,j,k}\overline{\mathbf{F}}_{i-1/2,j,k}\right] \\
&+ \frac{\Delta t}{\alpha_{i,j,k}\Delta y}\left[A_{i,j+1/2,k}\overline{\mathbf{F}}_{i,j+1/2,k} - A_{i,j-1/2,k}\overline{\mathbf{F}}_{i,j-1/2,k}\right] \\
&+ \frac{\Delta t}{\alpha_{i,j,k}\Delta z}\left[A_{i,j,k+1/2}\overline{\mathbf{F}}_{i,j,k+1/2} - A_{i,j,k-1/2}\overline{\mathbf{F}}_{i,j,k-1/2}\right] \\
&+ \frac{\Delta t}{\alpha_{i,j,k}\Delta x\Delta y\Delta z}[\mathbf{C}+\mathbf{D}],
\end{aligned}
\tag{2.3.1}
$$

where $\mathbf{C}$ denotes the momentum-exchange term enabling to enforce the impermeability condition with respect to the normal velocity components at the interface. Note that this term is non-zero only in the case of a moving interface. On the other side, $\mathbf{D}$ represents to the friction force at the interface $\Gamma_{i,j,k}$ and is written as

$$
\mathbf{D} = -\int_{\Gamma_{i,j,k}} \boldsymbol{\tau}_w dS, \tag{2.3.2}
$$

with the wall-shear stress $\boldsymbol{\tau}_w$ expressed as

$$
\boldsymbol{\tau}_w = \nu(\nabla\overline{\mathbf{u}})\cdot\mathbf{n}_{\perp}, \tag{2.3.3}
$$

where $\mathbf{n}_{\perp}$ denotes the interface normal. This term enables to enforce the no-slip condition with respect to the tangential velocity components at $\Gamma_{i,j,k}$.

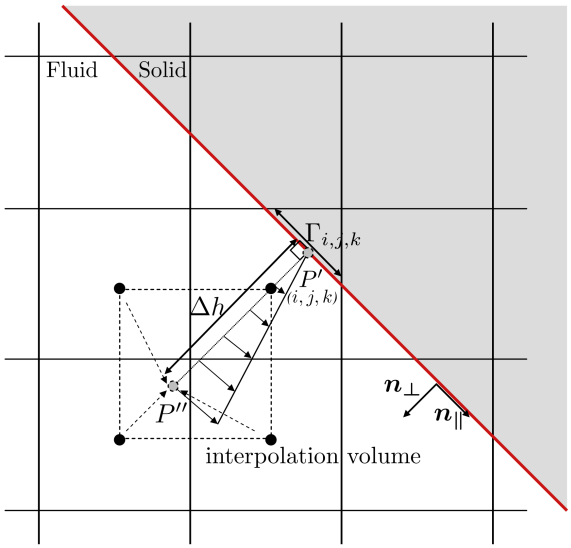

Figure 2.3: Linear approximation of the velocity gradient of a velocity cell. From Meyer et al. [55].

Considering the wall-resolved case, the wall-normal gradient is obtained by applying a linear approximation [55] from the difference of the interface velocity $\overline{\mathbf{u}}_{\Gamma}(P')$ and the tangential velocity $\overline{\mathbf{u}}_{\parallel}(P'')$ in point P'', as shown in Fig 2.3. P' stands for the normal projection of the cell center of cell (i,j,k) on $\Gamma_{i,j,k}$ and P'' results from a translation along the interface normal over a distance Δh. The velocity in P'' is obtained by trilinear Lagrangian interpolation from the velocities at the eight neighboring velocity-cell centers. Hence, this approach enables to express $\mathbf{D}$ as

$$
\mathbf{D} = -\frac{\nu\Gamma_{i,j,k}}{\Delta h}\left(\overline{\mathbf{u}}_{\parallel} - \overline{\mathbf{u}}_{\Gamma}\right). \tag{2.3.4}
$$

It is obvious that such a method requires a sufficiently fine mesh resolution to obtain a reliable gradient estimate and does not seem suitable for coarse grids. This is where the wall model comes in, by providing an

expectedly more accurate estimate of the wall-shear stress than the linear approximation. INCA proposes different turbulent wall models either assuming an equilibrium or not through the boundary layer. In order to go further, this current work aspires to provide a model being able to approximate a flow with a laminar-turbulent transition.

Chapter 3

Laminar Wall Model (LWM)

As a fundamental base, the laminar wall model presumes that the dynamics of the near-wall region can be described at each location as a self-similar solution. Specifically, it is assumed that the laminar boundary layer locally verifies the Falkner-Skan (FS) equation. The physics in the inner region is therefore restricted to an incompressible, steady and two-dimensional flow. Based on these simplifications, the wall-shear stress can thereby be deduced by solving the FS third-order ordinary differential equation (ODE) over a semi-infinite interval with the suitable local FS constants. To that end, the shooting process presented by Asaithambi [65] is implemented to turn the boundary value problem (BVP) of the Falkner-Skan equation into an initial value problem (IVP) made of a system of first order ODEs and to solve this latter. To make this process operational, a first order ODEs solver is carried out relying on the Dormand-Prince algorithm. As schematized in Fig 3.1, the shooting method enables to obtain the so-called shooting angle α involved in the wall-shear stress computation. Then, after providing the streamwise coordinate and estimating the outer flow velocity from the pressure field at the wall vicinity, the wall-shear stress can be directly computed and provided as a boundary condition.

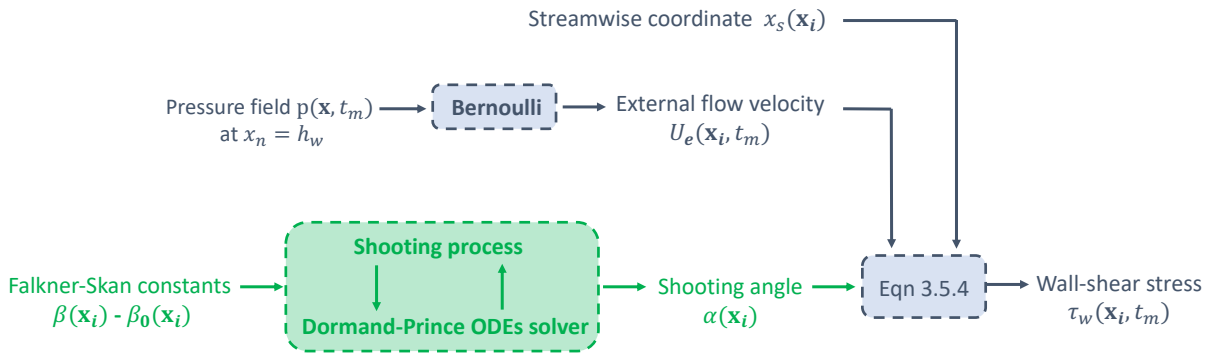

Figure 3.1: Schematic representation of the laminar wall model (LWM) considering the wall point $\mathbf{x}_i$ at the m^{th} time step (blue part) and the related pre-processing (green part).

3.1 Initial Value Problem

The Falkner-Skan (FS) equation is given by

$$\frac{d^3 f}{d\eta^3} + \beta_0 f \frac{d^2 f}{d\eta^2} + \beta \left[1 - \left(\frac{df}{d\eta} \right)^2 \right] = 0, \quad 0 < \eta < \infty, \tag{3.1.1}$$

with β and β_0 being the two FS constants depending on the geometry. The variable η denotes the similarity variable expressed as

$$\eta = \frac{x_n}{\lambda\,(x_s)},$$

where $\lambda(x_s)$ is the constant of proportionality of the boundary layer thickness scaling factor, x_s the streamwise coordinate and x_n the wall-normal coordinate. Subsequently, the boundary conditions are

$$f = 0 \quad \text{in } \eta = 0, \tag{3.1.2}$$

$$\frac{df}{d\eta} = 0 \quad \text{in } \eta = 0, \tag{3.1.3}$$

$$\frac{df}{d\eta} = 1 \quad \text{in } \eta \to \infty. \tag{3.1.4}$$

In order to solve the BVP of the FS Eqn 3.1.1, the computational method proposed by Asaithambi [65] is applied in the following of this section. The first step consists in introducing an additional boundary condition in $\eta = 0$ such that

$$\frac{d^2 f}{d\eta^2} = \alpha \quad \text{in } \eta = 0, \tag{3.1.5}$$

with α being designated as the shooting angle. As mentioned previously, this parameter will be used in the following to compute the wall-shear stress and stands for the main output of the FS equation resolution process. Thanks to this latter, it is now possible to solve the FS equation through a shooting method by iteratively solving the obtained IVP. Given that α directly influences the value of $df/d\eta$ at $\eta \to \infty$, the shooting angle has to be such that the condition 3.1.4 is verified. Then, for numerical considerations, it is necessary to truncate the semi-infinite interval into a finite one. To do so, the boundary condition 3.1.4 in $\eta \to \infty$ is replaced by the following one

$$\frac{df}{d\eta} = 1 \quad \text{in } \eta = \eta_\infty, \tag{3.1.6}$$

with η_∞ the truncated infinite similarity variable which has to be sufficiently large. Due to the introduction of the new unknown η_∞, it is required to impose an additional boundary condition as

$$\frac{d^2 f}{d\eta^2} = 0, \quad \text{in } \eta = \eta_\infty. \tag{3.1.7}$$

The shooting process thereby consists in iterating on both η_∞ and α while solving the IVP made of Eqn 3.1.1 - 3.1.3 and 3.1.5 up to verifying the truncated boundary conditions 3.1.6 and 3.1.7. Since both these asymptotic boundary conditions are evaluated at η_∞, which varies through the iterations, the coordinate transformation

$$\xi = \frac{\eta}{\eta_\infty} \tag{3.1.8}$$

is introduced in order to simplify the resolution. Subsequently, the original three-order Eqn 3.1.1 is turned into a system of three first-order equations expressed as

$$\begin{cases} \dfrac{df}{d\xi} = \eta_\infty u, \\ \dfrac{du}{d\xi} = \eta_\infty v, \\ \dfrac{dv}{d\xi} = -\eta_\infty \left[\beta_0 f v + \beta\left(1 - u^2\right)\right], \end{cases} \qquad 0 < \xi < 1 \tag{3.1.9}$$

by introducing the following change of variables

$$u = \frac{1}{\eta_\infty}\frac{df}{d\xi} \qquad \text{and} \qquad v = \frac{1}{\eta_\infty^2}\frac{d^2 f}{d\xi^2}. \tag{3.1.10}$$

Accordingly, the boundary conditions are written as

$$f(0) = 0, \quad u(0) = 0, \quad v(0) = \alpha, \tag{3.1.11}$$

$$u(1) = 1, \quad v(1) = 0. \tag{3.1.12}$$

3.2 Shooting Process

The system of equations and the boundary conditions being established, it is now relevant to focus on the shooting method itself. For the sake of convenience, the two following variables are introduced

$$\begin{aligned} p\left(\alpha,\eta_\infty\right) &= u\left(1;\alpha,\eta_\infty\right)-1,\\ q\left(\alpha,\eta_\infty\right) &= v\left(1;\alpha,\eta_\infty\right). \end{aligned} \tag{3.2.1}$$

Hence, the resolution process now consists in determining α and η_∞ verifying

$$\mathbf{F}\left(\alpha,\eta_\infty\right) = \begin{pmatrix} p\left(\alpha,\eta_\infty\right)\\ q\left(\alpha,\eta_\infty\right)\end{pmatrix} = \mathbf{0}. \tag{3.2.2}$$

These two variables are updated at the i^{th} step using Newton's 2D method such as

$$\begin{cases} \mathbf{F}'\left(\alpha^i,\eta_\infty^i\right)\begin{pmatrix}\Delta\alpha^i\\ \Delta\eta_\infty^i\end{pmatrix} = -\mathbf{F}\left(\alpha^i,\eta_\infty^i\right),\\ \begin{pmatrix}\alpha^{i+1}\\ \eta_\infty^{i+1}\end{pmatrix} = \begin{pmatrix}\alpha^i\\ \eta_\infty^i\end{pmatrix} + \begin{pmatrix}\Delta\alpha^i\\ \Delta\eta_\infty^i\end{pmatrix}, \quad i=0,1,\dots\\ \alpha^0=\alpha_0, \quad \eta_\infty^0=\eta_{\infty,0}, \end{cases} \tag{3.2.3}$$

with $\mathbf{F}'$ the Jacobian matrix of $\mathbf{F}$ expressed as

$$\mathbf{F}'\left(\alpha,\eta_\infty\right) = \begin{pmatrix} \partial p\left(\alpha,\eta_\infty\right)/\partial\alpha & \partial p\left(\alpha,\eta_\infty\right)/\partial\eta_\infty\\ \partial q\left(\alpha,\eta_\infty\right)/\partial\alpha & \partial q\left(\alpha,\eta_\infty\right)/\partial\eta_\infty\end{pmatrix}. \tag{3.2.4}$$

In order to evaluate the Jacobian matrix, it is necessary to solve two additional IVPs since $p\left(\alpha,\eta_\infty\right)$ and $q\left(\alpha,\eta_\infty\right)$ cannot be explicitly represented to find their respective derivative with respect to α and η_∞. The IVPs in question are obtained by establishing the partial derivative of Eqn 3.1.9 and 3.1.11 with respect to α as

$$\begin{cases} \dfrac{d}{d\xi}\left(\dfrac{\partial f}{\partial\alpha}\right) = \eta_\infty\dfrac{\partial u}{\partial\alpha},\\ \dfrac{d}{d\xi}\left(\dfrac{\partial u}{\partial\alpha}\right) = \eta_\infty\dfrac{\partial v}{\partial\alpha},\\ \dfrac{d}{d\xi}\left(\dfrac{\partial v}{\partial\alpha}\right) = -\eta_\infty\left[\beta_0\left(\dfrac{\partial f}{\partial\alpha}v+f\dfrac{\partial v}{\partial\alpha}\right)-2\beta u\dfrac{\partial u}{\partial\alpha}\right], \end{cases} \tag{3.2.5}$$

$$\frac{\partial f}{\partial\alpha}(0)=0, \quad \frac{\partial u}{\partial\alpha}(0)=0, \quad \frac{\partial v}{\partial\alpha}(0)=1, \tag{3.2.6}$$

and with respect to η_∞ as

$$\begin{cases} \dfrac{d}{d\xi}\left(\dfrac{\partial f}{\partial\eta_\infty}\right) = u+\eta_\infty\dfrac{\partial u}{\partial\eta_\infty},\\ \dfrac{d}{d\xi}\left(\dfrac{\partial u}{\partial\eta_\infty}\right) = v+\eta_\infty\dfrac{\partial v}{\partial\eta_\infty},\\ \dfrac{d}{d\xi}\left(\dfrac{\partial v}{\partial\eta_\infty}\right) = -\left[\beta_0 fv+\beta\left(1-u^2\right)\right]-\eta_\infty\left[\beta_0\left(\dfrac{\partial f}{\partial\eta_\infty}v+f\dfrac{\partial v}{\partial\eta_\infty}\right)-2\beta u\dfrac{\partial u}{\partial\eta_\infty}\right], \end{cases} \tag{3.2.7}$$

$$\frac{\partial f}{\partial \eta_\infty}(0) = 0, \quad \frac{\partial u}{\partial \eta_\infty}(0) = 0, \quad \frac{\partial v}{\partial \eta_\infty}(0) = 0. \tag{3.2.8}$$

This enables to obtain the Jacobian matrix such that

$$\mathbf{F}'(\alpha, \eta_\infty) = \begin{pmatrix} \partial u(\alpha, \eta_\infty)/\partial \alpha & \partial u(\alpha, \eta_\infty)/\partial \eta_\infty \\ \partial v(\alpha, \eta_\infty)/\partial \alpha & \partial v(\alpha, \eta_\infty)/\partial \eta_\infty \end{pmatrix}. \tag{3.2.9}$$

Considering that Newton's 2D method is fully established, it is theoretically possible to apply the shooting algorithm. However, in practice, such a process presents convergence problems and that, even for simple configurations like a flat plate. To overcome that, Zhang et al. [66] propose to introduce an internal loop at each i^{th} iteration based on Newton's method, which in this case is only applied on the shooting angle α until reaching a certain accuracy. The update of this parameter is thus achieved as

$$\begin{cases} \dfrac{\partial p\left(\alpha^i_{(j)}, \eta^i_\infty\right)}{\partial \alpha} \Delta\alpha^i_{(j)} = -p\left(\alpha^i_{(j)}, \eta^i_\infty\right), \\ \alpha^i_{(j+1)} = \alpha^i_{(j)} + \Delta\alpha^i_{(j)}, \\ \alpha^i_{(0)} = \alpha^i, \end{cases} \qquad j = 0, 1, \ldots \tag{3.2.10}$$

The resulting process is described by Algorithm 1.

Algorithm 1 Shooting process.

Initialization: $\alpha^0 = \alpha_0$ and $\eta^0_\infty = \eta_{\infty,0}$;

$i \leftarrow 0$;

do

- $\alpha^i_{(0)} \leftarrow \alpha^i$;
- $j \leftarrow 0$;
- **do**
  - Solve the IVPs 3.1.9, 3.1.11, 3.2.5 and 3.2.6 with $\alpha^i_{(j)}$ and η^i_∞;
  - Compute $\Delta\alpha^i_{(j)}$ and $\alpha^i_{(j+1)}$ using the 1-D Newton's method 3.2.10;
  - $j \leftarrow j + 1$;
- **while** $\left|p\left(\alpha^i_{(j-1)}, \eta^i_\infty\right)\right| > \varepsilon_p$;
- $\alpha^i \leftarrow \alpha^i_{(j-1)}$;
- Solve the IVPs 3.1.9, 3.1.11, 3.2.7 and 3.2.8 with α^i and η^i_∞;
- Compute $\mathbf{F}\left(\alpha^i, \eta^i_\infty\right)$ and $\mathbf{F}'\left(\alpha^i, \eta^i_\infty\right)$ respectively from Eqn 3.2.2 and Eqn 3.2.9;
- Compute $\begin{pmatrix} \Delta\alpha^i \\ \Delta\eta^i_\infty \end{pmatrix}$ and $\begin{pmatrix} \alpha^{i+1} \\ \eta^{i+1}_\infty \end{pmatrix}$ using the 2-D Newton's method 3.2.3;
- $i \leftarrow i + 1$;

while $\left|p\left(\alpha^{i-1}, \eta^{i-1}_\infty\right)\right| > \varepsilon_p \quad \& \quad \left|q\left(\alpha^{i-1}, \eta^{i-1}_\infty\right)\right| > \varepsilon_q$;

3.3 ODEs Solver

In order to be able to resolve the two IVPs involved in algorithm 1, a solver is implemented relying on an embedded Runge-Kutta formula RK5(4) derived by Dormand and Prince [67]. Considering a general formulation, the IVPs can be expressed as

$$\mathbf{y}'(x) = \mathbf{f}[x, \mathbf{y}(x)], \tag{3.3.1}$$

with $\mathbf{y}(x_0)$ known. The Runge-Kutta embedding technique consists in obtaining two RK formulae respectively of order p and q ($q > p$), in this particular case $p = 4$ and $q = 5$, which both share the same function evaluations. The approximation of the exact solution $\mathbf{y}(x_n)$ at x_n is noted $\mathbf{y}_n$ with $x_{n+1} = x_n + h_n$. Following this notation, the embedded algorithm can be formulated as

$$\begin{aligned} \hat{\mathbf{y}}_{n+1} &= \hat{\mathbf{y}}_n + \sum_{i=1}^{s} \hat{b}_i \mathbf{k}_i, \\ \mathbf{y}_{n+1} &= \hat{\mathbf{y}}_n + \sum_{i=1}^{s} b_i \mathbf{k}_i, \end{aligned} \tag{3.3.2}$$

where

$$\begin{aligned} \mathbf{k}_1 &= h_n \ \mathbf{f}\left(x_n, \hat{\mathbf{y}}_n\right), \\ \mathbf{k}_i &= h_n \ \mathbf{f}\left(x_n, \hat{\mathbf{y}}_n + \sum_{j=1}^{i-1} a_{ij} \mathbf{k}_j\right), \end{aligned} \tag{3.3.3}$$

for $i = 2, 3, \ldots, s$ with s the number of stages. The caps make reference to the order $q = 5$ such that $\hat{\mathbf{y}}_{n+1}$ is the 5^{th} order approximation and $\mathbf{y}_{n+1}$ the 4^{th} order one. Dormand and Prince developed different RK5(4) formulae which all have small principal truncation terms in the fifth order and extended regions of absolute stability: RK5(4)7M, RK5(4)7S and RK5(4)6M [67]. In this work, the focus is on the formula RK5(4)7M also used by the *ode45* solver from *Matlab* and from *GNU Octave*. The related coefficients involved in Eqn 3.3.2 and 3.3.3 are summarized in Tab 3.1.

a_{ij}						$\hat{b}_i$	b_i
						$\frac{35}{384}$	$\frac{5179}{57600}$
$\frac{1}{5}$						0	0
$\frac{3}{40}$	$\frac{9}{40}$					$\frac{500}{1113}$	$\frac{7571}{16695}$
$\frac{44}{45}$	$-\frac{56}{15}$	$\frac{32}{9}$				$\frac{125}{192}$	$\frac{393}{640}$
$\frac{19372}{6561}$	$-\frac{25360}{2187}$	$\frac{64448}{6561}$	$-\frac{212}{729}$			$-\frac{2187}{6784}$	$-\frac{92097}{339200}$
$\frac{9017}{3168}$	$-\frac{355}{33}$	$\frac{46732}{5247}$	$\frac{49}{176}$	$-\frac{5103}{18656}$		$\frac{11}{84}$	$\frac{187}{2100}$
$\frac{35}{384}$	0	$\frac{500}{1113}$	$\frac{125}{192}$	$-\frac{2187}{6784}$	$\frac{11}{84}$	0	$\frac{1}{40}$

Table 3.1: Coefficients related to the formula RK5(4)7M. From Dormand and Prince [67].

Combining Eqn 3.3.2 - 3.3.3 and Tab 3.1, it is possible to estimate the local truncation error in the p^{th} order formula as

$$E_{n+1} = \mathbf{y}_{n+1} - \hat{\mathbf{y}}_{n+1}. \tag{3.3.4}$$

This latter enables to control the truncation error through the step size computation. To do so, considering the n^{th} step, the process previously explained is repeated for different step sizes $h_{n,(m)}$ until reaching a certain

accuracy. For each new sub-step, the step size is updated by a locally optimal step-size strategy proposed by Shampine [68] as

$$h_{n,(m+1)} = 0.9\ h_{n,(m)} \left[\frac{\varepsilon}{\left\| E_{n+1,(m)} \right\|_\infty} \right]^{1/p+1}, \tag{3.3.5}$$

with ε being an imposed tolerance. Nevertheless, a minimum step size value $h_{\min}$ is imposed to break the process in order to avoid an excessive computational cost despite the loss of precision. There are now all the constitutive elements to establish the global process summarized by algorithm 2.

Algorithm 2 Dormand-Prince ODEs solver.

Provide: x_0, $\hat{\mathbf{y}}_0$ and h_0;

$n \leftarrow 0$;

while $x_n \leq x_{end}$ **do**

  $h_{n,(0)} \leftarrow h_n$;

  $m \leftarrow 0$;

  do

    Compute $\hat{\mathbf{y}}_{n+1,(m)}$ and $\mathbf{y}_{n+1,(m)}$ from Eqn 3.3.2 - 3.3.3 and Tab 3.1 with $h_{n,(m)}$, x_n and $\hat{\mathbf{y}}_n$;

    Compute the truncation error $E_{n+1,(m)}$ with Eqn 3.3.4;

    Compute the new step size $h_{n,(m+1)}$ with Eqn 3.3.5;

    $m \leftarrow m + 1$;

  while $\left\| E_{n+1,(m-1)} \right\|_\infty > \varepsilon \quad \& \quad h_{n,(m)} > h_{\min}$;

  $x_{n+1} \leftarrow x_n + h_{n,(m-1)}$;

  $\hat{\mathbf{y}}_{n+1} \leftarrow \hat{\mathbf{y}}_{n+1,(m-1)}$;

  Store $(x_{n+1}\ ;\ \hat{\mathbf{y}}_{n+1})$;

  $h_{n+1} \leftarrow h_{n,(m-1)}$;

  $n \leftarrow n + 1$;

end

3.4 Algorithms Validation

In order to verify the implementation, algorithms 1 and 2 are both assessed by considering different test cases. The Dormand-Prince solver is first evaluated considering the two-body gravitational problem. Then, the shooting process is applied for different FS constants and the obtained results are compared with respect to the literature.

3.4.1 Two-Body Gravitational Problem

According to Dormand and Prince [67], the two-body gravitational problem represents a severe test for the step-size procedure given that the step size must vary up to two orders of magnitude. This therefore seems to be a relevant case study to evaluate the robustness and the accuracy of the implemented solver. The related system of equations is given by

$$
\begin{aligned}
\partial_t y_1 &= y_3, \\
\partial_t y_2 &= y_4, \\
\partial_t y_3 &= -y_1 / \left(y_1^2 + y_2^2\right)^{3/2}, \\
\partial_t y_4 &= -y_2 / \left(y_1^2 + y_2^2\right)^{3/2},
\end{aligned}
\tag{3.4.1}
$$

with ∂_t corresponding to the partial time derivative. Subsequently, the initial conditions are

$$
\begin{aligned}
y_1(0) &= 1 - e, \\
y_2(0) &= 0, \\
y_3(0) &= 0, \\
y_4(0) &= \sqrt{(1+e)/(1-e)},
\end{aligned}
\tag{3.4.2}
$$

where e denotes the eccentricity imposed at 0.9 for this application.

Such a problem is solved over a period of time ranging from 0 to 20 seconds. The solver parameters are imposed as

$$\varepsilon = 10^{-11} \qquad \text{and} \qquad h_{\min} = 10^{-8} \quad [\text{s}].$$

For comparison purposes, a reference solution is obtained from the *ode45* solver in *Matlab* [69] by imposing both absolute and relative tolerances at 10^{-8}. Such a value enables to obtain roughly the same amount of time steps and computational time as for the implemented solver with the current parameters. Relying on the results in Fig 3.2, it is possible to observe a good correspondence between both solvers, which enables to validate algorithm 2 for this critical problem. Furthermore, the comparison of the step size through the iterations in Fig 3.3 reveals similar trends between the two cases.

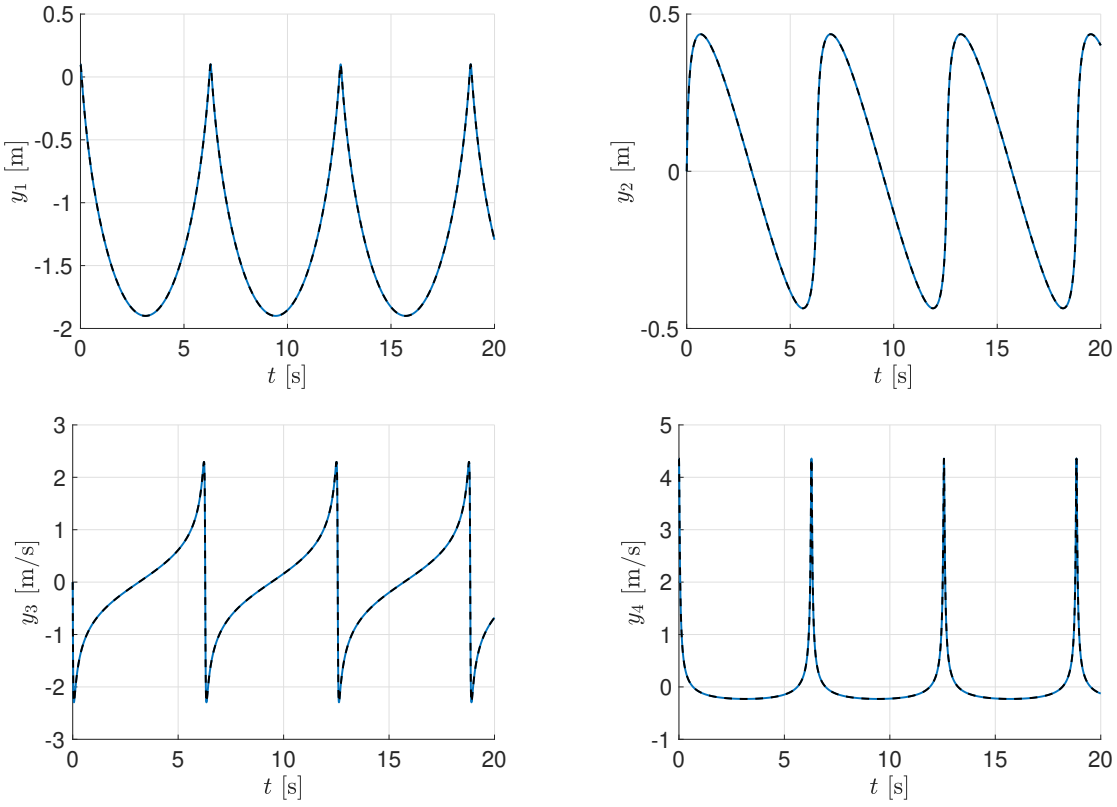

Figure 3.2: Solution of the two-body gravitational problem from algorithm 2 (solid line, blue) and from the *Matlab ode45* solver (dashed line, black).

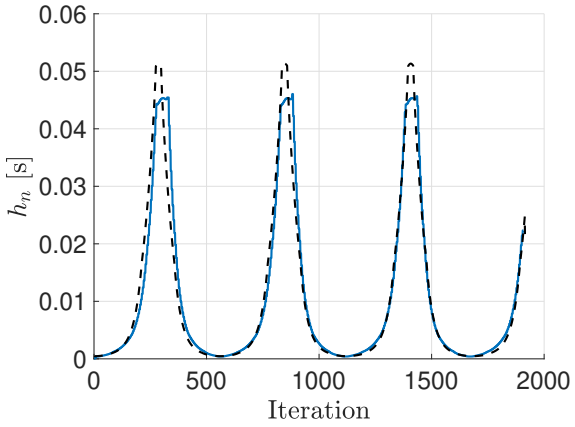

Figure 3.3: Step size h_n through the iterations used by the implemented solver (solid line, blue) and by the *Matlab ode45* solver (dashed line, black).

3.4.2 Accuracy of the Shooting Process

In a second phase, the shooting angles obtained from the implemented process are compared with external sources. All of them use the same shooting algorithm but differ in the means to solve the IVPs. As done in this work, the first reference [66] uses the Dormand-Prince pair. In the second source [65], Asaithambi solves the system of equations by recursive evaluation of Taylor's coefficients. Finally, in the third one [70], Salama uses an extended one-step method of order 5 to solve the Falkner-Skan equation.

As a starting point, the FS constants are imposed as

$$\beta_0 = 0.5 \qquad \text{and} \qquad \beta = 0, \tag{3.4.3}$$

in such a way that Eqn 3.1.1 now corresponds to the Blasius equation describing a self-similar boundary layer over a flat plate. In order to fit with the reference benchmark, the shooting parameters are imposed as

$$\varepsilon_p = 10^{-10}, \qquad \alpha_0 = 1, \qquad \eta_{\infty,0} = 1.$$

Regarding the Dormand-Prince solver, the minimum time step $h_{n,\min}$ is arbitrarily imposed at 10^{-8} and the tolerance on the local truncation error ε at 10^{-11} and this, for the rest of this work. The results obtained for different values of ε_q are presented in Tab 3.2. Note that due to the lack of information about the rounding process of the reference works, an additional decimal is kept for each tolerance value. This comparison enables to achieve an excellent correspondence between the different sources and to validate the results for this current setup.

ε_q \ α	Current	[66]	[65]	[70]
10^{-3}	0.3322	0.332	0.332	0.332
10^{-5}	0.332059	0.33206	0.33206	0.33205
10^{-7}	0.33205734	0.3320573	0.3320573	0.3320573
10^{-9}	0.33205733633	0.332057336	0.332057336	0.332057336
10^{-11}	0.3320573362 16	0.33205733621	0.33205733629	0.33205733663

Table 3.2: Shooting angle α considering a flat plate, i.e. $\beta_0 = 0.5$ and $\beta = 0$, with the shooting parameters imposed as $\varepsilon_p = 10^{-10}$, $\alpha_0 = 1$ and $\eta_{\infty,0} = 1$.

Then, it seems particularly interesting to focus on the flow over a wedge of half angle $\pi\beta/2$ by setting $\beta_0 = 1$ [71]. This case will be used in the following of this work to model a laminar flow around an airfoil.

In this study, β ranges from -0.1988 to 2.0 in Tab 3.3 and from 10 to 40 in Tab 3.4. Note that such a range is not restricted to typical values related to the wedge half angle. The main reason is that, beyond modeling a physical setup, it also seems relevant to consider such values to test the limit of the implementation and to assess the robustness. In addition, the shooting parameters are imposed as

$$\varepsilon_p = 10^{-6}, \qquad \varepsilon_q = 10^{-6}, \qquad \alpha_0 = 1, \qquad \eta_{\infty,0} = 10^{-3}.$$

Considering $\alpha_0 = 1$, the simulations reveal that the initial value $\eta_{\infty,0}$ has to be sufficiently small in order to obtain a convergence, especially for high β values. This observation agrees with Rogers [72] stating that for small $\eta_{\infty,0}$ the trial solution can behave roughly in the same way as the correct solution and this, despite a bad estimation of α_0. This is also in line with Asaithambi [65] attesting that $\eta_{\infty,0}$ has to be weaker with an increasing β value. For the interval of β values considered in this analysis, a value of $\eta_{\infty,0}$ comprised between 10^{-2} and 10^{-3} enables to obtain a good robustness regarding the convergence. Finally, the results summarized in Tab 3.3 and 3.4 enable to achieve an excellent match with the external sources and thus to validate the implementation.

β \ α	Current	[66]	[65]	[70]
2.0000	1.6872182	1.687218	1.687218	1.687218
1.0000	1.2325877	1.232587	1.232589	1.232588
0.5000	0.9276800	0.927680	0.927680	0.927680
0.0000	0.4696000	0.469600	0.469600	0.469600
-0.1000	0.3192698	0.319270	0.319270	0.319270
-0.1500	0.2163614	0.216362	0.216361	0.216362
-0.1800	0.1286362	0.128636	0.128637	0.128637
-0.1988	0.0052182	0.005222	0.005225	0.005226

Table 3.3: Shooting angle α with $\beta_0 = 1$, $\varepsilon_p = 10^{-6}$, $\varepsilon_q = 10^{-6}$, $\alpha_0 = 1$ and $\eta_{\infty,0} = 10^{-3}$.

β \ α	Current	[66]	[65]	[70]
40	7.3147850	7.314785	7.314785	7.314785
30	6.3382086	6.338208	6.338209	6.338208
20	5.1807180	5.180718	5.180718	5.180718
15	4.4914869	4.491486	4.491487	4.491487
10	3.6752341	3.675234	3.675234	3.675234

Table 3.4: Shooting angle α with $\beta_0 = 1$, $\varepsilon_p = 10^{-6}$, $\varepsilon_q = 10^{-6}$, $\alpha_0 = 1$ and $\eta_{\infty,0} = 10^{-3}$.

3.5 Wall-Shear Stress Computation

At this point, it is possible to estimate the wall-shear stress τ_w for different geometries by first providing the suitable FS constants β - β_0 and deducing the corresponding shooting angle α from algorithms 1 and 2. The wall-shear stress can then be computed from the obtained α and the local value of the external flow velocity U_e deduced from the Navier-Stokes solution at the current iteration. In the following, the related formulae are presented respectively for a flat plate, a wedge and an airfoil.

3.5.1 Flat Plate

Considering the Blasius equation, the wall-shear stress is given by

$$\tau_w = \mu \frac{\partial u}{\partial x_n}\bigg|_{x_n=0} = \mu \sqrt{\frac{U_\infty^3}{\nu x_s}} \frac{d^2 f}{d\eta^2}\bigg|_{\eta=0} = \mu \sqrt{\frac{U_\infty^3}{\nu x_s}}\ \alpha, \tag{3.5.1}$$

with U_∞ denoting the free-stream velocity and ν and μ respectively the kinematic and dynamic molecular viscosity. The variable x_s corresponds to the distance in the wall-tangential direction with respect to the leading edge. For this simple case, there is no need to extract any information from the solution since the free-stream speed is known *a priori*.

3.5.2 Wedge

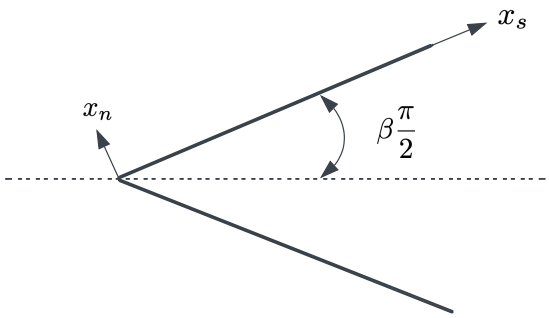

Figure 3.4: Wedge with a half-angle $\beta\pi/2$.

Then, studying the flow over a wedge of half-angle $\pi\beta/2$, the FS equation can be simplified by imposing $\beta_0 = 1$. For this particular case, the similarity variable is written as

$$\eta = x_n \sqrt{\frac{1}{2-\beta}\frac{U_e}{\nu x_s}}, \tag{3.5.2}$$

and the external flow velocity as

$$U_e\left(x_s\right) = K x_s^{\beta/(2-\beta)}, \tag{3.5.3}$$

with K a constant. As schematized in Fig 3.4, the distance along the wall with respect to the stagnation point is noted x_s and the one in the wall-normal direction x_n. Subsequently, the wall-shear stress is expressed as

$$\tau_w = \mu\ \frac{\partial u}{\partial x_n}\bigg|_{x_n=0} = \mu \sqrt{\frac{1}{2-\beta}\frac{U_e^3}{\nu x_s}} \frac{d^2 f}{d\eta^2}\bigg|_{\eta=0} = \mu \sqrt{\frac{1}{2-\beta}\frac{U_e^3}{\nu x_s}}\ \alpha. \tag{3.5.4}$$

Regarding the inviscid speed $U_e\left(x_s\right)$, it is possible to choose between two approaches. The first one consists in approximating the inviscid speed directly from the tangential velocity field $u_t\left(x_s, x_n\right)$ such that

$$U_e\left(x_s\right) \simeq u_t\left(x_s, x_n = h_w\right), \tag{3.5.5}$$

with h_w the height of extraction. Eqn 3.5.5 is perfectly verified if the tangential speed is taken exactly at the boundary layer edge whose location is, however, unknown *a priori*. This method was employed by Dauricio

et al. [13] for a flow around a NACA0012 by considering a linear growth of h_w with respect to x_s. In this work, the authors concluded that it is crucial to ensure a growth rate sufficiently high in order to avoid an extraction too close to the wall which leads to information that does not represent the external flow. On the other side, it is necessary to limit this rate in order to stay close enough to the boundary layer edge vicinity. The main weakness of this technique is therefore its strong sensitivity with respect to the h_w parameter and the required trial and error in order to get closer to the boundary layer edge during the extraction process.

As an alternative, $U_e\,(x_s)$ can be computed from the static pressure field $p\,(x_s, x_n)$. Relying on the boundary layer equation

$$\frac{\partial p}{\partial x_n} = 0, \tag{3.5.6}$$

it is acceptable to assume a constant pressure across the boundary layer. Hence, conversely to the velocity field, the pressure extraction offers a much better robustness with respect to the height h_w. The relation linking $U_e(x_s)$ and $p(x_s)$ can be expressed by deriving Bernoulli's equation with respect to x_s. The resulting equation is written as

$$U_e(x_s)\frac{\mathrm{d}U_e(x_s)}{\mathrm{d}x_s} = -\frac{1}{\rho}\frac{\mathrm{d}p(x_s)}{\mathrm{d}x_s}. \tag{3.5.7}$$

Thus, combining Eqn 3.5.3 and 3.5.7 leads to

$$K = \sqrt{\frac{-\frac{1}{\rho}\frac{dp}{dx_s}}{\frac{\beta}{(2-\beta)}\, x_s^{(3\beta-2)/(2-\beta)}}}. \tag{3.5.8}$$

From that, it is possible to estimate $U_e(x_s)$ from the pressure gradient by injecting Eqn 3.5.8 into Eqn 3.5.3.

3.5.3 Airfoil

Lastly, the wall-shear stress computation is established for flow around an airfoil. Relying on Dauricio et al. [13], this can be done by assuming that the dynamics of the flow over the airfoil is, at each location along the surface, similar to one describing a flow over a wedge whose half angle is related to the geometric angle between the wall-tangent and the streamwise direction. Sticking to this assumption, the wall-shear stress is deduced from Eqn 3.5.4 and the related constants can be expressed as

$$\beta_0 = 1, \tag{3.5.9}$$

$$\beta = \kappa - |\kappa|\left[1 - \chi\left(\frac{x}{c}, \mathrm{Re}_c\right)\right], \tag{3.5.10}$$

with x the distance in the chordwise direction and κ being defined such that $\pi\kappa/2$ is the geometric angle between the wall-tangent and the streamwise direction as shown in Fig 3.5. This latter is computed as

$$\kappa = \frac{2}{\pi}\cos^{-1}(\hat{\mathbf{t}} \cdot \hat{\mathbf{s}}), \tag{3.5.11}$$

where $\hat{\mathbf{t}}$ and $\hat{\mathbf{s}}$ respectively refer to the unit wall-tangent and the unit streamwise vector.

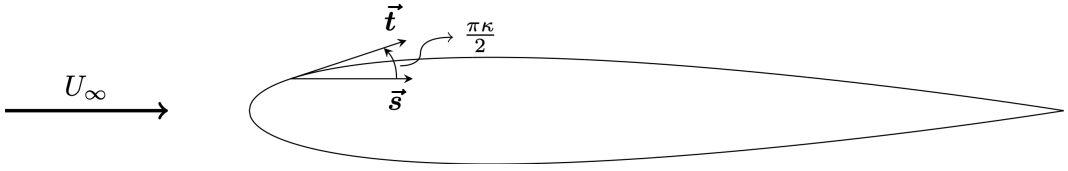

Figure 3.5: Illustration of the geometry-related parameter κ. $\vec{\mathbf{t}}$ and $\vec{\mathbf{s}}$ are respectively aligned with the wall-tangent and the streamwise direction. From Dauricio et al. [13].

The dynamics of a flow over a wedge itself is not sufficient to take into account the effect of the boundary layer along the surface. Only considering the geometric angle would be equivalent to considering a flow accelerating as much as an inviscid flow, thus leading to an overestimation of the wall-shear stress. In fact, the velocity gradient is dissipated by the viscosity, giving rise to the boundary layer. In response to that, Dauricio et al. introduced the correction function expressed as

$$\chi\left(\frac{x}{c}, Re_c\right) = \frac{1 - (\sqrt{x/c})e^{-ARe_c}}{1 + e^{-ARe_c}}, \tag{3.5.12}$$

with A a coefficient and the chord Reynolds number expressed as

$$Re_c = \frac{U_\infty c}{\nu}, \tag{3.5.13}$$

where U_∞ stands for the free-stream velocity magnitude and c the chord length. It is important to underline that this function only involves the distance in the chordwise direction x and not the distance along the surface x_s with respect to the stagnation point solely used in the wall-shear stress computation in Eqn 3.5.4. Subsequently, the correction turns off in the inviscid limit such as

$$\lim_{Re_c \to \infty} \chi \to 1, \tag{3.5.14}$$

which is consistent with its physical motivation.

The parameter A from Eqn 3.5.12 is kept free in order to tune the angle correction function. Dauricio et al. found that in the case of a NACA0012, $A = 2.63 \cdot 10^{-5}$ seems to be a suitable value. This value will thereby be imposed as the default one in the rest of this study.

As regards the inviscid speed $U_e\,(x_s)$ involved in Eqn 3.5.4, it is once again possible to estimate it from the velocity field using Eqn 3.5.5. The second option involving the static pressure gradient developed in Sec 3.5.2 does not, however, seem appropriate for this case since the FS equation is assumed to be verified locally with a given β value. Therefore, Eqn 3.5.3 cannot be used to be combined with the derivative of Bernoulli's equation. Instead, Bernoulli's principle in its standard formulation is applied along a streamline starting from the inlet. This leads to

$$p\,(x_s) + \frac{1}{2}\rho\, U_e^2\,(x_s) = p_\infty + \frac{1}{2}\rho\, U_\infty^2, \tag{3.5.15}$$

where p_∞ is the free-stream static pressure and U_∞ the free-stream velocity norm. The inviscid speed is thus expressed as

$$U_e\,(x_s) = U_\infty \sqrt{1 - c_p\,(x_s)}, \tag{3.5.16}$$

with c_p the pressure coefficient as

$$c_p\,(x_s) = 2\,\frac{p\,(x_s) - p_\infty}{\rho\, U_\infty^2}. \tag{3.5.17}$$

3.5.4 LWM and Incompressible Navier-Stokes Solver

This section enables thereby to describe the inputs and outputs as well as what is inside the laminar wall model. This black box can now be added to the incompressible Navier-Stokes solver described in Sec 2. Extracting the static pressure at the wall vicinity from the solution at the current step, the wall model is able to provide the wall-shear stress distribution. This latter is then used as a boundary condition for the next iteration by the solver. In the following of this work, the pressure is extracted by default at the second point off the wall.

Chapter 4

Laminar Flows over a Straight Wall

In the first instance, a validation phase of the laminar wall model (LWM) is carried out by considering flows over a straight wall: the stagnation point flow - so-called the Hiemenz flow [71] - and a flow over a flat plate. For these simple geometries, a Cartesian grid fitting with the wall is used and the numerical domain does not present any cut cells. Subsequently, the kinematic viscosity is in both cases imposed as sufficiently high to avoid any risk of transition, which ensures a fully laminar regime. So, in the absence of turbulence and taking into account the symmetry of the flows in the spanwise direction, the numerical domains are described in a two-dimensional space.

The main purpose of this section is to assess the accuracy of the LWM by carrying a comparison with respect to the wall-resolved (WR) case using the traditional no-slip condition. To that end, the wall-shear stress from the LWM is compared to the one computed from the WR solution. For this latter, the velocity gradient is obtained by applying a second order upwards finite difference method written as

$$f'(x_i) \simeq a \cdot f(x_i) + b \cdot f(x_{i+1}) + c \cdot f(x_{i+2}), \tag{4.0.1}$$

with

$$\begin{cases} a = -(b+c), \\ b = \dfrac{\Delta x_{i+2}}{\Delta x_{i+1}\Delta x_{i+2} - \Delta x_{i+1}^2}, \\ c = \dfrac{\Delta x_{i+1}}{\Delta x_{i+2}\Delta x_{i+1} - \Delta x_{i+2}^2}, \end{cases} \tag{4.0.2}$$

and where

$$\begin{cases} \Delta x_{i+1} = x_{i+1} - x_i, \\ \Delta x_{i+2} = x_{i+2} - x_i. \end{cases}$$

Additionally, the LWM is compared with a turbulent wall model (TWM) already implemented in INCA. This latter provides an estimate of the wall-shear stress by solving the standard logarithmic law [29]. The purpose of this comparison is to assess the effect of the fully turbulent flow assumption applied on a laminar case and the potential improvements brought by the LWM.

4.1 Flat Plate

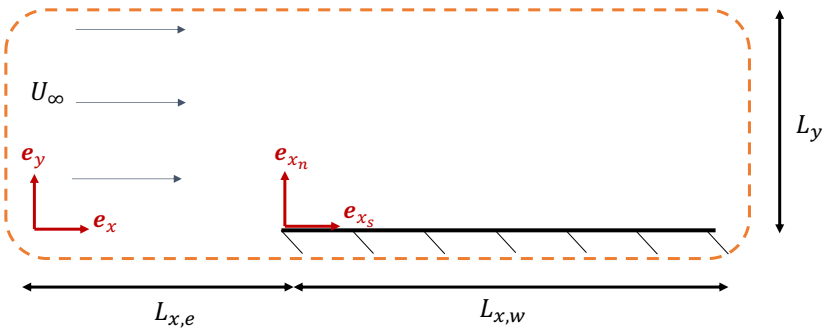

Figure 4.1: Description of the numerical setup considering a flat plate. The computational domain is represented by the orange dashed box and includes a slip region located upstream of the wall.

The laminar wall model (LWM) is first applied to one of the simplest configurations, namely flow over a flat plate. Fig 4.1 illustrates the numerical setup used to validate the LWM. The domain includes an entrance region, defined as a slip surface, which is followed by a horizontal wall. The entrance length and the wall length are respectively imposed as $L_{x,e} = 30$ [m] and $L_{x,w} = 80$ [m] with a height fixed as $L_y = 30$ [m]. The inlet corresponds to a uniform horizontal flow with a unit speed $U_\infty = 1$ [m/s] and a zero pressure gradient. The outlet and the upper boundary are specified using a first order Neumann boundary condition for velocities and a zero static pressure. The domain is then meshed using a hyperbolic stretching in both vertical and horizontal direction in order to capture the physics at the wall and the steep change of speed at the leading edge. The stretching factor is imposed at 1.5 in the vertical direction, at 1.2 along the entrance and at 1.01 over the wall. In the following, the number of elements used along the entrance and along the wall are respectively imposed as $N_{x_s,e} = 50$ and $N_{x_s} = 200$. Finally, the fluid is considered as incompressible with a unit density and a kinematic viscosity $\nu = 1 \cdot 10^{-3}$ [m^2/s].

4.1.1 Laminar Wall Model

For this configuration, the laminar wall-shear stress can be directly deduced *a priori* from the Blasius solution in Eqn 3.5.1, given that the inviscid speed equals the free-stream velocity U_∞. Thus, the accuracy of the wall-shear stress provided by the LWM is independent of the mesh resolution in the wall-normal direction.

In order to assess the validity of such a model, a wall-resolved (WR) reference solution is first obtained by studying the evolution of the wall-shear stress with respect to the wall-normal resolution N_{x_n}. The resulting Fig 4.2a brings out that the mesh with $N_{x_n} = 600$ is sufficiently fine to reach the convergence and the related solution will be kept as the benchmark for the rest of this analysis. Subsequently, it is important to highlight that this solution only presents a good correspondence with respect to the Blasius friction estimate sufficiently far away from the leading edge. Close to this region, the reference friction is larger, as globally observed with the other mesh resolutions. It is therefore possible to conclude that the flow needs a certain distance to establish itself as self-similar and, hence, that the LWM is unsuitable near the leading edge of the plate. On the other side, it is also necessary to keep in mind the artificial effects from the outlet boundary condition. In response to these two considerations, the analysis is re-centered between $4.5 \cdot 10^4$ and $5.5 \cdot 10^4$ where the WR reference solution presents a good match with the self-similar prediction.

Regarding the turbulent wall model (TWM), the convergence study in Fig 4.2b reveals a significant underestimation with respect to the WR reference solution at the leading edge vicinity. This error is all the more pronounced with a weaker resolution. Focusing on the previously defined self-similar region, the log-law enables a steep reduction of the error with respect to the benchmark friction from $N_{x_n} = 100$ to $N_{x_n} = 200$. Nevertheless, the TWM does not present a monotonic convergence. It is indeed possible to observe a better accuracy with $N_{x_n} = 200$ than with $N_{x_n} = 400$ through most of the self-similar region.

In order to quantify these previous observations, the relative error with respect to the WR reference solution on the friction is computed in $Re_{x_s} = 4.5 \cdot 10^4$ and $Re_{x_s} = 5.5 \cdot 10^4$ for the three cases, see Fig 4.3. As deduced from Fig 4.2b, the TWM does not present a monotonic convergence at the two points, which is illustrated by the significant increase of the error from $N_{x_n} = 200$ to 400. On the other side, considering the coarsest grid in $N_{x_n} = 100$, it is possible to state that the LWM offers a considerable improvement with respect to both the WR solution and the TWM at both locations. This demonstrates the interest of the LWM. Then, the gain becomes weaker with an increasing resolution and the WR solution ends up being more accurate between $N_{x_n} = 200$ and 400 in $Re_{x_s} = 5.5 \cdot 10^4$.

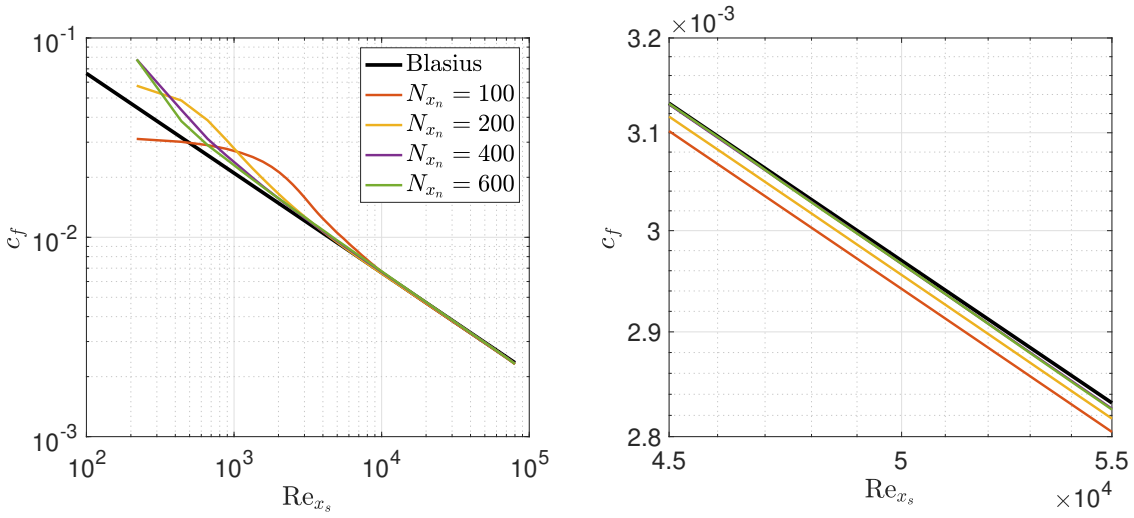

(a) Wall-resolved (WR).

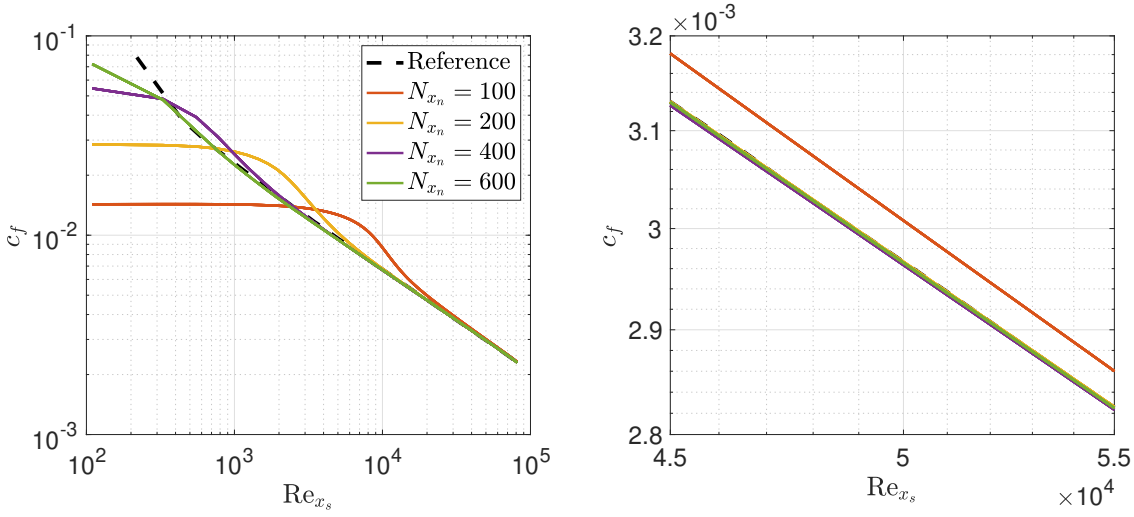

(b) Turbulent wall model (TWM).

Figure 4.2: Skin friction coefficient c_f for different grid resolutions in the wall-normal direction N_{x_n}. The reference friction corresponds to the WR solution obtained with $N_{x_n} = 600$ and $N_{x_s} = 200$ (dashed line, black).

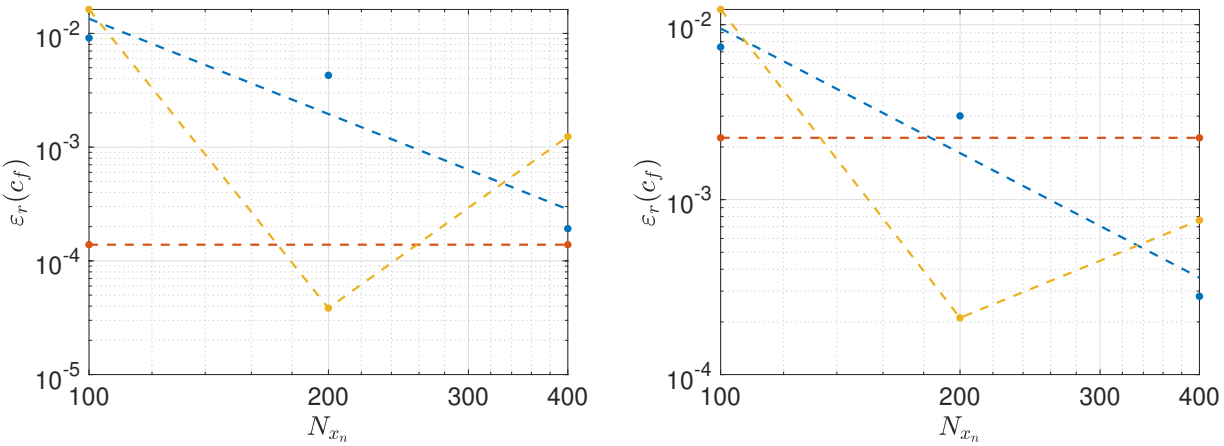

(a) $\mathrm{Re}_{x_s} = 4.5 \cdot 10^4$. **(b)** $\mathrm{Re}_{x_s} = 5.5 \cdot 10^4$.

Figure 4.3: Relative error ε_r with respect to the WR reference solution ($N_{x_n} = 600$ and $N_{x_s} = 200$) on the wall-shear stress obtained from the WR solution (blue points), from the LWM (orange points) and from the TWM (yellow points).

4.1.2 Boundary Layer

Then, it seems relevant to investigate the boundary layer obtained with the three wall treatments. To that end, the displacement thickness δ^* and the momentum thickness θ are calculated and compared with the results from the Blasius boundary layer written as [73]

$$\delta^* = 1.72\sqrt{\frac{\nu x}{U_\infty}} \qquad \text{and} \qquad \theta = 0.665\sqrt{\frac{\nu x}{U_\infty}}. \tag{4.1.1}$$

Considering an incompressible flow, these two parameters are expressed as [73]

$$\delta^*(x) = \int_0^{L_y} \left(1 - \frac{u(x,y)}{U_e}\right) \mathrm{d}y, \tag{4.1.2}$$

$$\theta(x) = \int_0^{L_y} \frac{u(x,y)}{U_e}\left(1 - \frac{u(x,y)}{U_e}\right) \mathrm{d}y, \tag{4.1.3}$$

with $u(x,y)$ denoting the wall-tangential speed and, for this particular setup, U_e corresponding to the free-stream velocity U_∞. It is thus possible to estimate them directly from the discrete solutions as

$$\delta^*(x_j) \simeq \sum_{i=1}^{N_{xn}} \left(1 - \frac{u(x_j,y_i)}{U_e}\right) \Delta y_i, \tag{4.1.4}$$

$$\theta(x_j) \simeq \sum_{i=1}^{N_{xn}} \frac{u(x_j,y_i)}{U_e}\left(1 - \frac{u(x_j,y_i)}{U_e}\right) \Delta y_i, \tag{4.1.5}$$

with $j = 1, ..., N_{x_s}$.

In this analysis, the WR reference solution ($N_{x_n} = 600$) and the results related to the LWM and TWM with $N_{x_n} = 400$ are used to estimate these two boundary layer parameters. From both displacement and momentum thickness in Fig 4.4a and Fig 4.4b, it is first possible to observe an acceptable match between the Blasius boundary layer and both WR case and TWM. There is, however, a significant underestimation for the LWM, all the more pronounced with the displacement thickness. To understand the cause of this gap, the focus is on the wall-shear stress coefficient in Fig 4.4c. Conversely to the TWM, the wall-shear stress

predicted from the Blasius solution and used by the LWM leads to an important underestimation close to the leading edge compared to the reference solution. As explained in the previous section, that is a direct consequence of the fact that the self-similarity does not hold in this region. Based on this observation, one can speculate that this offset in momentum loss is due to the local error in wall-shear stress around the leading edge, which impacts the whole solution by propagating downstream.

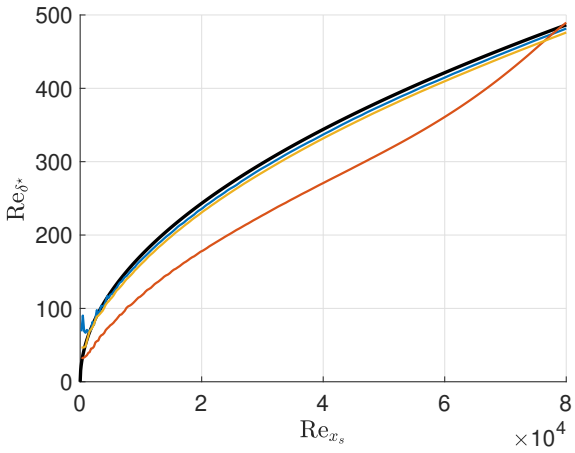

(a) Displacement thickness.

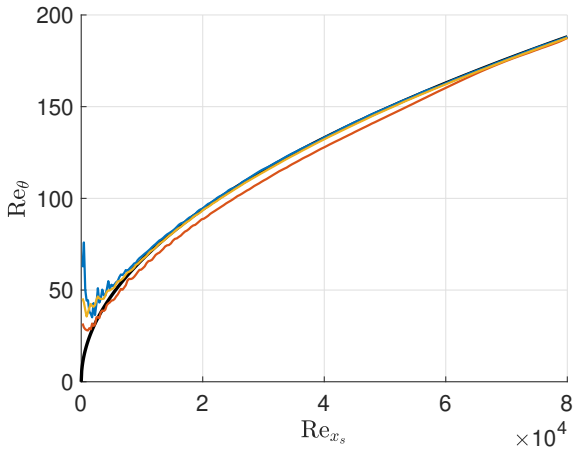

(b) Momentum thickness.

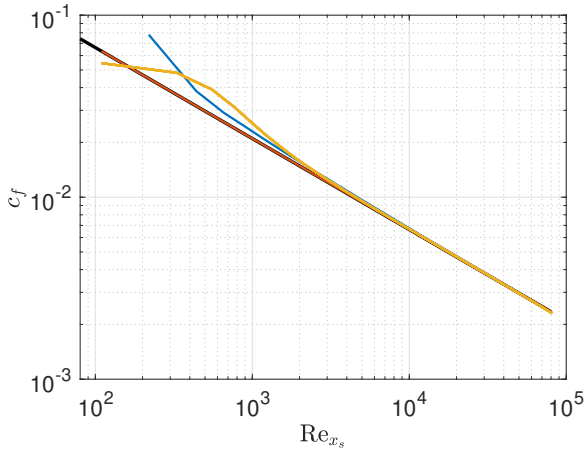

(c) Skin friction coefficient.

Figure 4.4: Boundary layer thickness and skin friction coefficient related to the Blasius solution (black line), to the WR reference solution (blue line), to the TWM with $N_{x_n} = 400$ (yellow line) and to the LWM with $N_{x_n} = 400$ (orange line).

To overcome this underestimation, an improved version of the LWM is proposed: instead of assuming a self-similar boundary layer through the whole domain, the model switches between a linear approximation $\tau_{w,\mathrm{lin}}$ and the Blasius estimate $\tau_{w,B}$ to approximate the local wall-shear stress. The former is simply obtained as

$$\tau_{w,\mathrm{lin}}(x_i) = \frac{u_{i,1}}{\Delta y_{i,1}}, \tag{4.1.6}$$

with $u_{i,1}$ being the tangential speed at the first grid point off the wall and $\Delta y_{i,1}$ the related grid cell size in the wall-normal direction. The imposed wall-shear stress τ_w is defined as the maximum between these two approximations leading to

$$\tau_w = \max(\tau_{w,B}\ ,\ \tau_{w,\mathrm{lin}}). \tag{4.1.7}$$

Relying on the convergence study with the wall-resolved case in Fig 4.2a, it is expected to obtain $\tau_w = \tau_{w,\text{lin}}$ in most of the leading edge vicinity for the different considered resolutions.

The results obtained from the improved LWM with $N_{x_n} = 400$ are summarized in Fig 4.5. Starting with the friction in Fig 4.5c, it reveals that the linear approximation enables to obtain a higher wall-shear stress estimate up to $Re_{x_s} = 1.03 \cdot 10^4$ compared to the initial LWM and thus offers a better match with respect to the reference friction. The Blasius estimate is then imposed on the rest of the domain and the two LWMs differ only near the leading edge. Both Fig 4.5a and 4.5b bring out that the improved LWM leads to a significant enhancement in terms of boundary layer thickness estimation. It thereby proves *a posteriori* the assumption made on the origin of the momentum loss underestimation through the whole domain.

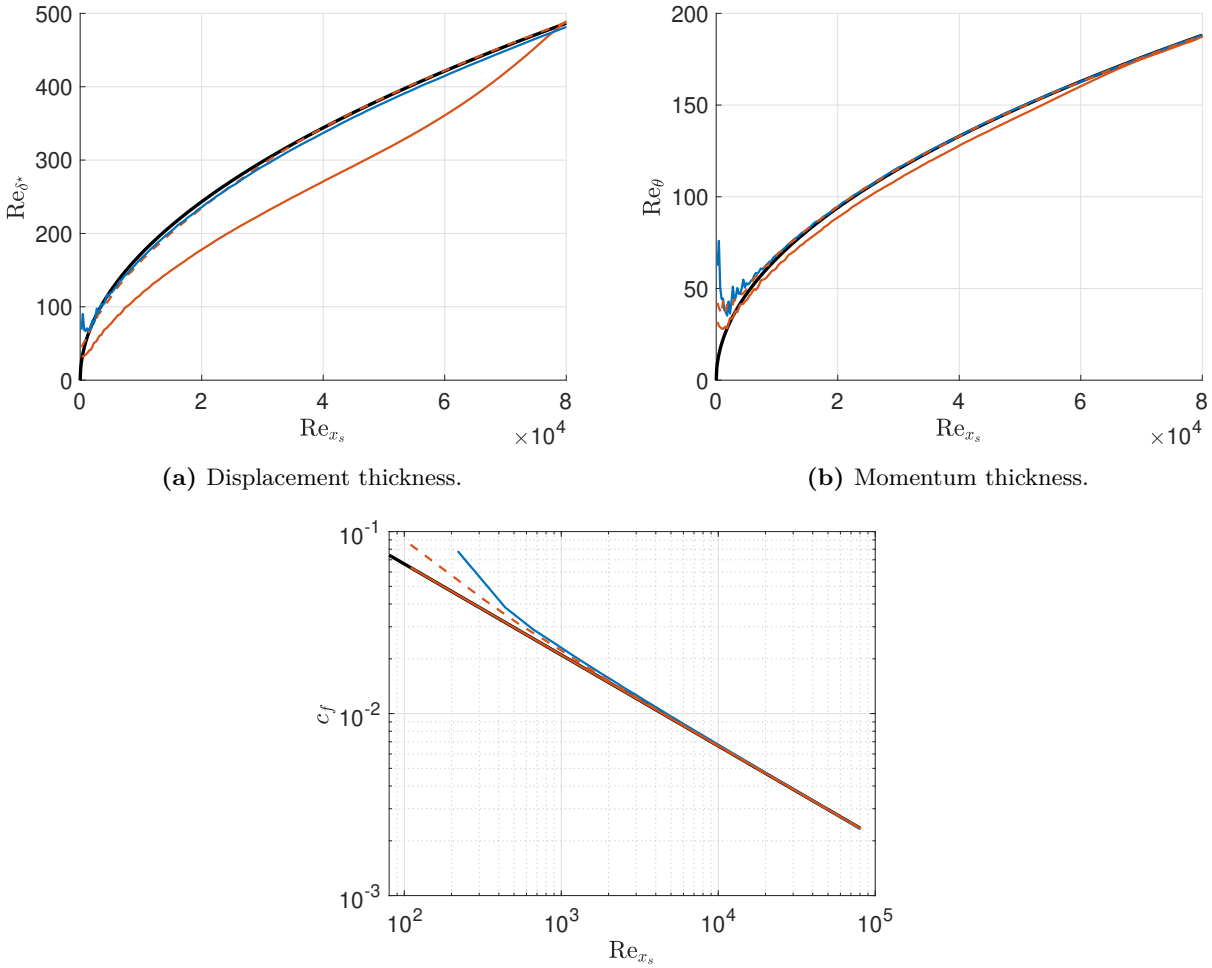

(a) Displacement thickness.

(b) Momentum thickness.

(c) Skin friction coefficient.

Figure 4.5: Boundary layer thickness and skin friction coefficient related to the Blasius solution (black line), to the WR reference solution (blue line), to the LWM imposing the Blasius wall-shear stress through the entire domain with $N_{x_n} = 400$ (solid line, orange) and to the improved LWM expressed in Eqn 4.1.7 with $N_{x_n} = 400$ (dashed line, orange).

Now that the boundary layer thickness has been analyzed, one can go deeper in detail by considering the velocity profiles from the reference solution and the solutions obtained from the LWM and from the improved LWM with $N_{x_n} = 400$. To that end, the velocity is extracted in $Re_{x_s} = 4.5 \cdot 10^4$, $5 \cdot 10^4$ and $5.5 \cdot 10^4$. Considering first the LWM, Fig 4.6 reveals that the error in terms of velocity is mainly due to the first grid point off the wall and this, at the three locations. It is possible to observe a significant excess of velocity at the first point leading to an offset with respect to the reference solution through the rest of the domain. The slopes

of the two velocity profiles are, however, relatively similar and the difference in local speed remains more or less constant until reaching U_∞. Therefore, one can conclude that the underestimation in wall-shear stress at the leading edge leads to a significant overestimation of the velocity at the first grid points through the whole domain, which explains the underestimation of the previously observed boundary layer thicknesses. Then, Fig 4.7 highlights the improvements brought by the second version of the LWM based on Eqn 4.1.7. For this case, both solutions present a good match as deduced from the boundary layer thickness analysis.

Although being a simple setup, the flat plate analysis enables to underline the importance of the self-similarity assumption. It is essential to verify its applicability in each region and this, for the overall accuracy of the solution. In some cases, like the leading edge of a flat plate, a linear approximation offers a much better accuracy locally, which leads to a weaker error downstream.

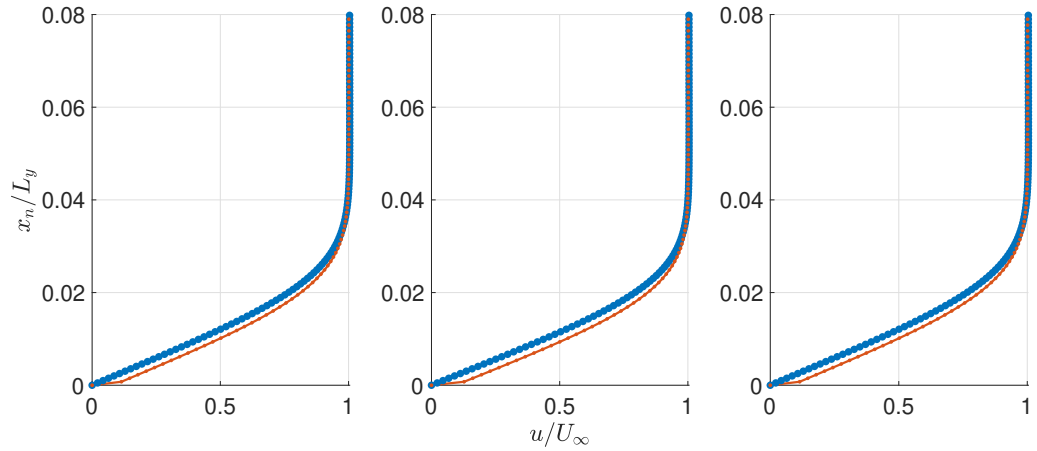

(a) Velocity profile.

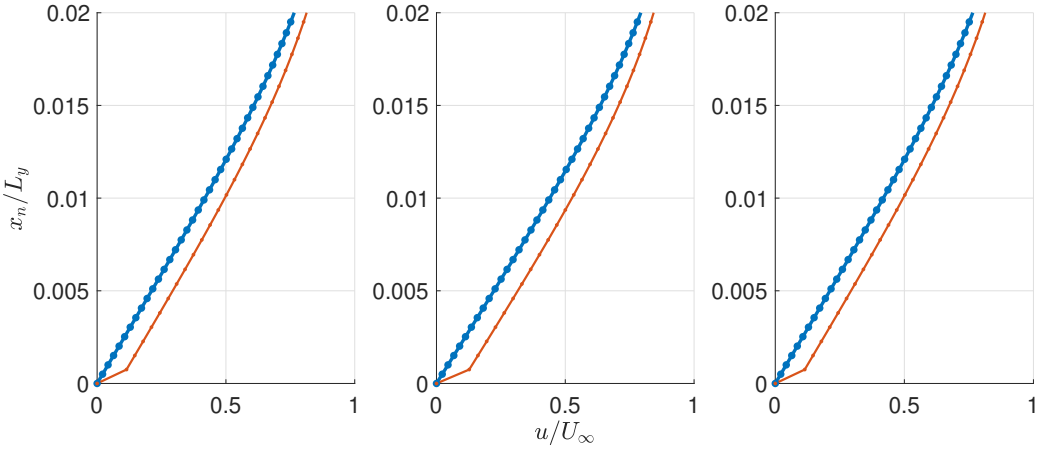

(b) Zoom on the wall vicinity.

Figure 4.6: Streamwise velocity profile in $Re_{x_s} = 4.5 \cdot 10^4$, $5 \cdot 10^4$ and $5.5 \cdot 10^4$ (left to right) from the WR reference solution with $N_{x_n} = 600$ (blue points) and from the LWM solution with $N_{x_n} = 400$ (orange points).

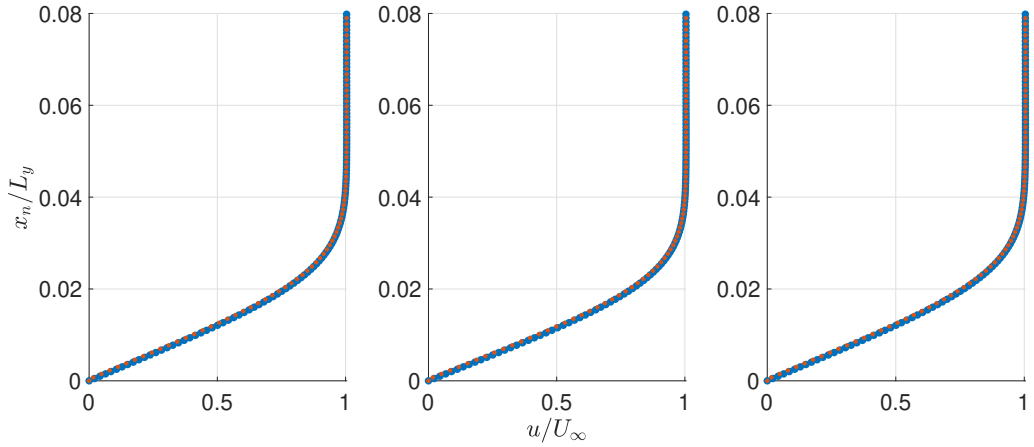

(a) Velocity profile.

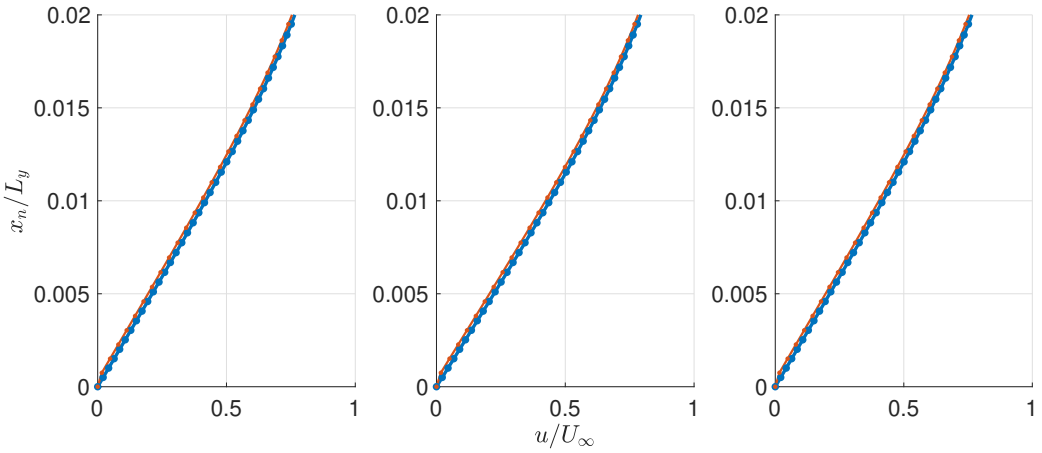

(b) Zoom on the wall vicinity.

Figure 4.7: Streamwise velocity profile in $Re_{x_s} = 4.5 \cdot 10^4$, $5 \cdot 10^4$ and $5.5 \cdot 10^4$ (left to right) from the WR reference solution with $N_{x_n} = 600$ (blue points) and from the improved LWM solution with $N_{x_n} = 400$ (orange points).

4.2 Stagnation Point Flow (Hiemenz Flow)

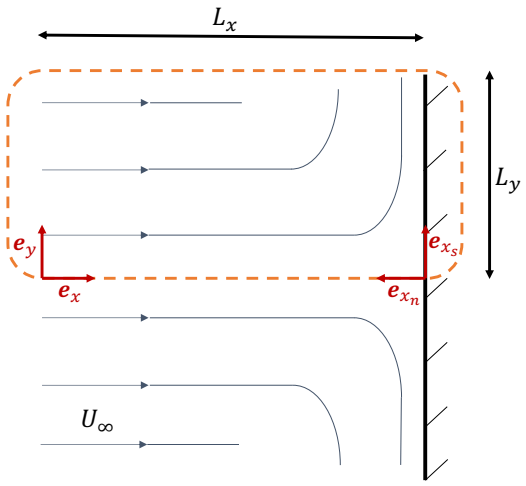

Figure 4.8: Illustration of the numerical setup considering a stagnation point flow. The computational domain is represented by the orange dashed box and is obtained by using the symmetry with respect to the stagnation point.

As a second setup, the 2D stagnation point flow is considered by simulating a uniform horizontal flow going towards a vertical wall, see Fig 4.8. Such a configuration can be approached by the self-similar theory considering the FS constants as $\beta = \beta_0 = 1$ [71]. Additionally, in order to limit the computational cost, only the upper half of the domain is modeled by taking advantage of the symmetry with respect to the stagnation point located in $(x_s, x_n) = \mathbf{0}$. The numerical domain presents a length $L_x = 0.5$ [m] and a half height $L_y = 4$ [m]. Regarding the boundary conditions, the incoming flow is represented by a horizontal uniform flow of speed norm $U_\infty = 1$ [m/s] and presenting a zero pressure gradient. Then, the upper limit is based on a first order Neumann boundary for velocities and a zero static pressure. Lastly, the symmetry is enforced at the lower side in $x_s = 0$. The domain is then meshed using $N_{x_s} = 300$ elements homogeneously distributed along the wall and N_{x_n} elements with a hyperbolic stretching in the wall-normal direction. The stretching factor is imposed at 1.5 in order to obtain a finer mesh at the wall vicinity while keeping an acceptable mesh size variation. Finally, the fluid is considered as incompressible with a unit density and a kinematic viscosity $\nu = 4 \cdot 10^{-4}$ [m^2/s].

4.2.1 Laminar Wall Model

Regarding the laminar wall model (LWM), the focus is first on the constant K involved in the inviscid speed $U_e(x_s)$ computation in Eqn 3.5.3. As illustrated in Fig 4.9, its value can be estimated at each point of the wall from Eqn 3.5.8, for all nonzero x_s, by taking the pressure gradient at the second point off the wall. In order to obtain a global K-value, two ways are investigated. It is either possible to average the K values over the entire wall (orange dashed line) or to choose a K-value at a single location imposed as the middle of the wall in this study (yellow dashed line). To decide between both options, it is important to remind that the self-similarity assumption does not hold at the vicinity of stagnation point and close to the outflow boundary. Indeed, on the one hand, the flow requires a certain distance from the stagnation point to establish itself as a self-similar solution. Additionally, from a numerical point of view, since

$$K = \sqrt{\frac{-\frac{1}{\rho}\frac{dp}{dx_s}}{x_s}} \sim \frac{1}{\sqrt{x_s}}, \tag{4.2.1}$$

any inaccuracy in terms of pressure gradient is strongly amplified at the stagnation point vicinity. On the other hand, the boundary condition at the outlet artificially introduces spurious effects impacting the solution. That can be visualized by the steep change in K in these two regions, whereas this latter remains relatively constant over the rest of the domain. It is thus possible to conclude that the average value does not seem

to be the best option in order to approximate the constant but taking the K-value at the middle of the wall seems more relevant. This second method will be kept for the rest of this analysis.

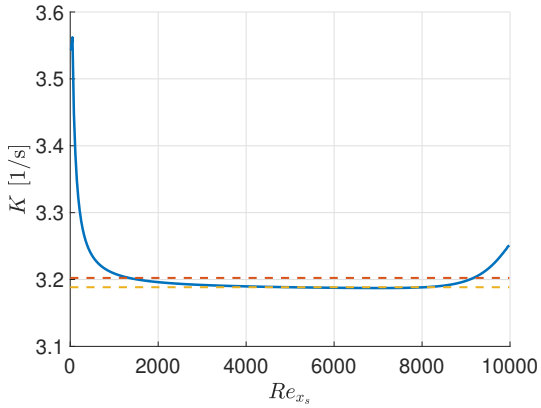

Figure 4.9: External flow velocity proportionality constant K from Eqn 3.5.8 at each point of the wall (solid line, blue), averaged on the wall (dashed line, orange) and at the middle of the wall in $Re_{x_s} = 5000$ (dashed line, yellow).

The method for calculating K being settled, it is possible to obtain the wall-shear stress estimate from Eqn 3.5.4 and assess its validity. To that end, it is first necessary to obtain a wall-resolved (WR) reference solution. A convergence study of the wall-shear stress is thereby performed with respect to the number of elements in the wall-normal direction N_{x_n} for $N_{x_s} = 300$. The resulting Fig 4.10a enables to consider the solution obtained with $N_{x_n} = 320$ as the reference.

Then, the same methodology is applied using the laminar wall model (LWM) and the turbulent wall model (TWM), giving respectively Fig 4.10b and Fig 4.10c. Qualitatively, the convergence study reveals that the LWM converges much earlier than the WR case and the TWM. It is indeed hard to distinguish the LWM results to the reference friction through the entire domain and this, from the coarsest resolution $N_{x_n} = 20$. This lead in convergence can be highlighted by focusing around the middle of the wall, as shown in the right-hand side of Fig 4.10. Subsequently, these results bring to light the interest of feeding the LWM with the pressure gradient instead of the velocity field. Although the pressure extraction is achieved at the second point off the wall, it is nevertheless possible to converge towards the reference solution by refining the grid. Obviously, this would not have been the case for a model fed with the velocity field, since the speed at the second point tends towards zero during the convergence study and does not represent the external flow behavior. For such a case, it is thereby necessary to determine a suitable fixed height of extraction by trails and errors to reach a converged grid state.

Regarding the TWM, the log-law is only able to reach an acceptable accuracy far away from the stagnation point and with a sufficiently high resolution. For most of the meshes, there is a significant overestimation of the speed derivative close to $x_s = 0$.

Afterwards, a more quantitative analysis can be achieved by computing the relative error in shear stress with respect to the WR reference solution ($N_{x_n} = 320$ and $N_{x_s} = 300$) at the middle of the wall, i.e. at $\mathrm{Re}_{x_s} = 5000$. To do so, the error in function of the wall-normal resolution is illustrated in Fig 4.11 for the three previously considered cases. This shows that for the entire range, the LWM enables to obtain a weaker error for each resolution compared to the WR case, which demonstrates the benefits of this model. Conversely, the TWM does not enable to reduce the error compared to the WR treatment and is therefore, as expected, not suitable for this application. Then, a linear curve fitting of the logarithmic representation enables to estimate the order of convergence. This leads to a scaling of the relative error ε_r as

$$\varepsilon_r \sim N_{x_n}^{-a}, \tag{4.2.2}$$

where $a = 1.81$ for the WR, $a = 1.77$ for the LWM and $a = 2.12$ for the TWM. The order of convergence is in all cases around 2, although slightly higher for the turbulent model. Since there is no significant difference

between the slopes of the WR case and the LWM, it is thus possible to conclude that the established laminar modeling enables to provide a significant improvement compared to the traditional no-slip condition.

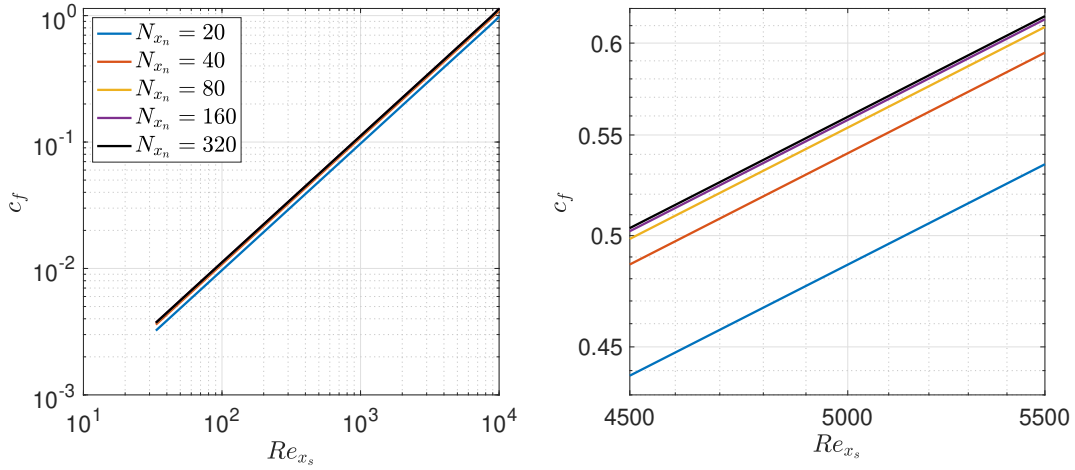

(a) Wall-resolved (WR).

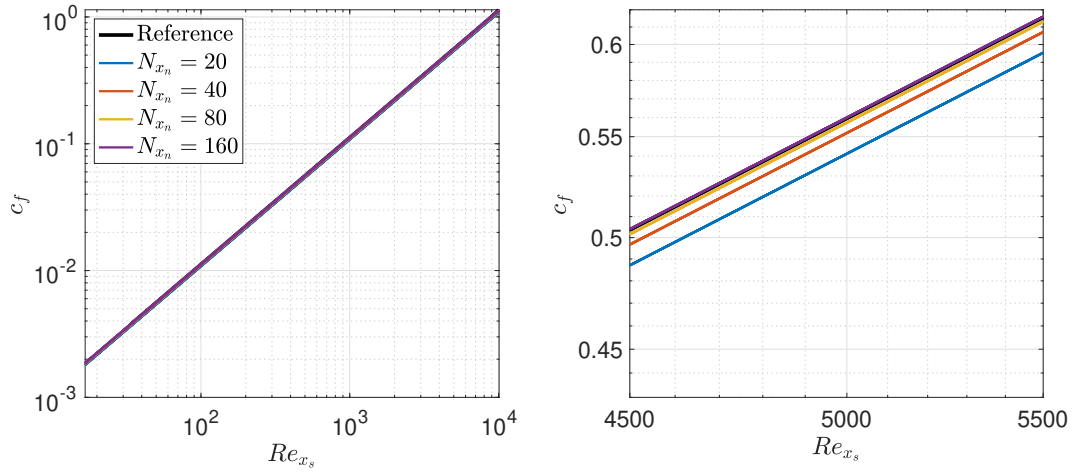

(b) Laminar wall model (LWM).

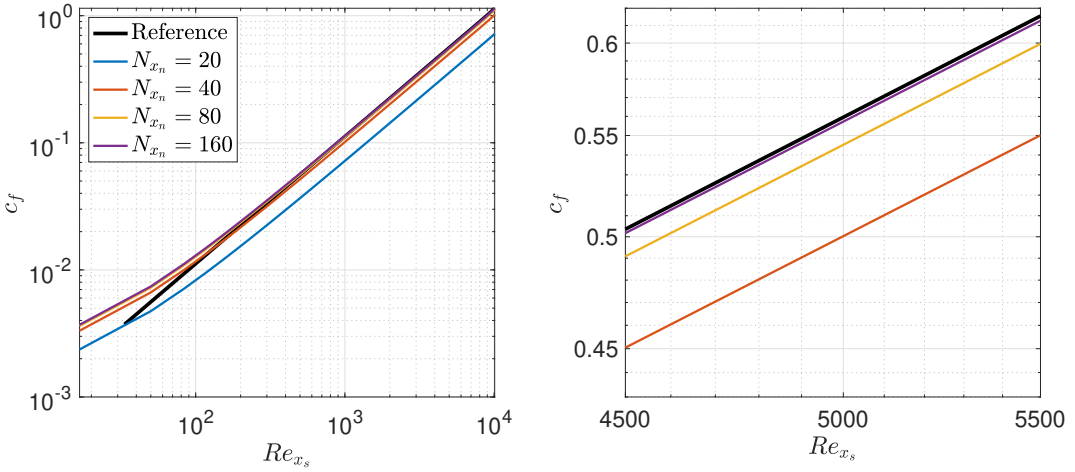

(c) Turbulent wall model (TWM).

Figure 4.10: Skin friction coefficient c_f for different grid resolutions in the wall-normal direction N_{x_n}. The reference friction (black line) corresponds in both cases to the WR solution with $N_{x_n} = 320$ and $N_{x_s} = 300$.

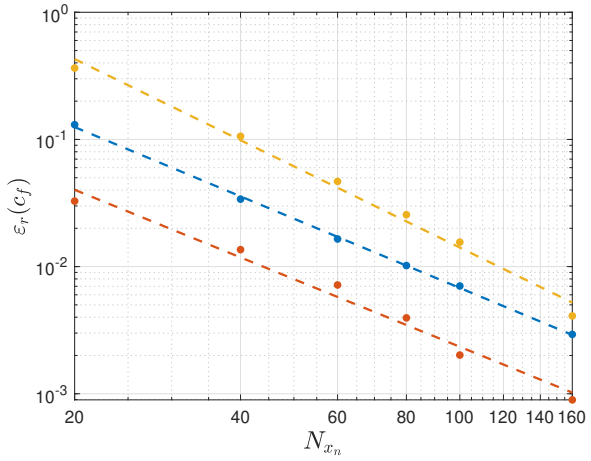

Figure 4.11: Relative error ε_r at the middle of the wall with respect to the WR reference solution ($N_{x_n} = 320$ and $N_{x_s} = 300$) on the wall-shear stress obtained from the WR solution (blue points), from the LWM (orange points) and from the TWM (yellow points).

4.2.2 Boundary Layer

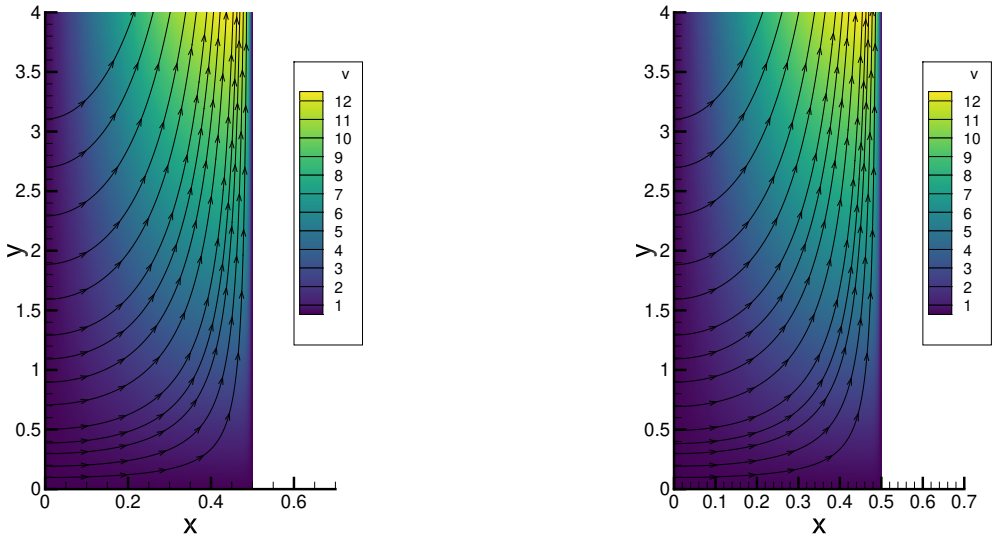

(a) WR ($N_{x_n} = 320$) .

(b) LWM ($N_{x_n} = 160$).

Figure 4.12: Steady wall-tangential velocity field.

At this stage, only the Neumann boundary condition has been validated. It is now necessary to verify if the wall modeling enables to obtain a solution similar to the WR reference case. As a qualitative comparison, the steady wall-tangential velocity field and the pressure field obtained with the LWM for $N_{x_n} = 160$ are both compared to the reference solution, respectively in Fig 4.12 and Fig 4.13. From this coarse analysis, it is possible to conclude that there is a good match between the two cases. Then, in order to go deeper in detail, the wall-tangential velocity distributions in $x_s/L_y = 0.375$, 0.5 and 0.625 from both methods are superimposed in Fig 4.14. It brings out that the LWM solution corresponds relatively well with the reference solution despite the lower resolution.

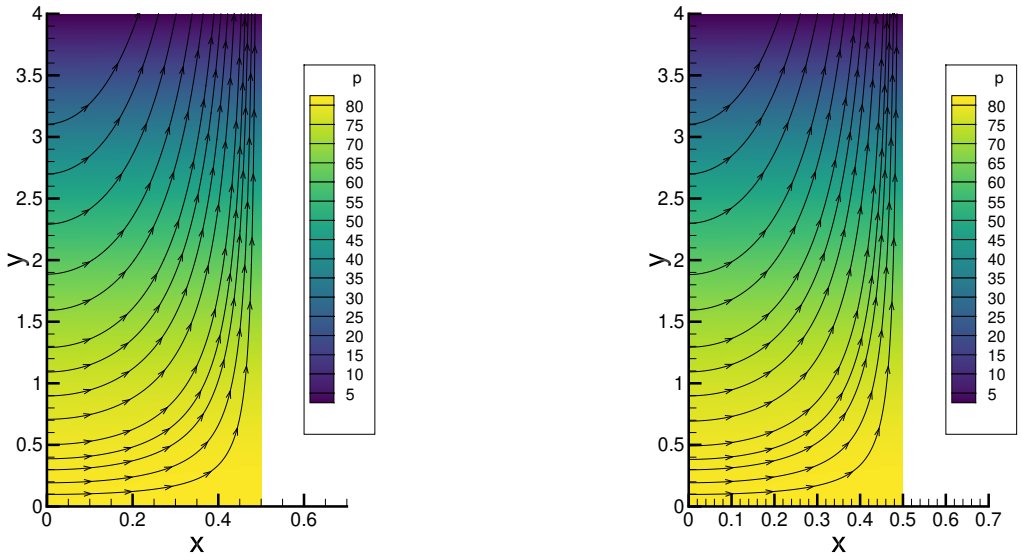

(a) WR ($N_{x_n} = 320$). **(b)** LWM ($N_{x_n} = 160$).

Figure 4.13: Steady pressure field.

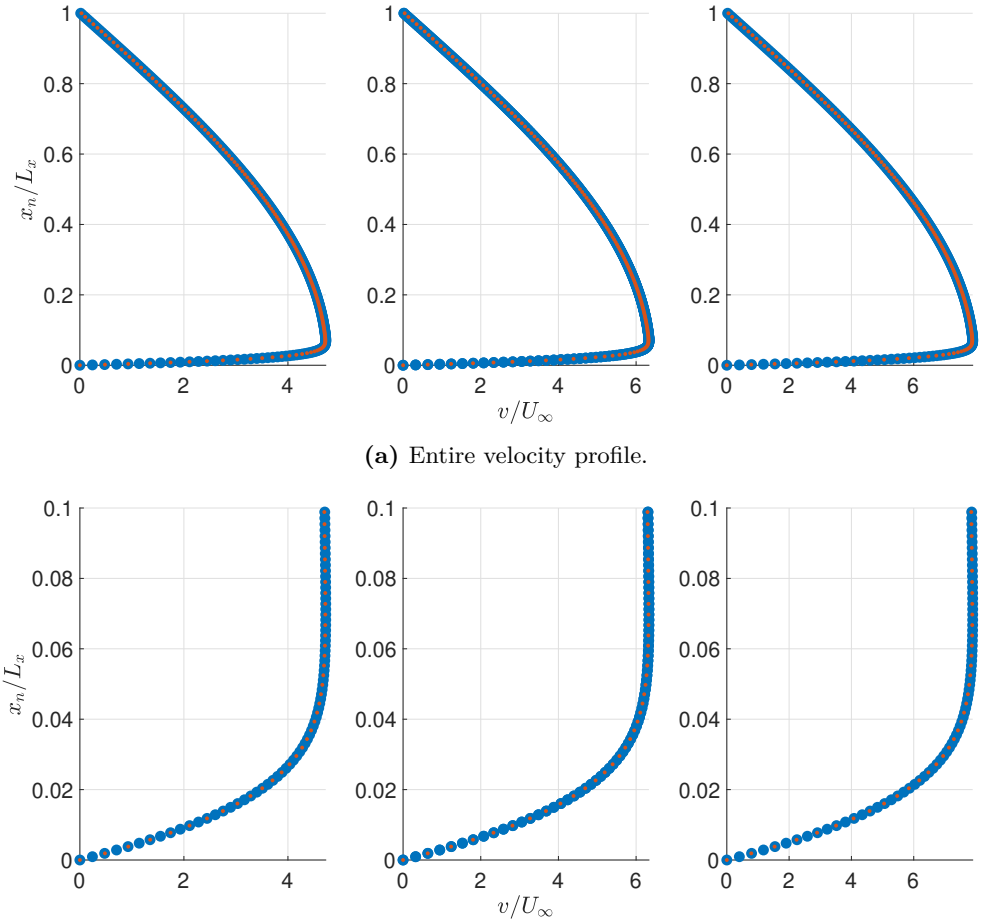

(a) Entire velocity profile.

(b) Zoom on the wall vicinity.

Figure 4.14: Wall-tangential velocity profile in $x_s/L_y = 0.375$, 0.5 and 0.625 (left to right) from the WR reference solution with $N_{x_n} = 320$ (blue points) and from the LWM solution with $N_{x_n} = 160$ (orange points).

4.2.3 Potential Flow Theory

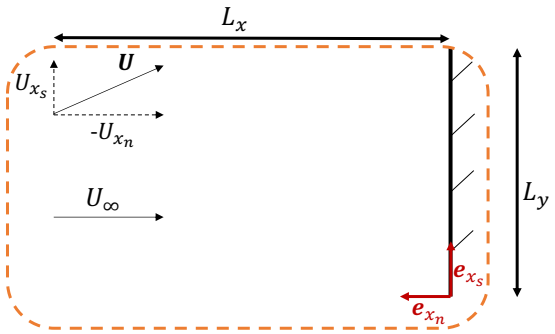

Figure 4.15: Illustration of the imposed inflow velocity U_∞ versus the velocity field $\mathbf{U}$ predicted from the potential flow theory.

It is important to specify that the incoming flow has been assumed so far as purely horizontal without any physical justification but only for the sake of simplicity. More rigorously, the inlet flow field can be approached from the potential flow theory [74], leading to a velocity field $\mathbf{U}$ represented in Fig 4.15 and expressed as

$$U_{x_n} = -K_p x_n \tag{4.2.3}$$

$$U_{x_s} = K_p x_s, \tag{4.2.4}$$

with K_p a constant. It is therefore obvious that the inlet boundary condition is physically inconsistent and introduces an error in the whole flow field. The error is all the greater if the half height L_y increases since the maximum value of the neglected component U_{x_s} is higher. Nevertheless, one can expect an attenuation of the related spurious effects at the wall vicinity by increasing the distance L_x.

To investigate the consequences on the LWM, one considers the computation of the inviscid speed constant K expressed in Eqn 4.2.1 and which only depends on the pressure field at the wall vicinity. A direct link with the potential flow theory can be made by considering the limit such that the ratio L_x/L_y tends to infinity. In this case, the effect from the inlet is negligible close to the wall and it is possible to use the potential flow Eqn 4.2.3 to express the asymptotic limit of K as

$$\lim_{L_x/L_y \to \infty} K = \frac{U_\infty}{L_x}. \tag{4.2.5}$$

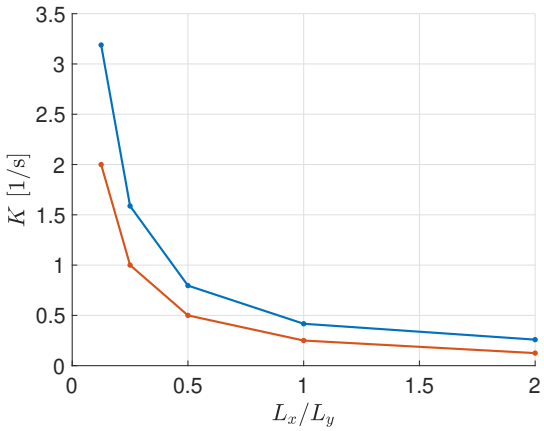

Figure 4.16: External flow velocity proportionality constant K from the LWM at the middle of the wall for different ratios L_x/L_y with $L_y = 4$ [m] (blue line). The results are put in contrast with the asymptotic limit from Eqn 4.2.5 (orange line).

To verify these words, the LWM is applied for different domain sizes by successively increasing L_x with L_y fixed at 4 [m]. For each case, the K value is extracted at the middle of the wall and the results are then summarized by the blue curve in Fig 4.16. Setting aside the asymptotic values from Eqn 4.2.5 (orange line), it is possible to deduce that the difference between both cases tends to decrease with an increasing ratio L_x/L_y, which means that the error coming from the inlet condition tends to fade away at the wall vicinity. Hence, this comparison with the potential flow theory enables to underline the importance of the boundary conditions and their impact on the physics of the flow, all the more important for small-sized domains. It is therefore necessary to keep a critical eye on the physical validity of the results previously discussed with the domain presenting a ratio $L_x/L_y = 0.5/4 = 0.125$.

4.3 Intermediate Conclusion

This section enables to validate the LWM for the stagnation point flow and for the self-similar region of the flat plate. Until a certain mesh resolution, the model enables to provide a more accurate wall-shear stress compared to the wall-resolved process. However, as shown with the analysis of the leading edge of the flat plate, it is essential to verify the validity of the self-similarity assumption throughout the domain for the local and global accuracy of the solution. In this case, using a linear approximation of the speed derivative near the leading edge and the Falkner-Skan friction on the rest of the domain leads to a much better match with the reference solution in terms of wall-shear stress, boundary layer thickness and velocity profile than imposing the Falkner-Skan estimate on the entire wall. Subsequently, the convergence study of the stagnation point flow underlines the robustness acquired by feeding the LWM with the pressure gradient instead of estimating the external flow speed directly from the velocity field. The sensitivity with respect to the height of extraction is much less important and it is therefore not necessary to determine the location of the boundary layer edge by trial and error. Such a validation prompts to extend this study by considering immersed boundaries.

Chapter 5

Surface Length Computation

Any surface can be straightforwardly represented by a triangular mesh in the form of a Standard Triangle Language (STL) file. This format is commonly used in practice and is relatively easy to obtain. The surface is described by a set of points gathered in triangles following the right-hand rule in a connectivity list [75]. Although it is an efficient way to describe complex shapes, it is not always trivial to compute the shortest distance on the resulting unstructured mesh with respect to a set of reference points. To overcome this, different methods have been developed using physical phenomena mainly based on wave propagation or heat diffusion. To illustrate the first category, Sethian established the Fast Marching algorithm [76, 77] which consists in solving the eikonal equation by simulating the propagation of a wave front from a set of source points. On the other side, Crane et al. proposed the Geodesics on Heat method [78] based on the relationship between the heat kernel and the surface length computation. In this work, a new approach is developed by adapting the reinitialization process described by Lauer in [59], which aims to compute the signed-distance function with respect to an interface defined on a Cartesian Mesh. Once operational, the method will be used to estimate the shortest distance on a surface defined by a triangular mesh with respect to a set of stagnation points, i.e. x_s involved in the wall-shear stress computation in Eqn 3.5.4. Hence, it will be possible to apply the LWM to immersed boundaries whose geometry is provided in the form of an STL file.

5.1 Original Reinitialization Process

The method proposed in this work is based on the reinitialization process explained by Lauer in [59]. This latter enables to reinitialize the signed-distance function ϕ with respect to an interface defined in a 3D Cartesian mesh. To do so, the reinitialization equation is applied as

$$\frac{\partial \phi}{\partial t_f} + S(\phi)(\|\nabla \phi\| - 1) = 0, \tag{5.1.1}$$

where t_f is a pseudo-time and $S(\phi)$ is the sign function with smearing expressed as

$$S(\phi) = \frac{\phi}{|\phi| + \Delta l} \quad \text{with} \quad \Delta l = \left|\frac{\partial \phi}{\partial x}\right| \Delta x + \left|\frac{\partial \phi}{\partial y}\right| \Delta y + \left|\frac{\partial \phi}{\partial z}\right| \Delta z. \tag{5.1.2}$$

The spatial derivatives are obtained following a modification of Godunov's method [79]. It is first possible to estimate the term $\partial\phi/\partial x$ by introducing two discretizations as

$$\left(\frac{\partial \phi}{\partial x}\right)^- = 2\frac{\phi_i - \phi_{i-1}}{\Delta x_i + \Delta x_{i-1}} \quad \text{and} \quad \left(\frac{\partial \phi}{\partial x}\right)^+ = 2\frac{\phi_{i+1} - \phi_i}{\Delta x_{i+1} + \Delta x_i}. \tag{5.1.3}$$

Then, it is necessary to choose one of these two terms as follows:

- If $S(\phi)\left(\frac{\partial \phi}{\partial x}\right)^+ \geq 0$ and $S(\phi)\left(\frac{\partial \phi}{\partial x}\right)^- \geq 0$: $\frac{\partial \phi}{\partial x} = \left(\frac{\partial \phi}{\partial x}\right)^-$.
- If $S(\phi)\left(\frac{\partial \phi}{\partial x}\right)^+ \leq 0$ and $S(\phi)\left(\frac{\partial \phi}{\partial x}\right)^- \leq 0$: $\frac{\partial \phi}{\partial x} = \left(\frac{\partial \phi}{\partial x}\right)^+$.

- If $S(\phi)\left(\frac{\partial\phi}{\partial x}\right)^{+} > 0$ and $S(\phi)\left(\frac{\partial\phi}{\partial x}\right)^{-} < 0$: $\frac{\partial\phi}{\partial x} = 0$.
- If $S(\phi)\left(\frac{\partial\phi}{\partial x}\right)^{+} < 0$ and $S(\phi)\left(\frac{\partial\phi}{\partial x}\right)^{-} > 0$: the variable s is introduced as

$$s = \frac{S(\phi)\left(\left|\left(\frac{\partial\phi}{\partial x}\right)^{+}\right| - \left|\left(\frac{\partial\phi}{\partial x}\right)^{-}\right|\right)}{\left(\frac{\partial\phi}{\partial x}\right)^{+} - \left(\frac{\partial\phi}{\partial x}\right)^{-} + \varepsilon},$$

  with ε being a small number based on computer accuracy.

  - If $s > 0$: $\frac{\partial\phi}{\partial x} = \left(\frac{\partial\phi}{\partial x}\right)^{-}$.
  - If $s < 0$: $\frac{\partial\phi}{\partial x} = \left(\frac{\partial\phi}{\partial x}\right)^{+}$.
  - If $s = 0$: $\frac{\partial\phi}{\partial x} = 0$.

Such a process is repeated in the other two directions of the space.

5.2 Adaptation of the Reinitialization Process

Now that the process to determine the signed-distance function ϕ with respect to an interface in a Cartesian mesh has been introduced, it is possible to adapt it to determine the shortest distance over a triangular mesh with respect to a set of stagnation points. This latter will be designated as the level-set function Φ in the following of this work and corresponds to the variable x_s involved in the wall-shear stress computation in Eqn 3.5.4. Subsequently, the set of stagnation points will be denoted by $\mathcal{V}_{SP}$ and the remaining vertices by $\mathcal{V}_r$ such that the whole set is expressed as $\mathcal{V} = \mathcal{V}_{SP} \cup \mathcal{V}_r$ and $\mathcal{V}_{SP} \cap \mathcal{V}_r = \varnothing$.

As a first step, the stagnation set is defined as

$$\Phi_v = 0 \qquad \forall v \in \mathcal{V}_{SP}, \tag{5.2.1}$$

and Eqn 5.1.1 is discretized in time using a first-order backward difference to obtain the following explicit expression

$$\Phi_v^{n+1} = \Phi_v^n + \Delta t \cdot (1 - \|\nabla\Phi_v^n\|) \qquad \forall v \in \mathcal{V}_r, \tag{5.2.2}$$

with n being the pseudo-time index, v the vertex index and Δt the pseudo-time step. Note that the sign function is, in this case, always 1 and thus not explicitly expressed.

Then, the pseudo-time step Δt is imposed as

$$\Delta t = C \cdot d_{\min}, \tag{5.2.3}$$

with $d_{\min}$ being the distance between the two closest vertices of $\mathcal{V}$ and C an arbitrarily imposed constant to ensure stability. In practice, the value $C = 1$ seems to be an interesting trade-off between stability and speed of convergence and will be the default value in the rest of this work. However, in case of divergence, it is simply advised to decrease C until getting a stable process. Besides, the convergence is monitored by the L^2 norm of the relative change in Φ, computed at the n^{th} iteration as

$$L^2[\Delta_r\Phi^n] = \sqrt{\sum_v \left[\frac{\Phi_v^n - \Phi_v^{n-1}}{\Phi_v^n}\right]^2} \qquad \forall v \in \mathcal{V}_r. \tag{5.2.4}$$

Regarding the gradient computation, it is now no longer possible to apply the method used by Lauer for a Cartesian mesh due to the irregularity of the points distribution. As alternatives, Mancinelli et al. introduced and compared three methods for calculating the gradient on triangular meshes [80]: the average gradient on star (AGS), the least squares fit of directional derivatives (LSDD) and the linear regression (LR). According to the authors, the LR offers the best performance on anisotropic meshes, but on the other hand, a very high computational cost, which makes it hardly applicable to large meshes. Subsequently, the comparison between the AGS and the LSDD brings out that the former is more accurate for almost all experiments and represents the best compromise between stability, accuracy and computational cost. It therefore seems relevant to select this method to estimate the gradient during the reinitialization.

The AGS consists in computing the gradient of the scalar field Φ at each triangle centroid and then applying a weighted average to obtain a gradient estimate at the vertices. Considering the triangle t defined by the vertices v_i, v_j and v_k and presenting an area A_t, the related gradient can be expressed as

$$\nabla\Phi_t = (\Phi_j - \Phi_i)\,\frac{(v_i - v_k)^{\perp}}{2A_t} + (\Phi_k - \Phi_i)\,\frac{(v_j - v_i)^{\perp}}{2A_t}, \tag{5.2.5}$$

where the symbol $\perp$ denotes the cross product with respect to the triangle normal, leading to an edge rotated by 90°. Afterwards, the gradient estimate at each vertex v is obtained by applying a weighted average of the related triangle gradients as

$$\nabla\Phi_v \simeq \frac{\sum_{t\in\mathcal{N}(v)} w_t \nabla\Phi_t}{\sum_{t\in\mathcal{N}(v)} w_t} \qquad \forall v \in \mathcal{V}_r, \tag{5.2.6}$$

with $\nabla\Phi_t$ computed from Eqn 5.2.5 and w_t corresponding to the weight assigned to the triangle t. $\mathcal{N}(v)$ stands for the set of triangles connected to the vertex v and verifying the upwind condition expressed as

$$\Phi_v > \Phi_{t,1} \qquad \text{and} \qquad \Phi_v > \Phi_{t,2}, \tag{5.2.7}$$

with $\Phi_{t,1}$ and $\Phi_{t,2}$ the respective values of the level-set function at the other two vertices of the considered triangle t. If this condition is not verified, the triangle is simply not taken into account in the averaging process. Note that if there is no valid triangle to obtain a gradient estimate, the gradient norm is simply imposed at zero as done by Lauer for the signed-distance function computation in Sec 5.1.

Regarding the weight w_t, several methods are applied in the literature. Correa et al. [81] investigated different possibilities as the inverse distance of the centroid of the triangle t with respect to the vertex v, the angle of t formed at v and the area/volume of t. In the same way, Sozer et al. [82] applied an inverse distance weighted (IDW) face interpolation by taking the square of the inverse distance of centroid as weight. Relying on different experiments [81, 83], both the inverse distance of centroid and the angle work similarly and lead to better performances than the area/volume. Subsequently, Correa et al. [81] concluded that the inverse distance enables to reach the highest accuracy as the mesh becomes highly irregular, while Mancinelli et al. [80] decided to keep the angle in order to obtain a better robustness against anisotropic meshes, i.e. meshes containing elongated elements. Due to this lack of uniqueness, both the inverse distance of centroid and the angle will be investigated in the following for the weighted average. For the former, the first and second powers of the distance will be studied.

Gathering the different steps leads to algorithm 3 with the initial value Φ^0 imposed by default at 10^{-6}. Note that for the rest of this chapter, the system of units will not be prescribed since the unit of Φ_v corresponds to the unit of the vertices coordinates. All the values are thus expressed in the same system of units imposed by the geometry definition.

Algorithm 3 Reinitialization.

Initialization:

$$\Phi_v^0 = \Phi^0 \qquad \forall v \in \mathcal{V}_r;$$

$$\Phi_v = 0 \qquad \forall v \in \mathcal{V}_{SP};$$

Pseudo time step computation with Eqn 5.2.3;

$n \leftarrow 0$;

do

Gradient $\nabla\Phi_t^n$ computation for each triangle t with Eqn 5.2.5;

forall $v \in \mathcal{V}_r$ **do**

Gradient $\nabla\Phi_v^n$ computation by averaging the gradients of the valid triangles with Eqn 5.2.6;

Updated level-set function Φ_v^{n+1} computation with Eqn 5.2.2;

end

$L^2\left[\Delta_r\Phi^{n+1}\right]$ computation with Eqn 5.2.4;

$n \leftarrow n + 1$.

while $L^2\left[\Delta_r\Phi^n\right] > \varepsilon$;

As a first validation, one considers the level-set function over a flat plate defined in the xy-plane with $L_x = 2$ and $L_y = 1$ and for which the stagnation line is imposed in $x = 0$. For this simple case, the reference solution is $\Phi_{ref}(x, y) = x$ and the surface is represented by a triangular mesh made of 1756 homogeneously distributed vertices. Regarding the averaging method in Eqn 5.2.6, the used weighting method is that considering the inverse distance of centroid.

First and foremost, it is necessary to focus on the convergence of the iterative process. To do so, the mean relative error $\bar{\varepsilon}_r[\Phi]$ and the L^2 norm of the relative change in Φ are respectively represented in Fig 5.1a and 5.1b. It brings out that the process seems almost perfectly converged around 190 iterations at which both variables are close to the epsilon machine such that

$$\bar{\varepsilon}_r[\Phi] = 3.0 \cdot 10^{-16} \qquad \text{and} \qquad L^2[\Delta_r\Phi] = 2.8 \cdot 10^{-15}.$$

The solution at the 250^{th} iteration is then represented in Fig 5.1c and 5.1d in both 2D and 3D views. The 3D view enables to demonstrate the smoothness of the level-set function distribution as well as to validate the process for this first setup.

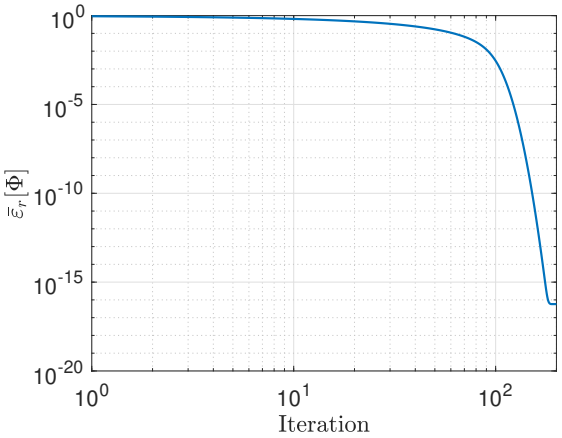

(a) Mean relative error $\bar{\varepsilon}_r$ on Φ with respect to the reference solution $\Phi_{ref} = x$.

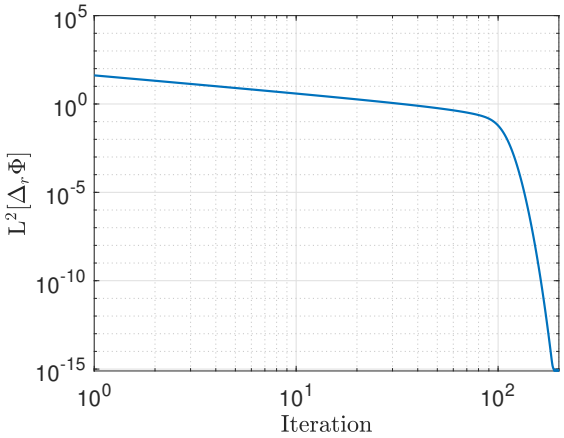

(b) L^2 norm of the relative change in Φ expressed in Eqn 5.2.4.

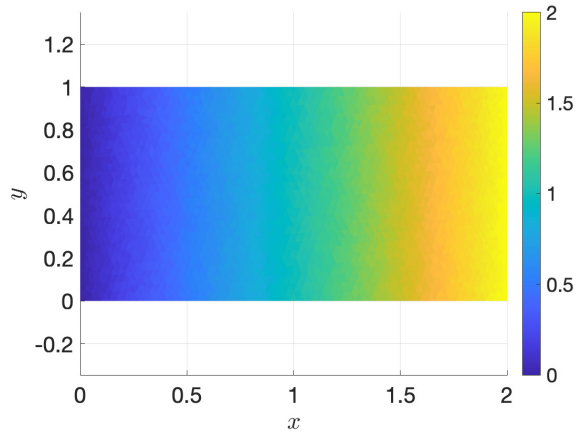

(c) Steady Φ field in 2D view.

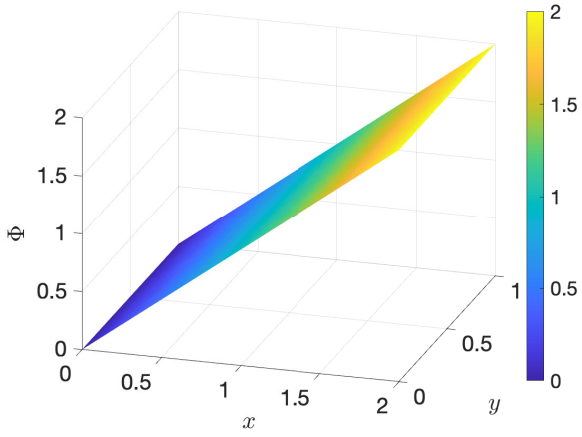

(d) Steady Φ field in 3D view.

Figure 5.1: Reinitialization process 3 applied to a flat plate defined in the xy-plane with a stagnation line imposed in $x = 0$.

5.3 Presence of Maxima and Ridges

It is important to underline that the reinitialization Eqn 5.2.2 assumes an exact solution with a gradient norm which is unit everywhere. Yet, this is not the case if the level-set function comprises local maxima or ridges. To illustrate these words, one can consider the exact solution of a sphere presenting a single stagnation point. In this case, the point on the surface opposite to the stagnation location is a maximum and presents a zero gradient norm. Thus, the reinitialization process 3, as it is, cannot converge towards the correct solution at maxima, but in practice leads to discontinuities. Note that since the process is an upwind scheme, such discontinuities do not impact the rest of the solution.

Considering the LWM in real applications, it is generally unlikely to apply it at such points. Returning to the example of the sphere, the maximum is located in the separation region where it is irrelevant to apply the LWM. Nevertheless, in order to be as robust and general as possible, algorithm 3 is improved to avoid these discontinuities. The reinitialization process is first modified such that if a maximum is detected, i.e. if all level-set function values on the first ring $\mathcal{V}_{\text{ring},v}$ of a given vertex v are smaller than Φ_v, the gradient norm $\|\nabla\Phi_v\|$ is imposed at 1. Thus, the iterative process is locally stopped and Φ_v remains constant. Then, once the iterative process has converged, a post-processing is applied at each maximum. To do so, the reinitialization process is applied at the vertex v considering each connected triangle t and the corresponding gradient separately, which leads to an estimate $\Phi_{v,t}$. Since only a part of the surrounding is considered at

the time, the maximum does not correspond to a top of a bump anymore and assuming a unit gradient norm leads to more accurate results for each triangle. Finally, in order to obtain a single value in v, a weighted average is applied in the same way as done for the gradient averaging in Eqn 5.2.6 such as

$$\Phi_v \simeq \frac{\sum_{t\in\mathcal{N}(v)} w_t \Phi_{v,t}}{\sum_{t\in\mathcal{N}(v)} w_t}. \tag{5.3.1}$$

This process is repeated until $L^2\left[\Delta_r \Phi\right]$ becomes weaker than a certain tolerance. If the level-set function only presents a single maximum, the process can be achieved in a single iteration since the neighboring vertices remain unchanged during the post-processing. However, if the distance field presents a ridge, the post-processed points depend on each other and it is therefore necessary to apply the process several times until reaching the converged solution. The improved process can thereby be recapitulated as algorithm 4 and the tolerance ε will be imposed at 10^{-12} in the following.

In order to illustrate the limitations of algorithm 3 and the improvements brought by algorithm 4, one considers the same flat plate as defined in Sec 5.2. In addition, in order to obtain a reference solution presenting a ridge, two stagnation lines are respectively imposed in $x = 0$ and $x = 2$. For such a configuration, the reference solution is expressed as

$$\Phi_{ref}(x, y) = \begin{cases} x & 0 \leq x \leq 1, \\ 2 - x & 1 \leq x \leq 2, \end{cases} \tag{5.3.2}$$

and thus presents a crest in $x = 1$. Algorithm 3 is finally applied by considering the inverse distance of centroid method during the averaging process.

The resulting level-set function and relative error after 800 iterations are respectively represented in Fig 5.2a and 5.2b. This enables to highlight the existence of discontinuities on the ridge leading to a maximum relative error of approximately 1400 %. As previously mentioned, it is possible to notice from the relative error distribution that the rest of the solution is not impacted by the discontinuities due to the upwind nature of the scheme. As an order of magnitude, the relative error drops around 10^{-16} at the discontinuities proximity and remains relatively constant over the rest of the domain.

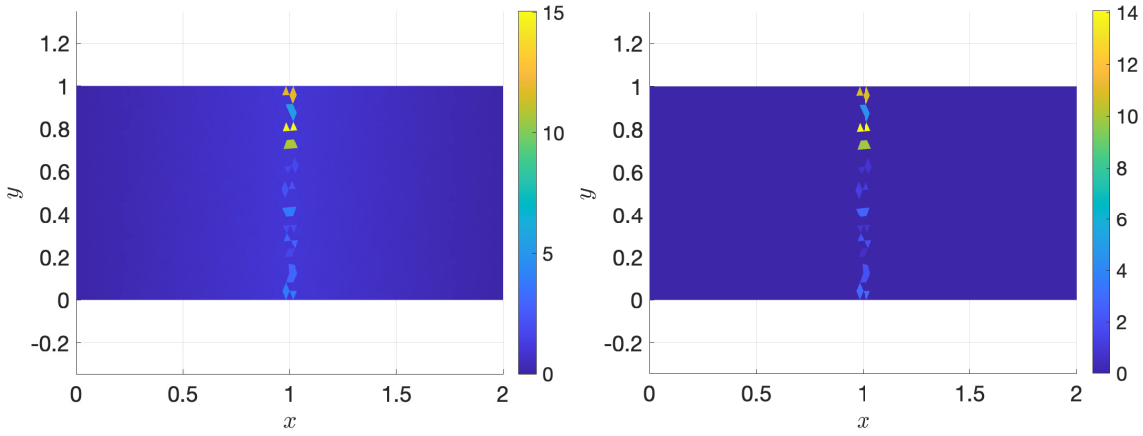

(a) Steady Φ field in 2D view.

(b) Relative error distribution on the steady Φ field with respect to the reference solution in Eqn 5.3.2.

Figure 5.2: Reinitialization process 3 applied to a flat plate defined in the xy-plane with two stagnation lines respectively imposed in $x = 0$ and $x = 2$.

Algorithm 4 Improved reinitialization.

Initialization: $\Phi_v^0 = \Phi^0 \quad \forall v \in \mathcal{V}_r \qquad \text{and} \qquad \Phi_v = 0 \quad \forall v \in \mathcal{V}_{SP}$;

Pseudo time step computation with Eqn 5.2.3;

`/* Main loop */`

$n \leftarrow 0$;

do

  Gradient $\nabla\Phi_t^n$ computation for each triangle t with Eqn 5.2.5;

  forall $v \in \mathcal{V}_r$ **do**

    if $\Phi_v^n > \Phi_w^n \quad \forall w \in \mathcal{V}_{ring,v}$ **then**

      $\|\nabla\Phi_v^n\| = 1$;

    else

      Gradient $\nabla\Phi_v^n$ computation by averaging the gradients of the valid triangles with Eqn 5.2.6;

    end

    Updated level-set function Φ_v^{n+1} computation with Eqn 5.2.2;

  end

  $L^2\left[\Delta_r\Phi^{n+1}\right]$ computation with Eqn 5.2.4;

  $n \leftarrow n + 1$;

while $L^2\left[\Delta_r\Phi^n\right] > \varepsilon$;

`/* Post-processing */`

do

  Determine the set of maximums $\mathcal{V}_{\max}$ such that $\Phi_v^n > \Phi_w^n \quad \forall w \in \mathcal{V}_{\text{ring},v}$;

  forall $v \in \mathcal{V}_{\max}$ **do**

    forall $t \in \mathcal{N}(v)$ **do**

      $\Psi^0 \leftarrow \Phi^n$;

      $j \leftarrow 0$;

      do

        Gradient $\nabla\Psi_t^j$ computation for the triangle t with Eqn 5.2.5 considering Ψ_v^j;

        Updated level-set function $\Psi_{v,t}^{j+1}$ computation with Eqn 5.2.2 only considering the triangle t and its gradient $\nabla\Psi_t^j$;

        $\Psi^{j+1} \leftarrow \Psi^j$ and $\Psi_v^{j+1} \leftarrow \Psi_{v,t}^{j+1}$;

        $j \leftarrow j + 1$;

      while $\left|\left\|\nabla\Psi_t^{j-1}\right\| - 1\right| > \varepsilon$;

      $\Phi_{v,t}^{n+1} \leftarrow \Psi_{v,t}^j$;

    end

    Φ_v^{n+1} computation with Eqn 5.3.1 from $\Phi_{v,t}^{n+1} \quad \forall t \in \mathcal{N}(v)$;

  end

  $L^2\left[\Delta_r\Phi^{n+1}\right]$ computation with Eqn 5.2.4;

  $n \leftarrow n + 1$;

while $L^2\left[\Delta_r\Phi^n\right] > \varepsilon$;

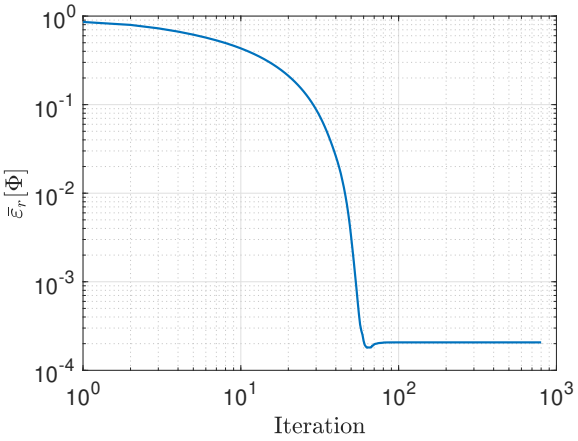

(a) Mean relative error $\bar{\varepsilon}_r$ on Φ with respect to the reference solution in Eqn 5.3.2 through the main loop.

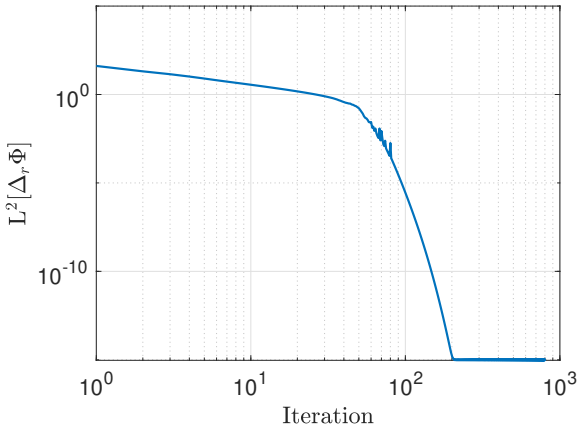

(b) L^2 norm of the relative change in Φ expressed in Eqn 5.2.4 through main loop.

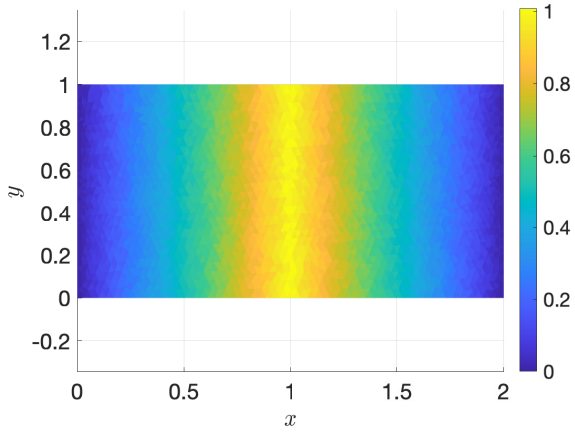

(c) Final Φ field in 2D view.

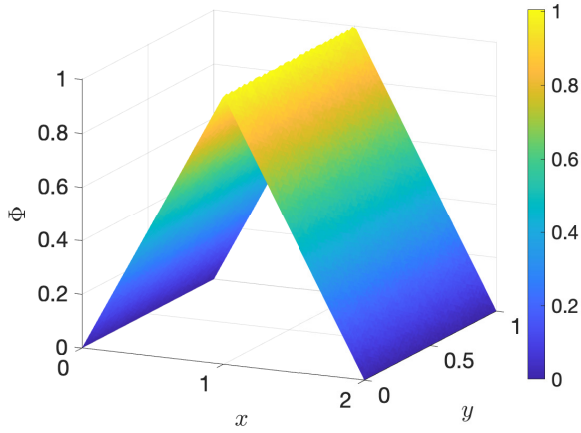

(d) Final Φ field in 3D view.

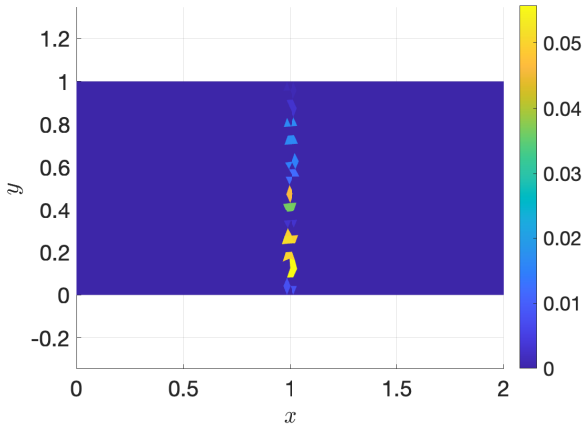

(e) Relative error distribution on the final Φ field with respect to the reference solution in Eqn 5.3.2.

Figure 5.3: Improved reinitialization process 4 applied to a flat plate defined in the xy-plane with two stagnation lines respectively imposed in $x = 0$ and $x = 2$. The final Φ field is obtained after 800 iterations in the main loop and considering $\varepsilon = 10^{-12}$ during the post-processing part.

Afterwards, the improved process 4 is applied considering the same setup and the same averaging method. The focus is first on the convergence of the main loop. To that end, the mean relative error and the L^2 norm

of the relative change in Φ are each represented in Fig 5.3a and 5.3b. Relying on the minimum value of $L^2[\Delta_r\Phi]$, one can conclude that the convergence is reached after about 250 iterations leading to

$$\bar{\varepsilon}_r[\Phi] = 1.0 \cdot 10^{-4} \qquad \text{and} \qquad L^2[\Delta_r\Phi] = 9.7 \cdot 10^{-16}.$$

It is important to keep in mind that at this stage, the points on the ridge are still untreated and are only frozen by imposing a unit gradient norm. Then, the post-processing is applied with a tolerance $\varepsilon = 10^{-12}$, which leads to the solution represented in Fig 5.3c and 5.3d with a mean relative error

$$\bar{\varepsilon}_r[\Phi] = 7.3 \cdot 10^{-5}.$$

It brings out the smoothness of the solution and the absence of the discontinuities previously observed with algorithm 3. The corresponding relative error distribution in Fig 5.3e reveals that the accuracy remains, however, weaker on the ridge compared to the rest of the solution. It is therefore important to keep such a critical region in mind if a high accuracy is required in the whole domain.

5.4 Convergence Study

So far, the improved reinitialization process 4 has been illustrated for a flat plate with a given mesh resolution. It seems relevant to go further by studying the convergence of the obtained level-set function with respect to the number of vertices and this, for the three types of averaging methods. In the following, the method using the inverse distance of centroid is denoted by $1/d$, the one considering the square of the inverse distance of centroid by $1/d^2$ and the one utilizing the related angle by θ. Subsequently, in addition to the flat plate, the following geometries are considered: a cylinder, a sphere and a cube. To that end, the different shapes are meshed by the open source 3D finite element mesh generator, so-called *Gmsh* [84].

As a general procedure, the mean relative error $\bar{\varepsilon}_r[\Phi]$ on the level-set function field and the relative error $\varepsilon_r[\Phi_{\max}]$ on the absolute maximum are represented for the different considered mesh resolutions and types of averaging. The solution related to the weakest mean relative error is then illustrated. For each case, the convergence in the main loop is monitored by verifying that the plateau of $L^2[\Delta_r\Phi]$ is reached and the post-processing is achieved with $\varepsilon = 10^{-12}$.

5.4.1 Flat Plate

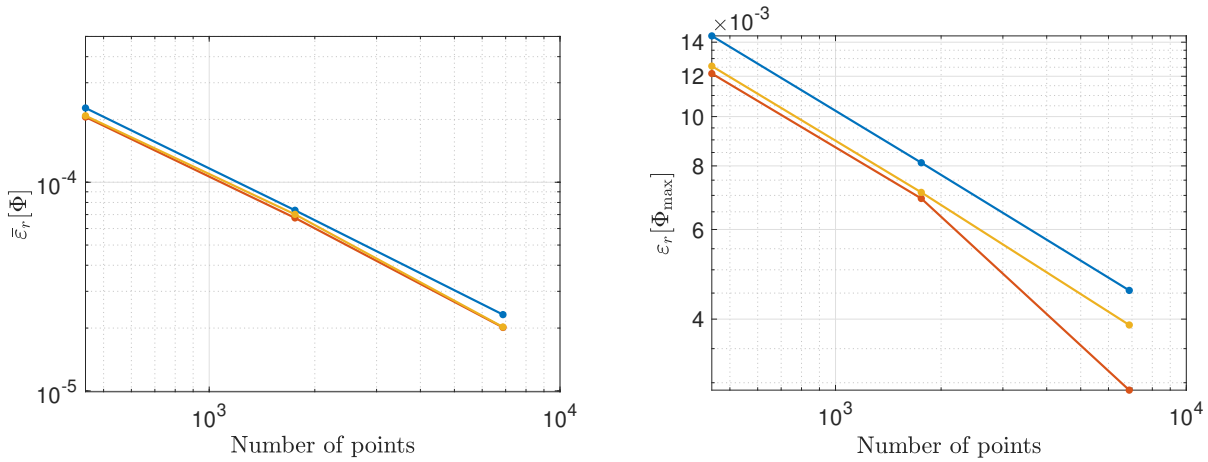

(a) Mean relative error $\bar{\varepsilon}_r$ on the final Φ field with respect to the reference solution in Eqn 5.3.2.

(b) Relative error ε_r on the absolute maximum $\Phi_{\max}$ of the final Φ field.

Figure 5.4: Improved reinitialization process 4 applied to the flat plate with two stagnation lines, cfr. Fig 5.3, and using the weighted average $1/d$ (blue line), $1/d^2$ (orange line) and θ (yellow line).

First, the flat plate with two stagnation lines, as previously described in Sec 5.3, is considered. The mean relative error in Fig 5.4a reveals that the three weights lead to the same order of convergence around 0.85.

The mean accuracy is similar in the three cases, although slightly weaker with $1/d$. An analogous behavior is observed from $\varepsilon_r[\Phi_{\max}]$ in Fig 5.4b, except at the highest resolution where $1/d^2$ enables a steeper decrease of the relative error.

5.4.2 Cylinder

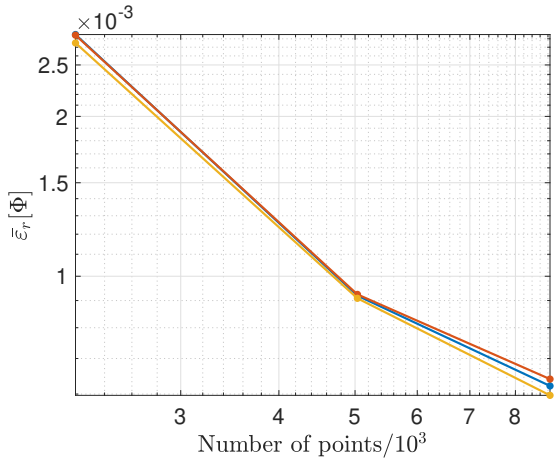

(a) Mean relative error $\bar{\varepsilon}_r$ on the final Φ field with respect to the reference solution in Eqn 5.4.1.

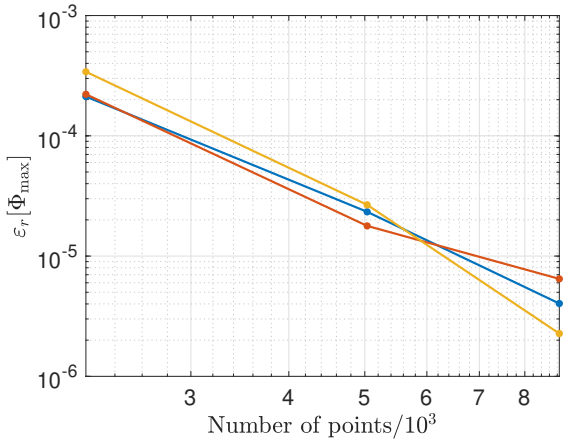

(b) Relative error ε_r on the absolute maximum $\Phi_{\max}$ of the final Φ field.

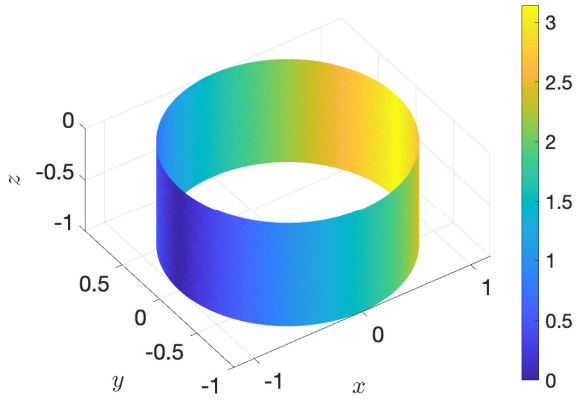

(c) Final Φ field with the geometry in 3D.

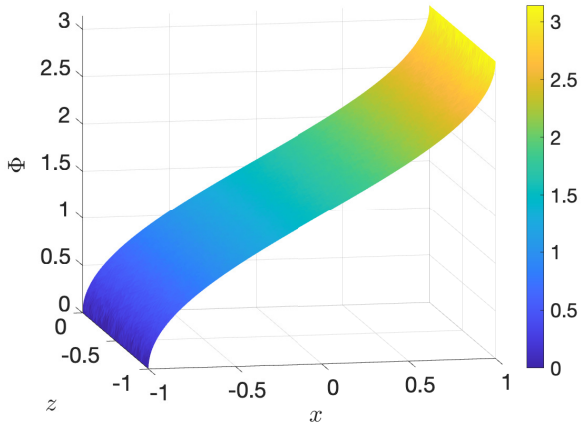

(d) Final Φ field with the geometry projected in a xz-plane $\forall y \geq 0$.

Figure 5.5: Improved reinitialization process 4 applied to a cylinder centered in $(x,\ y) = \mathbf{0}$ and with a stagnation line imposed in $(x,\ y) = (-1,\ 0)$ with $z \in [-1; 0]$. The improved reinitialization process 4 is carried out using the weighted average $1/d$ (blue line), $1/d^2$ (orange line) and θ (yellow line). The final Φ field presented is the solution corresponding to the finest mesh made of 8853 points and using the weighted average θ.

The focus is now on a cylinder of unit radius, centered in $(x, y) = \mathbf{0}$ and with $z \in [-1; 0]$. Imposing a stagnation line in $(x,\ y) = (-1,\ 0)$ leads to the reference solution

$$\Phi_{ref}(x, y) = \arccos\left(-x/\sqrt{x^2 + y^2}\right). \tag{5.4.1}$$

The related mean relative error in Fig 5.5a enables to deduce that the order of convergence is about 1.1 for the three weights, each of them leading more or less to the same accuracy in the mean sense. Regarding the relative error on $\Phi_{\max}$ in Fig 5.5b, the post-processing converges towards the reference solution for all three

types of weights. However, none of them stands out in terms of accuracy over the entire range of resolutions.

Finally, the solution at the highest resolution, i.e. with the mesh made of 8853 points and using the weight θ, is represented in Fig 5.5c. In this case, the relative errors are

$$\bar{\varepsilon}_r[\Phi] = 6.0 \cdot 10^{-4} \qquad \text{and} \qquad \varepsilon_r\left[\Phi_{\max}\right] = 2.3 \cdot 10^{-6}.$$

In order to assess the smoothness of this solution, the geometry is projected in the xz-plane $\forall y \geq 0$ and the level-set function is represented in the normal direction, which gives Fig 5.5d. This illustration demonstrates the smoothness of the solution for the current curved geometry.

5.4.3 Sphere

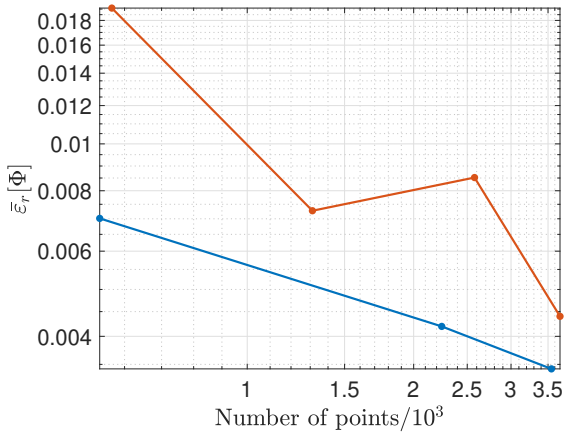

(a) Mean relative error $\bar{\varepsilon}_r$ on the final Φ field with respect to the reference solution in Eqn 5.4.2.

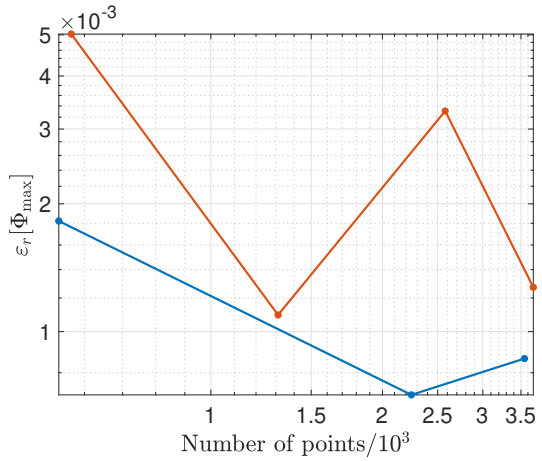

(b) Relative error ε_r on the absolute maximum $\Phi_{\max}$ of the final Φ field.

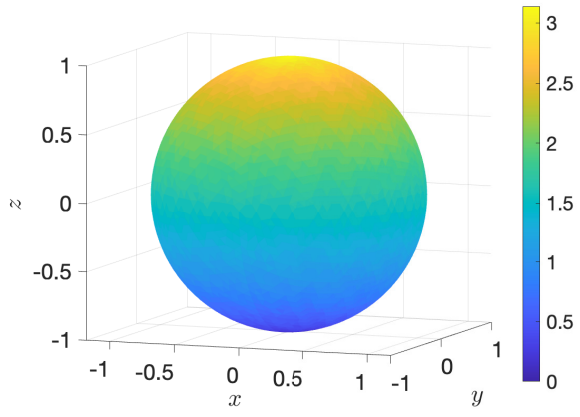

(c) Final Φ field with the geometry in 3D.

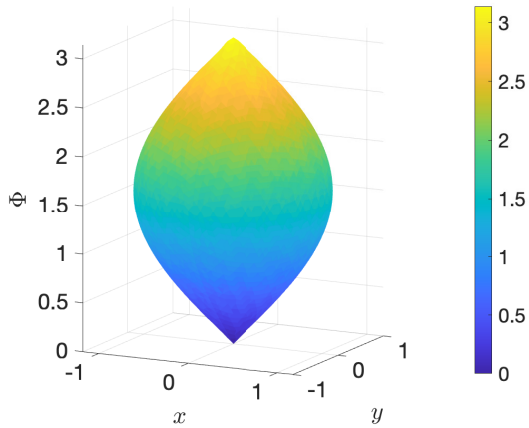

(d) Final Φ field with the geometry projected in a xy-plane.

Figure 5.6: Improved reinitialization process 4 applied to a sphere centered in $(x, y, z) = \mathbf{0}$ and with a stagnation point imposed in $(x, y, z) = (0, 0, -1)$. The two geometric definitions in Fig 5.7 are considered: half-circle definition (orange line) and triple-circle definition (blue line). The final Φ field presented is the solution corresponding to the finest mesh made of 3550 points with the triple-circle geometry definition.

(a) Half-circle definition. **(b)** Triple-circle definition.

Figure 5.7: Geometric definition of the sphere surface during the meshing process. The constraints imposing the number of elements are only imposed on the solid black curves.

In order to increase the complexity, the process is applied to a sphere of unit radius, centered in $(x, y, z) = \mathbf{0}$ and with a single stagnation point located in $(x, y, z) = (0, 0, -1)$. The reference solution is thus expressed as

$$\Phi_{ref}(x, y, z) = \arccos\left(-z/\sqrt{x^2 + y^2 + z^2}\right). \tag{5.4.2}$$

As illustrated in Fig 5.7, two geometry definitions are employed during the mesh generation: a half circle and a combination of three circles. In both cases, the solid black curves are used to impose the number of elements during the refinement and to guide the automatic meshing carried out by *Gmsh*. The geometry in Fig 5.7a therefore leads to more mesh irregularities compared to the one in Fig 5.7b. Finally, for the sake of simplicity, the re-initialization process is applied to these two cases only with the averaging method θ.

The convergence studies of the relative errors $\bar{\varepsilon}_r[\Phi]$ and $\varepsilon_r[\Phi_{\max}]$, respectively in Fig 5.6a and 5.6b, reveal that the geometric definition and the resulting mesh quality play a significant role. Indeed, the triple-circle geometry enables to obtain a monotonic decrease of the mean error along with the better accuracy over the whole resolution range in the mean sense and regarding the absolute maximum $\Phi_{\max}$. In contrast, the half-circle geometry presents a weaker precision and a slight increase of the mean relative error during the refinement process. It would be relevant to carry out further investigations with a rigorous analysis of the mesh properties (such as the number of obtuse angles, triangle elongation...) in order to explain the evolution of the error with respect to such parameters. Additionally, a very slight increase of $\varepsilon_r[\Phi_{\max}]$ is observed for the triple-circle case despite a monotonic decrease of the mean error, which brings to light a certain lack of robustness from the post-processing. Once again, a study of the mesh quality would be interesting to get a better understanding of such a trend. Despite this lack of monotonicity, it is important to keep in mind that the mean relative error remains of the order of $10^{-2} - 10^{-3}$ and the relative error on the absolute maximum around 10^{-3} for all cases. Such orders of magnitude seem relatively acceptable in the wall modeling field which is already tainted by imprecision due to the physical assumptions.

Lastly, the solution obtained with the finest mesh and with the triple-circle geometry is represented in Fig 5.6c. Its smoothness is highlighted by projecting the geometry in a xy-plane and presenting the level-set function along the normal direction in 5.6d.

5.4.4 Cube

Finally, the reinitialization process is applied to a cube of unit edge length $c = 1$ presenting a stagnation point at one of its vertices in $(x, y, z) = \mathbf{0}$. For such a configuration, the shortest path to reach the point presenting the absolute maximum level set function value $\Phi_{\max}$ is shown in Fig 5.8. This enables to compute the reference value

$$\Phi_{\max,\text{ref}} = 2 \cdot \sqrt{c^2 + (c/2)^2}.$$

The geometry is defined by a triangular mesh made of $16.9 \cdot 10^3$ vertices and the considered averaging method is θ.

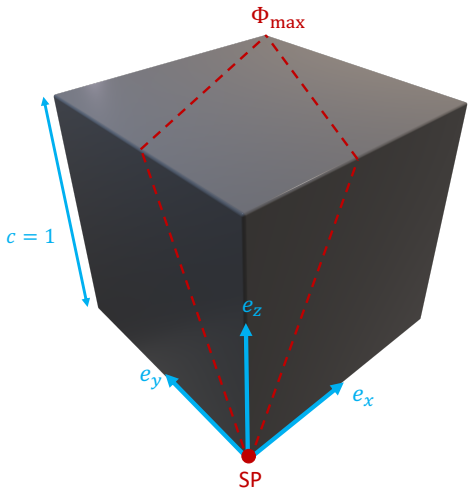

Figure 5.8: Cube of unit edge length c presenting a stagnation point (SP) in $(x, y, z) = \mathbf{0}$ and shortest paths from the SP to the absolute maximum Φ_{max} (dashed line, red).

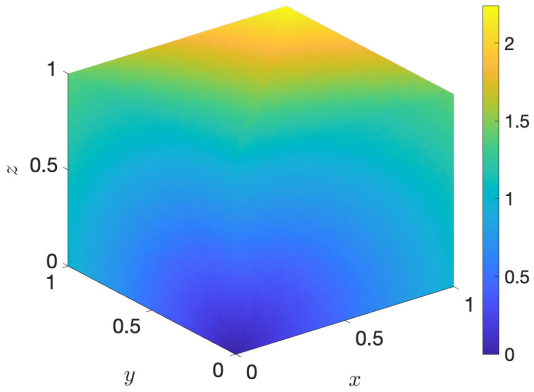

(a) Final Φ field with the geometry in 3D.

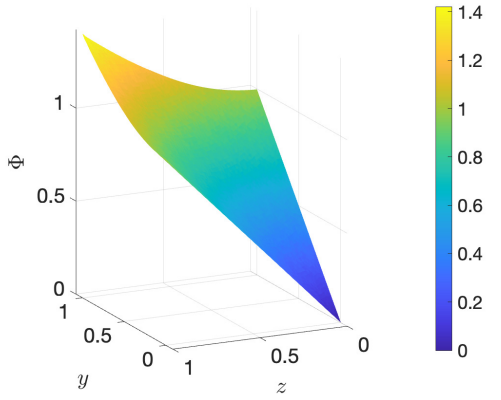

(b) Φ field over the face in $x = 0$.

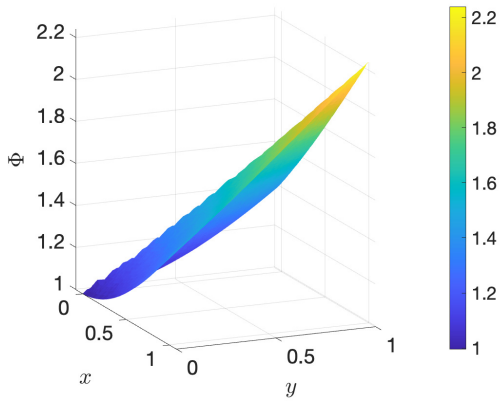

(c) Φ field over the face in $z = 1$.

Figure 5.9: Improved reinitialization process 4 applied to a cube presenting a stagnation point imposed in $(x, y, z) = \mathbf{0}$.

The resulting level-set function is shown in Fig 5.9. The accuracy of the solution is first assessed in $\Phi_{\max}$ by computing the relative error

$$\varepsilon_r \left[\Phi_{\max}\right] = 7.9 \cdot 10^{-4}.$$

As a global observation, the level-set function field in Fig 5.9a is relatively smooth even at the edges of the cube. Thus, the reinitialization process and, more specifically, the method which computes the gradient offers a good robustness with respect to abrupt changes in surface direction.

In addition, the three faces in $x = 0$, $y = 0$ and $z = 0$ do not present any ridge and show an excellent smoothness, as highlighted in Fig 5.9b with the surface in $x = 0$. The other three require the post-processing to treat their respective ridge located on the diagonal connected to the point $\Phi_{\max}$. As shown in Fig 5.9c for the face in $z = 1$, the distance field is globally smooth despite some irregularities on the ridge line where the post-processing is applied. Nevertheless, the improved reinitialization enables to obtain a field without any discontinuity and with a globally good smoothness.

5.5 Intermediate Conclusion

The improved reinitialization process 4 seems relatively robust for both flat plate and cylinder. For these setups, the algorithm monotonically convergences towards the reference solution with a decrease of the mean error of the first order. Subsequently, it comes that the type of weight does not significantly influence the accuracy of the solution and this, for all mesh resolutions. On the other side, the analysis of the sphere highlights the sensitivity of the method with respect to the mesh quality. In the case of an irregular mesh, it is possible to obtain a weak increase of the mean relative error during the refinement process. It would be interesting to complete this analysis with a deeper investigation of the mesh properties. Finally, the study of the cube brings out the robustness of the process with respect to the steep changes in surface direction encountered at each edge of the geometry.

Regarding the LWM, the improved reinitialization process seems promising due to the smoothness of the solutions and their level of accuracy. It is clear that, for the simple geometries considered, the precision of the obtained level-set function is not as perfect as the analytical solution, but it is important to keep in mind the imprecision introduced by the modeling itself. Indeed, the overall accuracy is inevitably limited by the self-similarity assumption. Hence, in this context, the order of magnitude of the error for the different studied configurations seems acceptable. Finally, algorithm 4 can be easily parallelized, which gives the opportunity to reach interesting performances and apply the process to complex bodies requiring a large number of vertices and without a known analytical solution.

Chapter 6

Transitional Flow over an Extruded Wing

Thanks to algorithm 4, it is now possible to apply the LWM to immersed boundaries and explore more complex setups. In this section, the transitional flow over an extruded wing is investigated. The physics at the wall is modeled by a hybrid model combining the LWM with a turbulent wall model based on the general wall function (GWF) proposed by Shih et al. [85] and simplified by assuming a zero pressure gradient. Regarding the test cases, a NACA0012 is first considered at $Re = 1.25 \cdot 10^6$ with a zero angle of attack. Then, the A-airfoil is studied at ($Re = 3.1 \cdot 10^6$; AoA $= 3.4°$) and ($Re = 2.1 \cdot 10^6$; AoA $= 13.3°$).

6.1 Methodology

The emphasis is first on the hybrid wall model (HWM) composed of the LWM and a turbulent wall model based on a simplified version of the general wall function (GWF) [85] neglecting the effect of the pressure gradient. The LWM gives a wall-shear stress estimate as described in Sec 3.5.3 from the pressure field extracted in $x_n = h_{w,p}$. To do so, it is first necessary to determine the stagnation points from the literature and then apply algorithm 4 to obtain the level-set function field of the STL file defining the geometry. Afterwards, this field is used to determine the level-set function at the immersed boundary centroid in each cut cell by applying a linear interpolation. It is then possible to compute and provide a laminar wall-shear stress estimate at each of these control points.

On the other side, according to Shih et al. [85], the general wall function is said to be unified, which means that it covers the whole inner layer and is therefore applicable in the viscous sublayer, buffer layer and inertial sublayer. More specifically, an asymptotic solution is obtained for both inertial and viscous sub-layers. Then, an analytical expression matching with both asymptotic solutions is established in the buffer layer by introducing a turbulent stress model. The general wall function, as formulated in [85], is fed with the tangential speed and pressure gradient. However, the implementation used in INCA does not take into account the pressure gradient by setting this latter to zero and only considers the tangential speed in $x_n = h_{w,u}$. With such a simplification, the asymptotic solutions are therefore reduced to the linear expression $u_1^+ = x_n^+$ in the viscous sublayer and to the log-law in the inertial subrange. It is important to keep in mind that the general wall function (GWF) used in this work is a simplification of the original formulation. Subsequently, due to the coarseness of the meshes considered in the following, the point of extraction in $x_n = h_{w,u}$ will be located in the inertial subrange. Hence, the simplified GWF will correspond to the log-law.

As a first stage, the x-coordinate of the transition location x_t is simply taken from the literature and hard-coded in INCA. From this knowledge, the model switches between the two wall functions by applying the LWM in $x \leq x_t$ and the GWF in $x > x_t$.

In a second phase, a sensor measuring the turbulent kinetic energy is implemented in order to determine the type of regime locally and thus automatically switch between the two wall functions. Relying on Bodart et al. [86], the turbulent kinetic energy in viscous units is consistently comprised between 2.5 and 4.0 in the log layer through a wide range of Reynolds numbers. Since $x_n = h_{w,u}$ is expected to be located in this region,

it seems suitable to compute the kinetic energy from the extracted velocity field used by the GWF. As done by Meneveau et al. [87], a temporal low-pass filter with an exponential kernel is used to obtain a time-filtered value $\langle f \rangle$ of f from the ODE

$$\frac{d\langle f \rangle(t)}{dt} = \frac{f(t) - \langle f \rangle(t)}{T(t)}, \tag{6.1.1}$$

with $T(t)$ the characteristic time of averaging. The resolution of Eqn 6.1.1 leads to

$$\langle f \rangle^n = \left(1 - e^{-\Delta t/T}\right) \cdot f^n + e^{-\Delta t/T} \cdot \langle f \rangle^{n-1}, \tag{6.1.2}$$

with n corresponding to the index denoting the current time step and Δt the time step increment. In order to capture the large-scale unsteadiness, Bodart et al. [86] defined the characteristic time as

$$T(t) = \left(S_{ij} S_{ij}\right)^{-1/2}, \tag{6.1.3}$$

where S_{ij} is the strain-rate tensor at the edge of the wall model. However, for the sake of performance, $T(t)$ will be simply imposed as a constant in the whole domain for the rest of this work and its value will be expressed with respect to the free-stream velocity U_∞ and the chord length c as

$$T = \tau \cdot c/U_\infty, \tag{6.1.4}$$

with τ being an arbitrarily imposed time factor.

The established low-pass filter enables to compute the turbulent kinetic energy k expressed as

$$k = \langle u_i' u_i' \rangle = \langle u_i u_i \rangle - \langle u_i \rangle^2, \tag{6.1.5}$$

where the velocity field is written as

$$u_i = \langle u_i \rangle + u_i'. \tag{6.1.6}$$

Then, fitting with the formulation of Larsson et al. [3], the sensor is defined as

$$s_w(t) = \frac{\rho\ k(t)}{\langle \tau_w \rangle(t)}, \tag{6.1.7}$$

at each point of the wall. In this work, the denominator is obtained by averaging the wall-shear stress from the GWF only. Nevertheless, this latter is expected to tend towards zero at the stagnation line vicinity, thus leading to extremely high sensor values that do not represent any turbulent activity. Therefore, for convenience, the sensor will only be used from 5% of the chord length and the upstream region will be assumed as fully laminar. Downstream, if the sensor exceeds an imposed threshold $s_{\mathrm{w,thr}}$, the wall-shear stress is estimated from the GWF and otherwise, from the LWM. Eventually, the sensor update will be achieved after each range of 500 iterations. The main motivation is to avoid any turbulent production due to the sensor itself.

The resulting HWM is summarized in Fig 6.1. The heights of extraction are respectively imposed by default as

$$h_{w,p} = 2 \cdot \Delta_{\min} \qquad \text{and} \qquad h_{w,u} = 2.5 \cdot \Delta_{\min},$$

with $\Delta_{\min}$ being the minimum cell size $\min(\Delta_x, \Delta_y, \Delta_z)$. In both cases, the information at the extraction point is obtained by applying a trilinear Lagrangian interpolation from the solution at the eight neighboring velocity-cell and pressure-cell centers.

In order to validate the HWM, the resulting pressure field and the imposed wall-shear stress will be studied in the following through the pressure coefficient $c_p(t, \mathbf{x})$, the local skin friction coefficient $c_{f,l}(t, \mathbf{x})$ and the friction coefficient $c_f(t, \mathbf{x})$ respectively expressed as

$$c_p(t, \mathbf{x}) = 2 \cdot \frac{p(t, \mathbf{x}) - p_\infty}{\rho U_\infty^2}, \tag{6.1.8}$$

$$c_{f,l}(t,\mathbf{x}) = 2 \cdot \frac{\tau_w(t,\mathbf{x})}{\rho U_e^2(t,\mathbf{x})}, \tag{6.1.9}$$

$$c_f(t,\mathbf{x}) = 2 \cdot \frac{\tau_w(t,\mathbf{x})}{\rho U_\infty^2}, \tag{6.1.10}$$

with the static pressure p resulting from a trilinear interpolation in $x_n = 2 \cdot \Delta_{\min}$ by default. In all three cases, a time averaging process is carried out to obtain representative statistics. To do so, the time-averaged value $\langle g \rangle$ of g is computed at the n^{th} iteration as

$$\langle g \rangle^{\,n} = \frac{g^n + (n - n_0) \cdot \langle g \rangle^{\,n-1}}{n - n_0 + 1}, \tag{6.1.11}$$

where n_0 is the first step from which the averaging process starts. Then, a spanwise averaging is achieved leading to the time-averaged two-dimensional pressure and skin friction coefficients respectively denoted c_p, $c_{f,l}$ and c_f.

Lastly, the averaging period is specified for each of the three configurations in Tab 6.1. The flow statistics and time-averaged two-dimensional pressure and skin friction coefficients presented in the following are obtained by only considering the results through this range of time. On the other side, regarding the sensor, both turbulent kinetic energy and averaged wall-shear stress from the GWF are obtained by considering the solution from the beginning of the simulation.

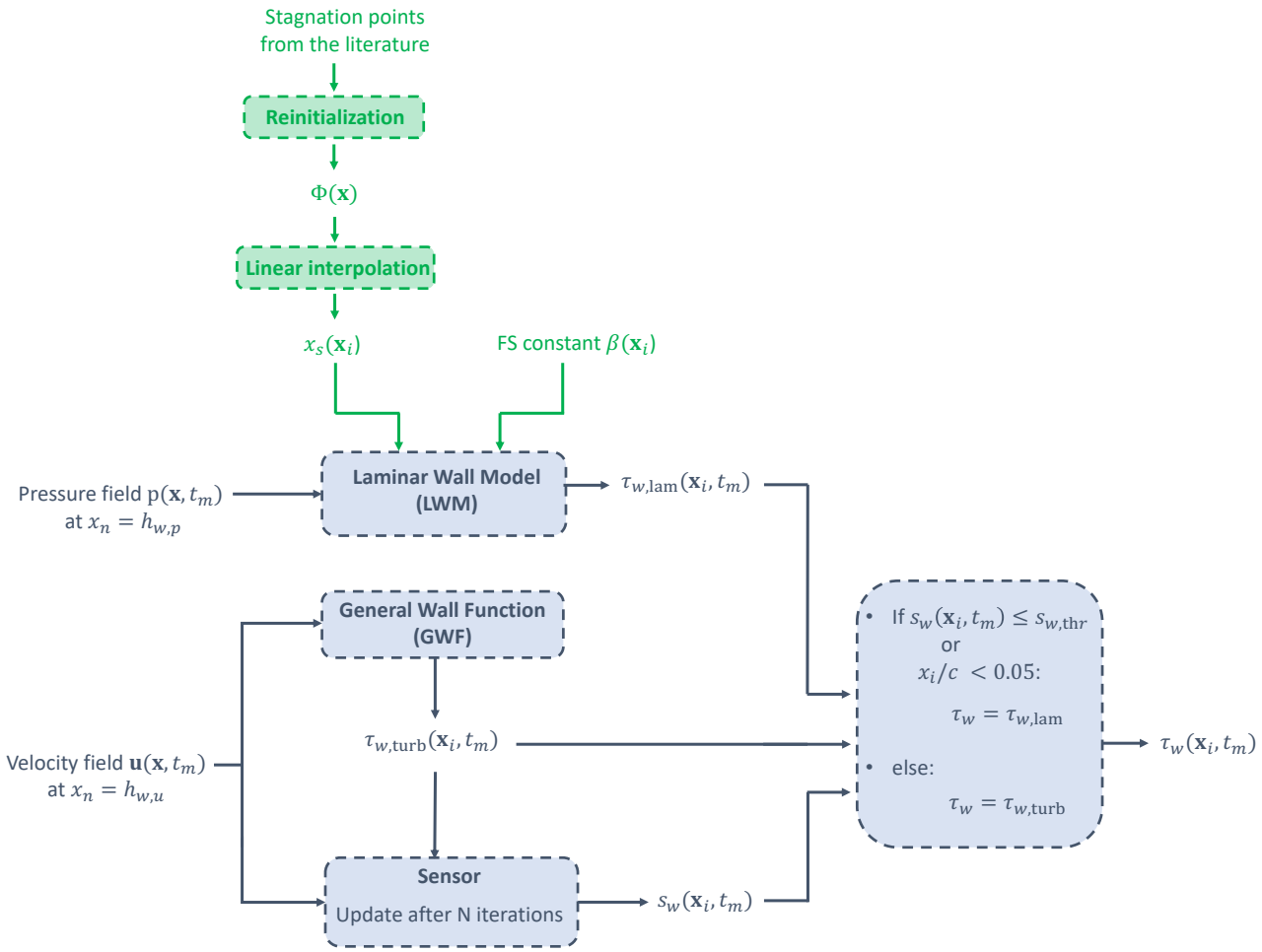

Figure 6.1: Hybrid wall model (HWM) with transition detection. Schematic representation of the model considering the wall point $\mathbf{x}_i$ at the m^{th} time step (blue part) and the related pre-processing (green part).

	Averaging process
NACA0012	from $t = 10$ to $20c/U_\infty$
A-airfoil C3	from $t = 10$ to $25c/U_\infty$
A-airfoil C13	from $t = 10$ to $17c/U_\infty$

Table 6.1: Period of averaging to obtain the flow statistics and the time-averaged two-dimensional pressure and skin friction coefficients.

6.2 NACA0012

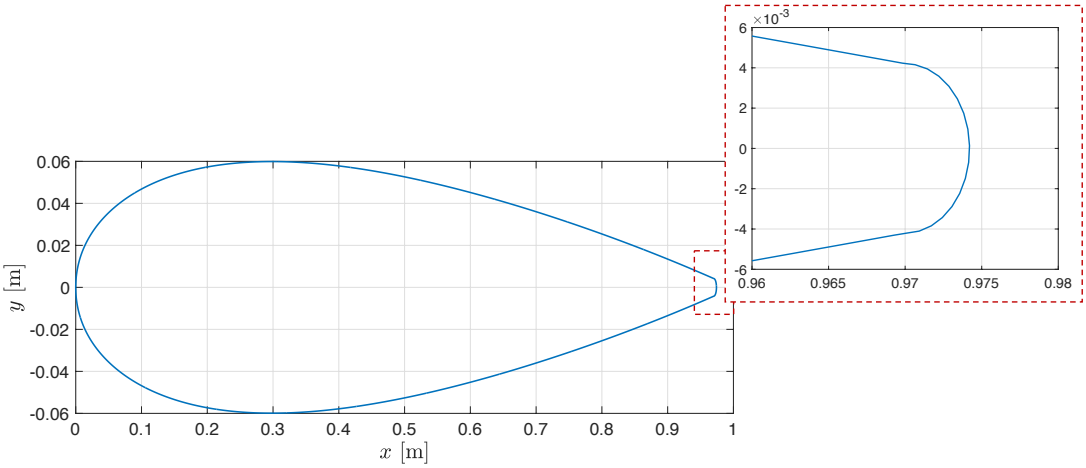

Figure 6.2: NACA0012 with a rounded trailing edge in $x = 0.97$ [m].

The flow around a NACA0012 is first investigated by imposing $Re = 10.25 \cdot 10^6$ and a zero inclination. Hence, it is possible to take advantage of the symmetry and simulate only the upper side of the profile. The chord is imposed as $c = 1$ [m] and the domain sizing such that

$$x/c \in [-10\ ;\ 10], \qquad y/c \in [0\ ;\ 10], \qquad z/c \in [-0.175\ ;\ 0.175],$$

for a leading edge located in $(x/c, y/c, z/c) = \mathbf{0}$. For numerical considerations, the sharp trailing edge is cut in $x/c = 0.97$ and replaced by a half-circle as shown in Fig 6.2. Despite that, the reference length will be kept as $c = 1$ [m] to fit with the external data from the literature.

Afterwards, the mesh generation is achieved by applying the adaptive mesh refinement (AMR) method in the xy-plane. For this setup, two meshes are considered: a fine and a coarse grid. Their respective characteristics are summarized in Tab 6.2 and the resulting coarse mesh is illustrated in Fig 6.3.

		Coarse	Fine
Initial grid resolution: $N_x \cdot N_y \cdot N_z$		$30 \cdot 15 \cdot 40$	$60 \cdot 30 \cdot 40$
Number of refinement steps		4	4
Refinement ratio		3	3
Total nbr of cells		$1.89 \cdot 10^6$	$7.56 \cdot 10^6$
Airfoil contour	$\Delta_{x,y}/c$	$2.8 \cdot 10^{-3}$	$1.4 \cdot 10^{-3}$
	Δ_z/c	$8.7 \cdot 10^{-3}$	$8.7 \cdot 10^{-3}$
	Nbr of cut cells	$15.9 \cdot 10^3$	$31.2 \cdot 10^3$

Table 6.2: Characteristics of the fine and the coarse mesh resulting from the AMR method for the NACA0012.

Regarding the boundary conditions, a uniform horizontal flow is imposed in $x/c = -10$ with a speed norm $U_\infty = 1$ [m/s] and a zero pressure gradient. Then, a symmetry is enforced in $y/c = 0$. In addition, both boundaries in $y/c = 10$ and $x/c = 10$ are based on a first order Neumann condition for velocities and a zero static pressure. Lastly, both faces normal to the spanwise direction are defined as periodic boundaries. The flow is assumed to be incompressible with a unit density and a kinematic viscosity $\nu = 1/(10.25 \cdot 10^6)$ [m^2/s].

Finally, it is necessary to provide the level-set function Φ related to the STL file in Fig 6.2 for a set of stagnation points imposed in $(x/c, y/c) = \mathbf{0}$. To that end, algorithm 4 is applied while monitoring the

convergence of the main loop through the L^2 norm of the relative change in Φ, see Fig 6.4a. The resulting steady field is illustrated in Fig 6.4b and presents a good correspondence with respect to the curvilinear coordinates from *Xfoil* [88].

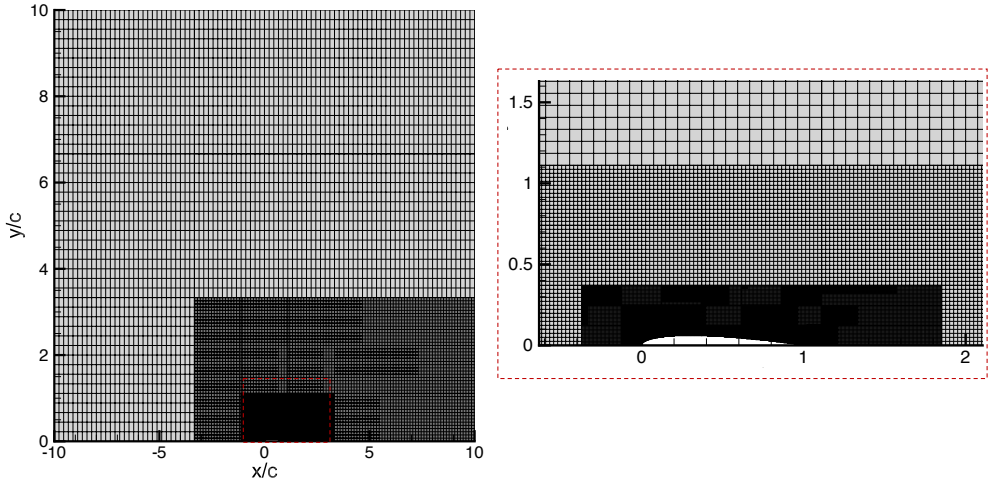

Figure 6.3: Coarse mesh resulting from the AMR method used to simulate the flow around a NACA0012. Illustration with solid cell blanking.

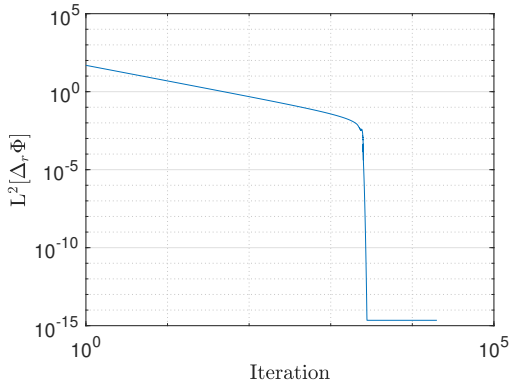

(a) L^2 norm of the relative change in Φ expressed in Eqn 5.2.4 through the main loop.

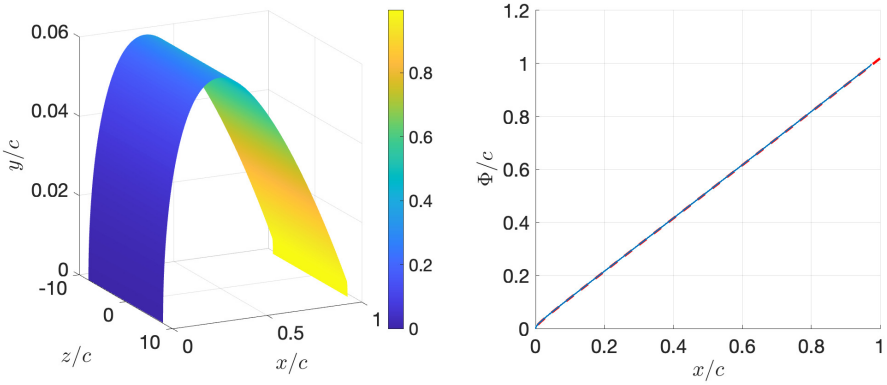

(b) Level-set function divided by the chord length Φ/c over the geometry in 3D (left side) and with respect to the x-coordinate (blue points; right side). Φ/c is compared to the curvilinear coordinates from *Xfoil* (dashed line, red; right side).

Figure 6.4: Results from the improved reinitialization process 4 for the NACA0012 defined in Fig 6.2 and with a stagnation line imposed in $(x/c, y/c) = \mathbf{0}$.

6.2.1 Hard-Coded Transition with Fine Mesh

Relying on the empirical data obtained by Becker [89], the transition point is imposed in $x/c = 0.2$ and the hybrid model is applied accordingly with the fine mesh. The resulting mean flow is illustrated in Fig 6.5. The averaged chordwise velocity $\langle u \rangle$ and static pressure field $\langle p \rangle$ reveal that the flow initially presents a stagnation at the leading edge vicinity, followed by an acceleration and then a deceleration until reaching the trailing edge. The flow does not present any separation and recirculation region. Focusing on the boundary layer observed in Fig 6.5a, it is possible to underline the coarseness of the mesh due to the steep increase of velocity from the wall to the first grid point and the changes in the shape of a staircase step following the geometry profile. It is therefore important to keep in mind the potential influence of the mesh resolution in the following of this analysis.

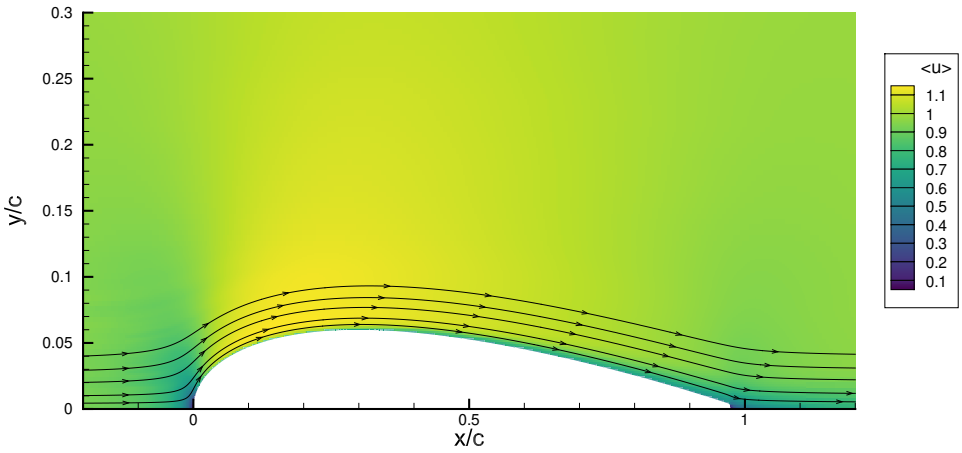

(a) Averaged velocity field $\langle u \rangle$ aligned with the x-direction.

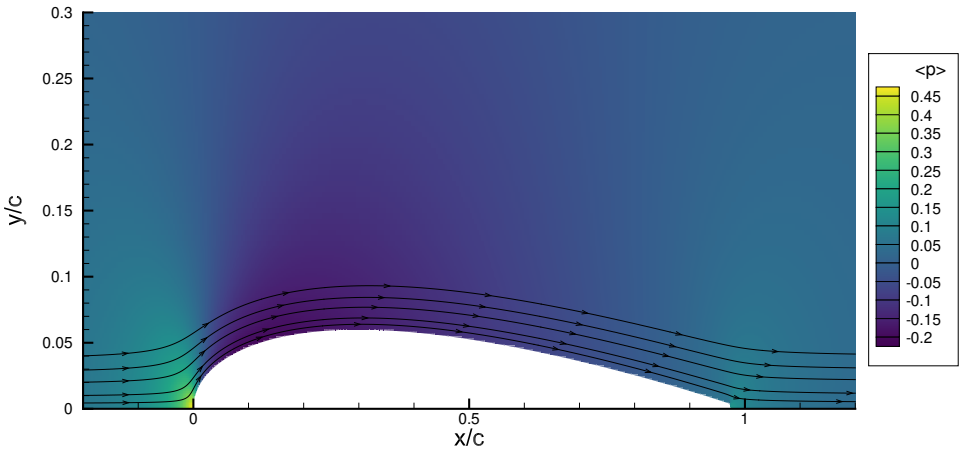

(b) Averaged pressure field $\langle p \rangle$.

Figure 6.5: NACA0012: HWM with hard-coded transition and fine mesh. Averaged solution illustrated with streamlines (black lines).

Then, the instantaneous solution at the middle slice of the domain after $20c/U_\infty$ is considered. The corresponding velocity field in Fig 6.6 reveals important upstream and downstream oscillations. Concerning those upstream, an analysis about their origin and consequences on the sensor will be achieved in Sec 6.2.2. Additionally, it is important to remind that only the upper half of the domain is represented by assuming a perfect symmetry between the upper and lower part. This assumption has been justified by the horizontal

incoming flow and the symmetry of the airfoil, but without taking the turbulent wake into account. Nevertheless, it is obvious that this region of the flow develops three-dimensional structures independently of the plane of symmetry. It is therefore important to keep a critical eye regarding the turbulent structures obtained in the wake of the instantaneous solution and the potential effect of this simplification on the overall solution.

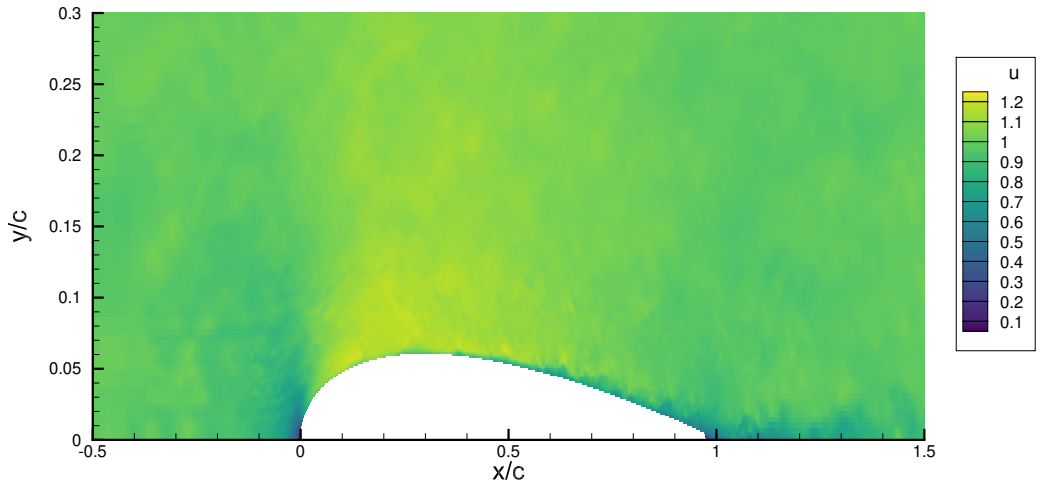

Figure 6.6: NACA0012: HWM with hard-coded transition and fine mesh. Instantaneous velocity field aligned with the x-direction, in $t = 20c/U_\infty$ and at the middle slice of the domain.

The study is then refocused on the vicinity of the wall. To do so, the pressure distribution is first compared with the one predicted by *Xfoil* considering a zero Mac number in Fig 6.7a and 6.7b. Globally, both solutions present a good correspondence up to $x/c = 0.97$. Beyond, a significant drop of pressure is observed and that, due to the introduction of the rounded trailing edge. Additionally, the pressure distribution presents oscillations through the entire range, all the more pronounced around the suction peak. Two potential causes can be identified: the geometry definition over the Cartesian mesh and the interpolation process. On the one hand, for such a mesh resolution, the geometry cannot be perfectly captured, thus leading to abrupt jumps of the represented profile only defined cut cell by cut cell. On the other hand, it seems relevant to question the effect of the trilinear assumption used during the interpolation process at the pressure extraction points.

The pressure field is then injected within the LWM and used to estimate the external flow velocity by applying Bernoulli 3.5.16. In order to check the validity of this process, the resulting speed is compared with the one obtained from *Xfoil* in Fig 6.7c. The good match observed between both solutions enables to validate the external flow velocity computation from the pressure field.

There are now all the elements to compute the wall-shear stress in both laminar and turbulent regions by applying the HWM. The resulting local skin friction coefficient is compared with respect to the empirical data [89] and *Xfoil* in Fig 6.7d. Concerning *Xfoil*, the parameter N_{crit} is imposed at 4 to get a transition as close as possible to $x/c = 0.2$. Globally, both computed friction distributions correspond relatively well with the empirical one. Focusing on the laminar part in Fig 6.7e, a good correspondence is found between the three solutions in a global sense and the LWM leads to a very slight overestimation at the transition point vicinity.

Regarding the turbulent region, the GWF first leads to an important overestimation in the zone following the turbulent transition. Then, the offset decreases downstream and the GWF ends up matching relatively well with the empirical data from $x/c \simeq 0.45$. A similar behavior is observed with the friction predicted by *Xfoil*. In this case, however, the overestimation region is much shorter compared to the one related to the GWF. In addition, the GWF leads to a relatively smooth friction distribution from $x/c = 0.2$ to 0.4 and then

presents wiggles with an increasing frequency downstream. As for the pressure, the two plausible causes are the mesh resolution and the trilinear interpolation process, in this case, applied to the velocity input data at the extraction points.

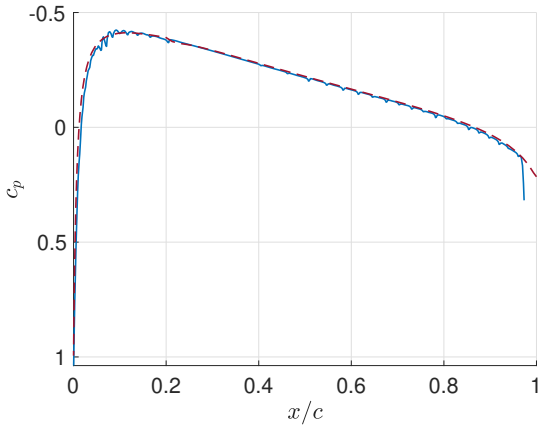

(a) Pressure coefficient.

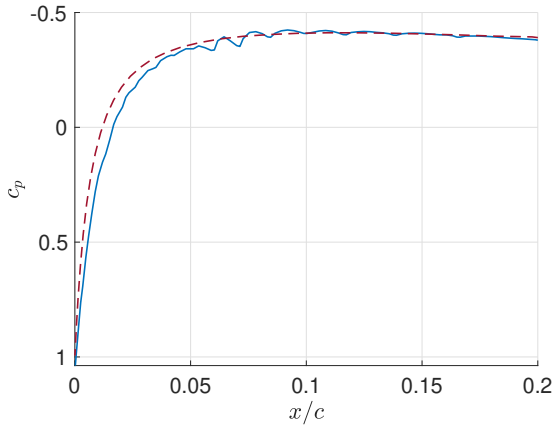

(b) Zoom of c_p in the laminar part.

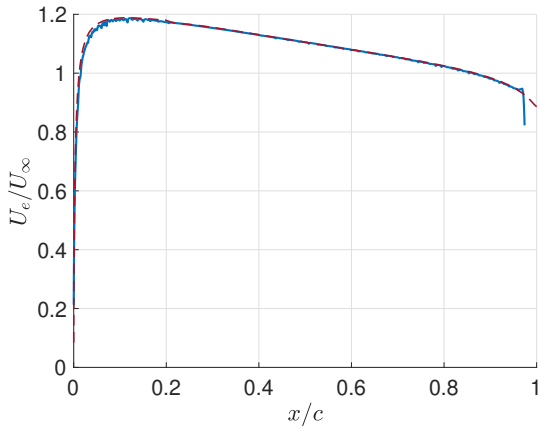

(c) External flow velocity.

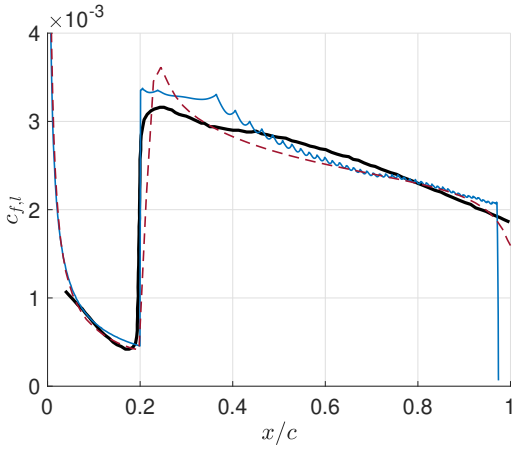

(d) Local skin friction coefficient.

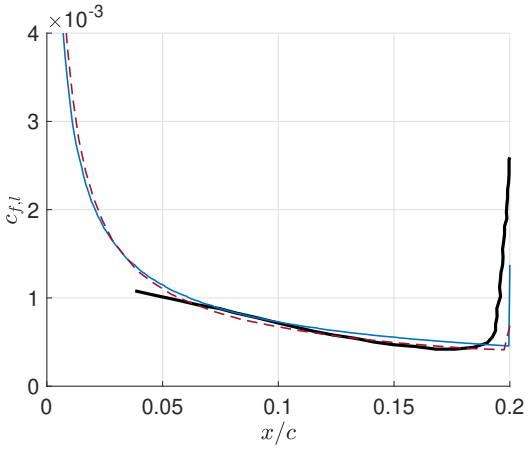

(e) Zoom of $c_{f,l}$ in the laminar part.

Figure 6.7: NACA0012: fine mesh. Skin friction, pressure and external flow velocity related to the HWM with hard-coded transition (solid line, blue), to *X-foil* with $N_{\text{crit}} = 4$ (dashed line, red) and to the experiment [89] (solid line, black).

Afterwards, the trilinear interpolation process is applied to the pressure field to obtain the pressure distribution around the profile at different wall distance x_n, see Fig 6.8. Globally, varying the wall distance x_n does not imply any significant change regarding the pressure distribution, but only a slight decrease of the suction peak. This observation brings out the robustness of the LWM with respect to the height of extraction $h_{w,p}$, in contrast to a model fed with the velocity field. Subsequently, the zoom on the suction peak in Fig 6.8b shows that the smaller the distance x_n, the greater the amplitude of oscillation for a constant frequency. One plausible explanation is the consequence of the trilinear assumption during the interpolation process. Indeed, reducing the wall distance leads to a stencil located in a region with a more pronounced non-linearity and thus, the linear process leads to a distribution presenting more abrupt variations. Consequently, although the variation of the pressure is weak with respect to the wall distance, it is advised not to achieve the linear interpolation too close to the wall in order to avoid significant spurious oscillations as observed with $x_n = 1 \cdot \Delta_{\min}$.

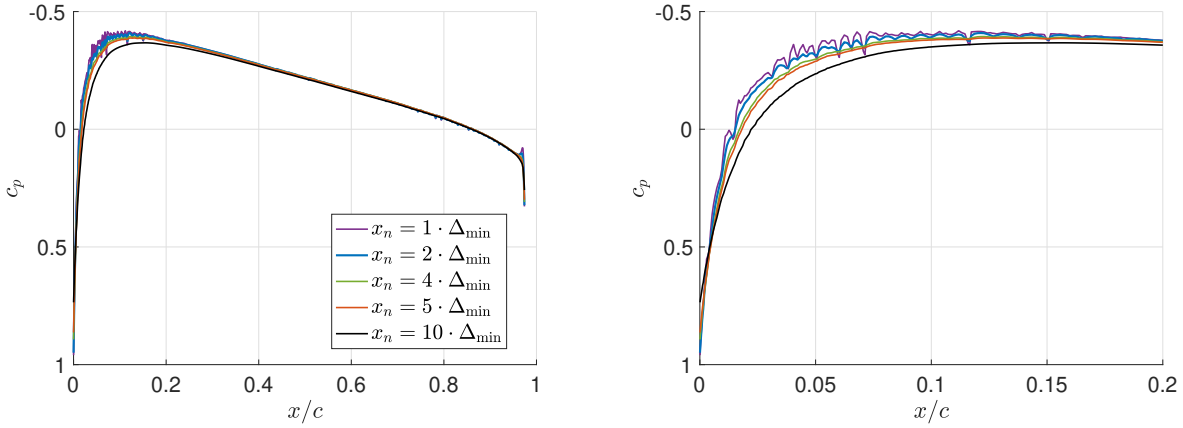

(a) Pressure coefficient.

(b) Zoom of c_p in the laminar part.

Figure 6.8: NACA0012: HWM with hard-coded transition and fine mesh. Pressure distribution at different wall distance x_n expressed with respect to the minimum grid cell size at the wall $\Delta_{\min}$.

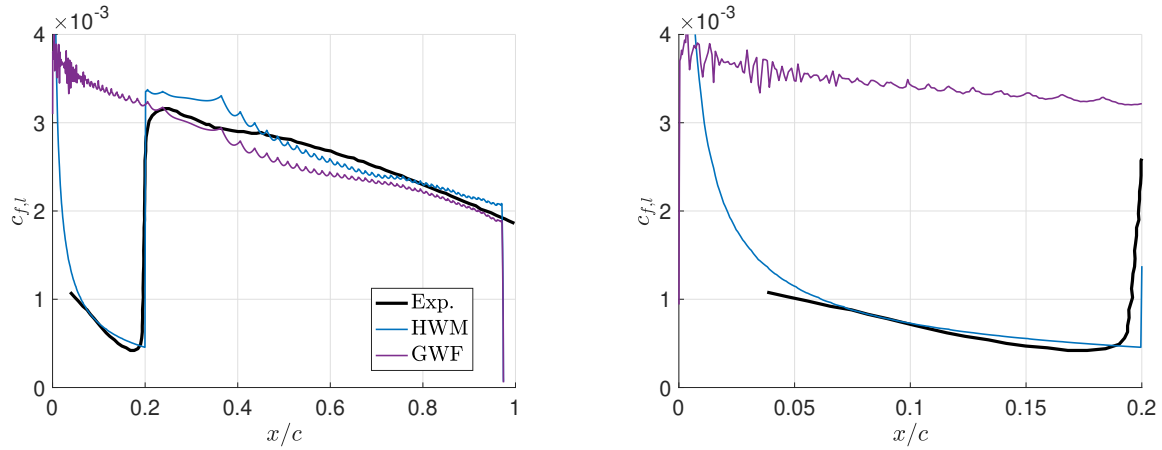

(a) Local skin friction coefficient.

(b) Zoom of $c_{f,l}$ in the laminar part.

Figure 6.9: NACA0012: fine mesh. Friction obtained from the GWF, i.e. assuming a fully turbulent flow, and from the HWM with hard-coded transition. Both cases are compared to the empirical friction [89] (black line).

Lastly, the HWM is compared to a fully turbulent wall modeling by considering the GWF over the entire surface. The comparison of their respective friction distribution in Fig 6.9 brings out that the GWF leads to an important overestimation of the laminar wall-shear stress, whereas the LWM enables to obtain a signifi-

cantly better match with respect to the empirical data. As an order of magnitude, the ratio between both estimates is around 4 in the laminar region. Hence, this brief comparison demonstrates the interest of the LWM compared to the existing turbulent wall model.

Thus, for this first analysis, the HWM with hard-coded transition leads to a wall-shear stress corresponding relatively well with the empirical data and *Xfoil* in a global sense, despite a coarsely resolved boundary layer. The match is particularly good in the laminar region, whereas the GWF leads to a short overestimation zone with respect to the experiment downstream of the transition location. Additionally, the robustness of the LWM regarding the height of extraction $h_{w,p}$ is demonstrated with the analysis of the pressure distribution in function of the wall distance x_n. Finally, the comparison between the LWM and the GWF in the laminar region brings to light the significant improvement in wall-shear stress prediction brought by the laminar modeling.

6.2.2 Mesh Resolution

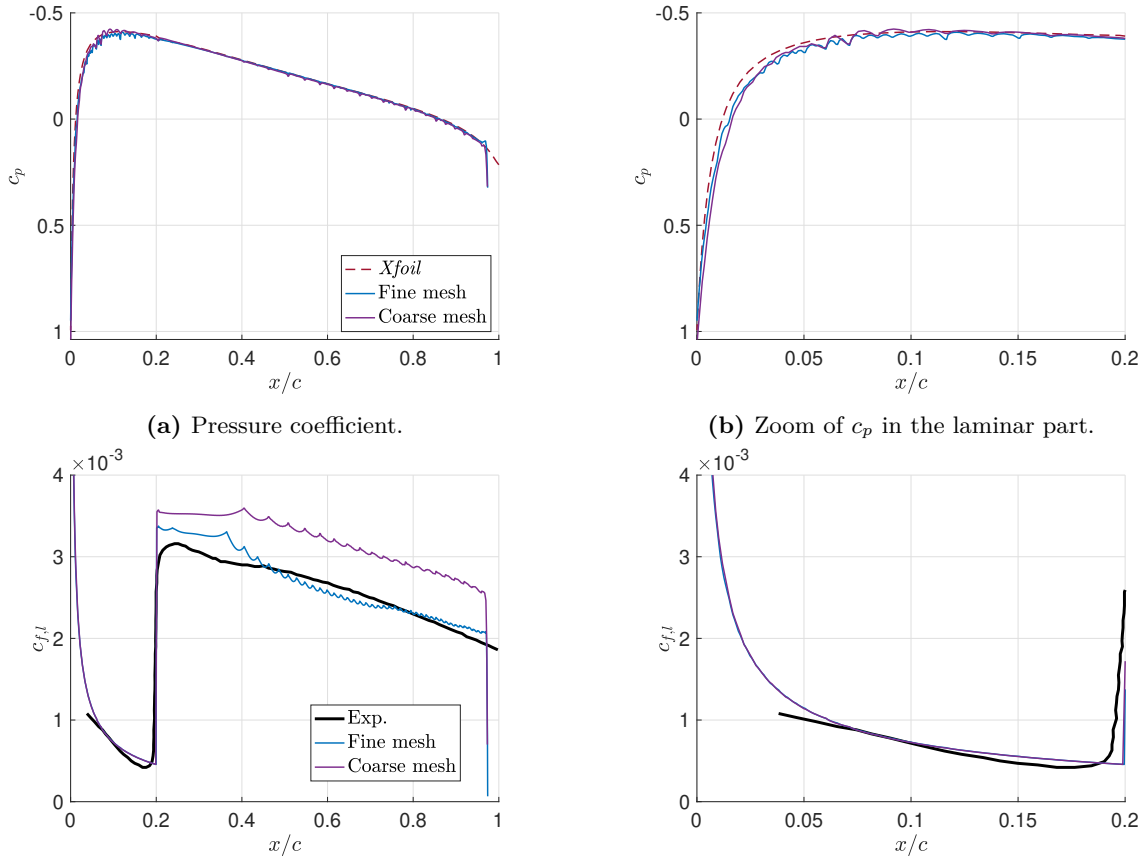

(a) Pressure coefficient.

(b) Zoom of c_p in the laminar part.

(c) Local skin friction coefficient.

(d) Zoom of $c_{f,l}$ in the laminar part.

Figure 6.10: NACA0012: HWM with hard-coded transition. Influence of the mesh resolution on the skin friction and on the pressure. The results are compared with those from *Xfoil* (dashed line, red) and from the experiment [89] (solid line, black).

The effect of the grid resolution is then studied by considering the two fine and coarse meshes defined in Tab 6.2 with a hard-coded transition in both cases. Starting with the pressure distribution in Fig 6.10a and 6.10b, it is possible to conclude that the two resolutions lead to similar results, albeit slightly different in the region of the suction peak. In both cases, this area presents wiggles whose frequency increases with the mesh resolution, and whose oscillation amplitude is slightly greater with the coarse grid.

Regarding the friction distribution, Fig 6.10c highlights the effect of the mesh refinement leading to a much better match with respect to the empirical data in the turbulent region. The fine mesh enables to

significantly decrease the overestimation of the turbulent wall-shear stress compared to the coarse grid. As observed in the pressure distribution, the turbulent part presents wiggles in both cases, with comparable oscillation amplitudes and a higher frequency for the fine mesh. Subsequently, Fig 6.10d reveals that the grid resolution has a much weaker effect in the laminar part. It is in fact difficult to distinguish the laminar friction distributions of the two meshes. This observation is in line with the discussion about the pressure coefficient, which is expected since the LWM is only fed with this latter.

Since the mesh refinement does not enable to significantly attenuate the oscillations in the pressure and the friction distribution, but mainly implies a higher frequency, the major cause therefore seems to be the trilinear interpolation process of the pressure and of the velocity input data at the extraction points. In order to validate this speculation, it would be interesting to consider a higher-order interpolation process. However, such a method is currently being implemented in INCA, but is not yet available.

In a second stage, the effect of the mesh size on the upstream velocity field fluctuations is studied. To that end, the Reynolds stress component $\langle u'u' \rangle$ is illustrated in Fig 6.11 for both mesh resolutions. This comparison underlines a strong reduction in upstream fluctuations with an increasing mesh resolution. The origin of the latter seems to be a direct consequence of the incompressible hypothesis, which implies that any local disturbance has an effect on the whole domain. Hence, the changes in flow around the profile have an impact on both upstream and downstream regions. In this context, it is important to specify that the spatial discretization method is a non-dissipative central second order scheme [23]. As a result, the upstream variations are conserved and transported downstream, thus affecting the solution near the wall. To overcome that, a first straightforward solution would be to use a compressible solver. However, because of the much higher calculation costs involved, this possibility is not considered in this work. On the other side, it is also relevant to investigate the spatial discretization by introducing dissipation with an upwind scheme. Two trials, of third and fifth order respectively, were carried out, both leading to an unstable process. It would be interesting to analyze this deeper to completely get rid of these incoming fluctuations. Nevertheless, since the amplitude is strongly attenuated with the mesh refinement, no further research is carried out in the following.

Then, focusing on the boundary layer related to the fine mesh in Fig 6.11a, the Reynolds stress distribution shows a smooth increase until reaching a maximum around $x/c \simeq 0.6$ followed by a slight decrease until the trailing edge. It is, nevertheless, not possible to observe a significant Reynolds stress rise translating a clear turbulent transition, which is expected due to the mesh resolution. A similar trend, although less pronounced, is observed with the coarse mesh in Fig 6.11b. This illustration also reveals that the upstream fluctuations significantly impact the boundary layer vicinity and in particular the leading edge.

Lastly, it seems necessary to assess the consequences of such upstream oscillations on the sensor. To that end, the sensor distribution is analyzed in Fig 6.12 with a time factor $\tau = 1$ for the two meshes. Considering a threshold $s_{\mathrm{w,thr}}$ above 2, it brings out that the coarse mesh presents a mainly turbulent surface, while the fine mesh, showing much weaker upstream fluctuations, predicts a well-defined laminar region. Since both averaged friction fields from the GWF $\langle c_f \rangle$ are relatively similar, it is thus possible to conclude that the upstream fluctuations significantly impact the measured turbulent kinetic energy k/U_∞^2 and consequently the sensor values. Indeed, whereas the fine mesh shows a low-energy zone followed by a high-energy region downstream, the coarse mesh leads to high-energy spots all over the surface. Since a coarser mesh resolves a weaker range of turbulent structures, this higher turbulent kinetic energy upstream can only be caused by the incoming fluctuations.

On the whole, the mesh refinement implies a strong improvement of the turbulent friction estimate from the GWF, while no significant change is observed regarding the LWM. In addition, the pressure and friction distributions show oscillations for both mesh resolutions, with the major difference being a higher frequency with the fine mesh. Based on this, such wiggles seem to be mainly caused by the trilinear interpolation of the pressure and of the velocity input data at the extraction points. To overcome that, it would be relevant to increase the order of interpolation. Subsequently, the velocity field presents in both cases upstream fluctuations, whose cause seems to be the incompressibility hypothesis. The latter, due to the use of a non-dissipative spatial discretization scheme, are conserved and significantly impact the sensor distribution at the wall vicinity in the case of the coarse mesh. To partially or completely get rid of this spurious effect, it appears appropriate to increase the grid resolution, modify the spatial discretization scheme or, if necessary, to use a compressible solver.

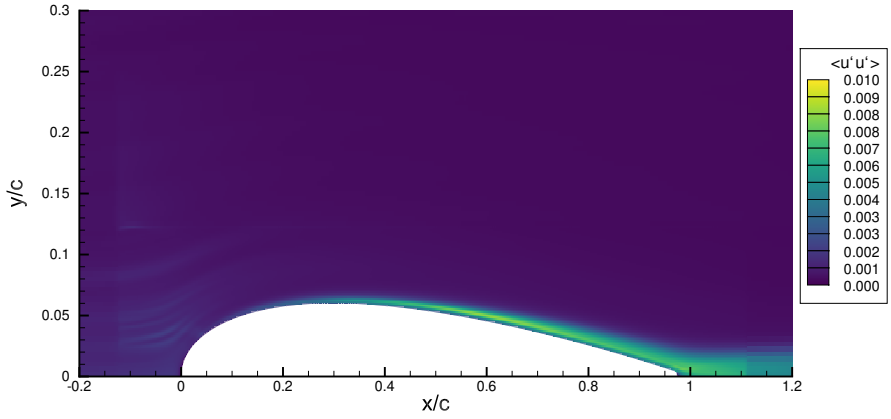

(a) Fine mesh.

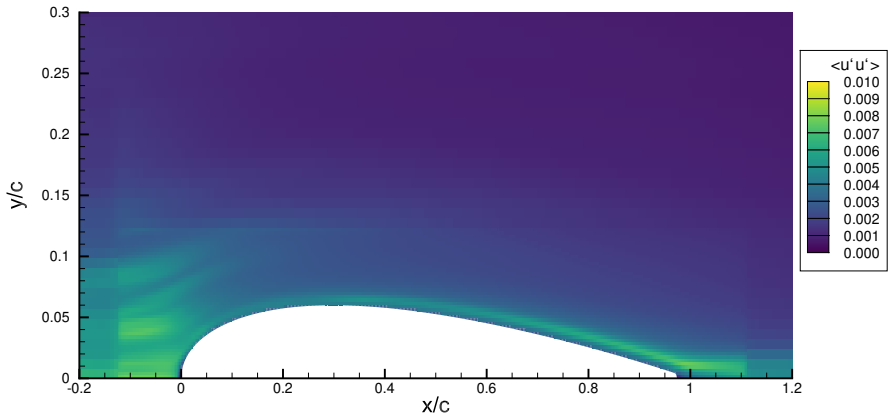

(b) Coarse mesh.

Figure 6.11: NACA0012: HWM with hard-coded transition. Influence of the mesh resolution on the Reynolds stress component $\langle u'u' \rangle$ with u' the chordwise speed fluctuation.

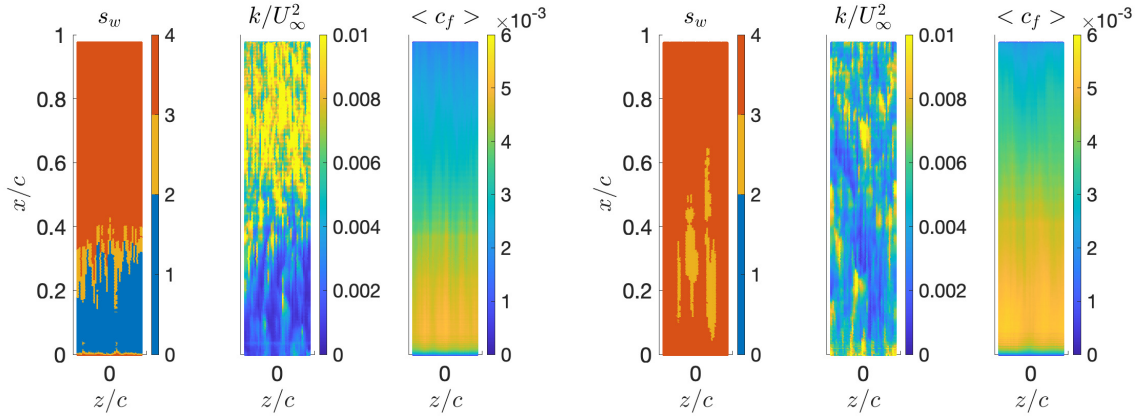

(a) Fine mesh. **(b)** Coarse mesh.

Figure 6.12: NACA0012: HWM with hard-coded transition. Influence of the mesh resolution on the sensor distribution s_w, on the turbulent kinetic energy k/U_∞^2 and on the averaged skin friction coefficient from the GWF $\langle c_f \rangle$ in $t = 20c/U_\infty$ and with a time factor $\tau = 1$.

6.2.3 Hard-Coded Transition with Coarse Mesh

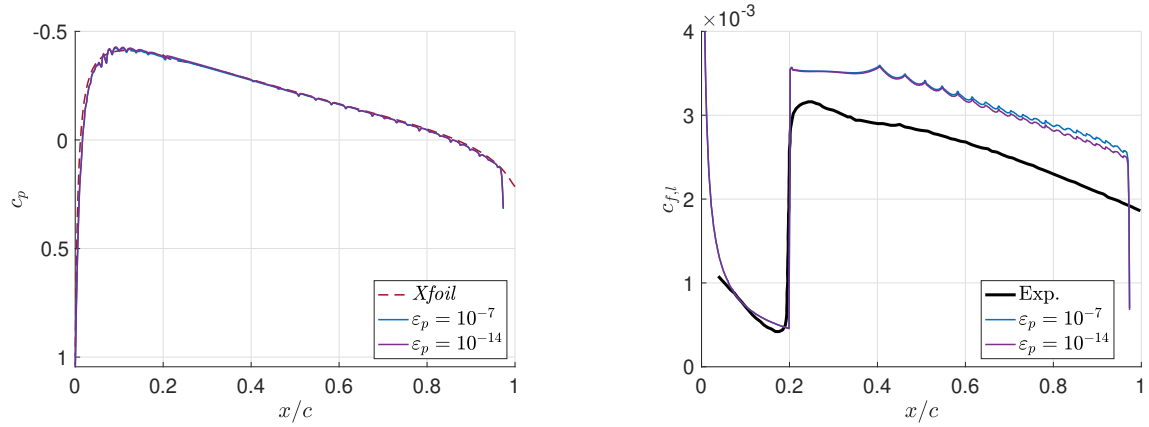

(a) Pressure coefficient. **(b)** Local skin friction coefficient.

Figure 6.13: NACA0012: HWM with hard-coded transition and coarse mesh. Influence of the Poisson residual value ε_p and comparison with the results from *Xfoil* (dashed line, red) and from the experiment [89] (solid line, black).

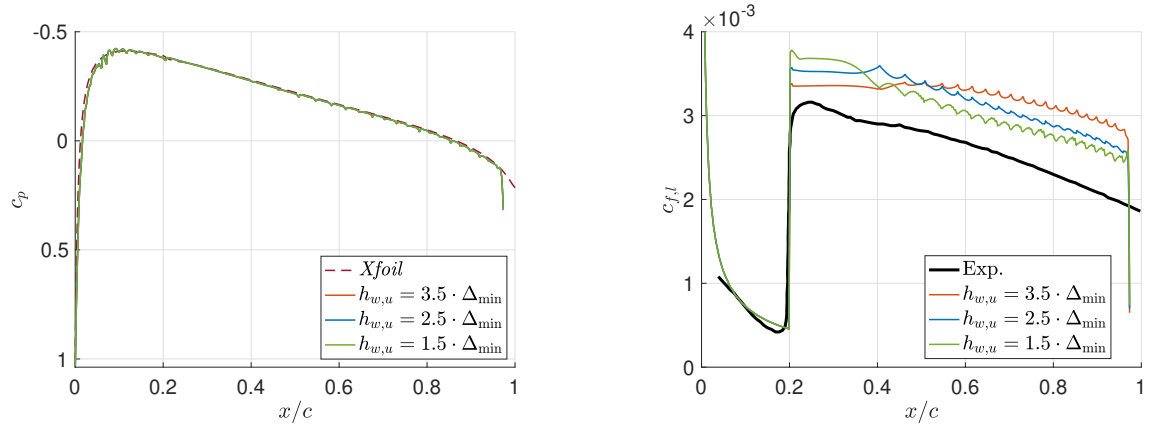

(a) Pressure coefficient. **(b)** Local skin friction coefficient.

Figure 6.14: NACA0012: HWM with hard-coded transition and coarse mesh. Influence of the height of extraction for the velocity field $h_{w,u}$ with a pressure extracted in $h_{w,p} = 2 \cdot \Delta_{\min}$, and comparison with the results from *Xfoil* (dashed line, red) and from the experiment [89] (solid line, black).

The analysis is now directed towards the turbulent friction overestimation encountered with the coarse mesh. The previous section has revealed that a mesh refinement enables to strongly reduce it. For the sake of completeness, it seems interesting to examine the effect of other factors as the Poisson solver residual ε_p and the height of extraction $h_{w,u}$ used during the interpolation of the velocity to feed the GWF.

In this work, the default value of the solver residual is $\varepsilon_p = 10^{-7}$. In order to assess such a threshold, two simulations are performed, one with the default value and one with a residual $\varepsilon_p = 10^{-14}$. Fig 6.13 reveals that decreasing the solver residual does not imply significant changes in pressure and friction distribution. The default value therefore seems low enough to obtain converged results.

Concerning the height of extraction $h_{w,u}$, Fig 6.14 brings out that this parameter has no clear effect on the friction obtained from the GWF. A better match with the empirical data is first observed at the transition vicinity with a higher $h_{w,u}$, whereas a weaker height leads to a better accuracy from $x/c \simeq 0.4$ to the trailing edge. Regarding the pressure distribution, the modification of the Neumann boundary condition with the

height of extraction does not imply any noticeable change.

Based on these two comparisons, it therefore seems that only a mesh refinement enables to significantly improve the correspondence between the turbulent wall-shear stress estimate from the GWF and the empirical data.

6.2.4 Findings

This first setup enables to assess the validity of the HWM with hard-coded transition in the case of a fully attached flow over a symmetric aerodynamic profile. From the results related to the fine mesh, it is possible to state that the predicted wall-shear stress matches relatively well with the empirical data despite the fact that the boundary layer is only partially resolved and coarsely represented, as underlined by the study of the mean flow. Additionally, the mesh resolution has a significant effect regarding the GWF, whereas the LWM is much less impacted. This latter also shows a strong robustness regarding the height of extraction $h_{w,p}$ due to the weak variation in pressure distribution as a function of the wall distance x_n, and offers a much better accuracy in the laminar region compared to a fully turbulent modeling with the GWF.

For the two meshes, the pressure and the friction distribution around the profile, both requiring a trilinear interpolation respectively at the pressure and velocity extraction points, present oscillations whose frequency increases with the mesh resolution without significant change in amplitude. Subsequently, varying the wall distance x_n used to define the extraction points for the pressure interpolation brings out that the oscillation amplitude is higher the closer to the wall. Based on these two observations, the trilinear assumption seems to be the main cause of these wiggles. In order to fully demonstrate these words, it would be necessary to apply a higher order interpolation process.

Finally, the analysis highlights the existence of upstream fluctuations in the velocity field. The cause seems to be the incompressibility assumption under which any local change near the wing is reflected in the entire domain. Since a central non-dissipative scheme is used, the upstream oscillations are conserved and propagate downstream until reaching the wall vicinity. This mainly affects the sensor prediction by biasing the estimate of the turbulent kinetic energy. Nevertheless, such an effect is strongly reduced by achieving a mesh refinement. On the other side, it is also possible to introduce dissipation by using an upwind scheme or avoiding this issue by employing a compressible solver.

Although with the fine mesh, the HWM friction corresponds well to the empirical data and the sensor shows a clear turbulent transition, only the hard-coded transition method is employed for this first setup due to the related significant computational cost. Simulations with transition detection will be investigated in the following with the A-profile.

6.3 A-Profile

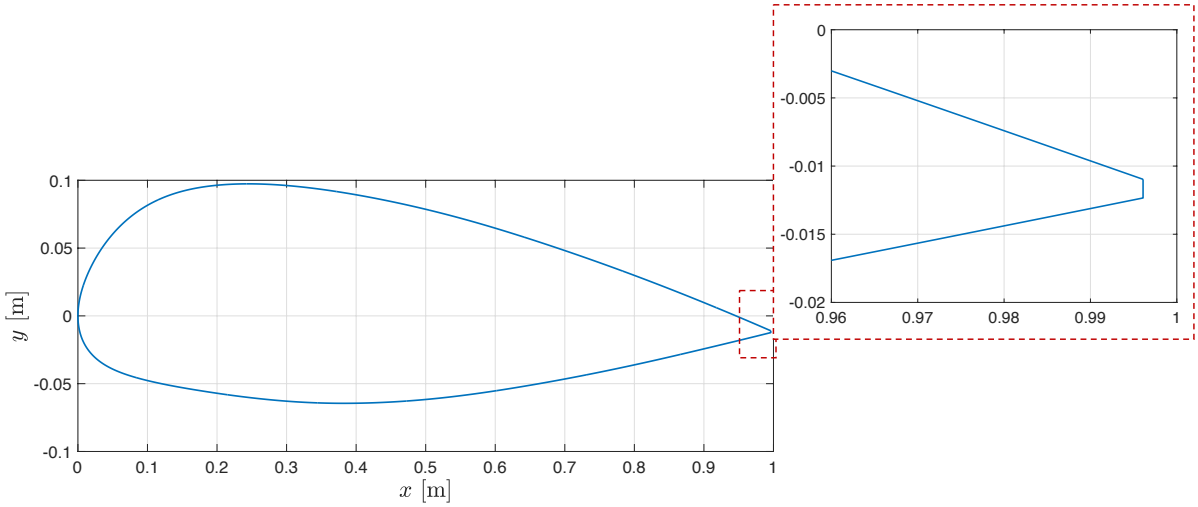

Figure 6.15: A-airfoil with a cut trailing edge in $x = 0.996$ [m].

The A-profile has been one of the test cases investigated by the EUROVAL (European Initiative on Validation of CFD Codes) project [90] and thus offers an interesting number of external studies. The principal source of this work is the CD-ROM [91] regrouping empirical data and numerical simulations for different flow configurations at a Mach number of 0.15. The measurements were performed in the F1 wind tunnel whose characteristics are summarized in [92]. In this analysis, two configurations are considered: ($Re = 3.1 \cdot 10^6$; AoA $= 3.4°$) and ($Re = 2.1 \cdot 10^6$; AoA $= 13.3°$). They will be respectively designated in the following as C3 and C13.

Foremost, the airfoil geometry is defined as shown in Fig 6.15 with a chord $c = 1$ [m]. For numerical considerations, the trailing edge is cut in $x/c = 0.996$ but the reference chord length is kept as $c = 1$ [m] in order to fit with the external setups. The domain sizing is imposed as

$$x/c \in [-10\ ;\ 10], \qquad y/c \in [-10\ ;\ 10], \qquad z/c \in [-0.15\ ;\ 0.15],$$

with the leading edge positioned in $(x/c, y/c, z/c) = \mathbf{0}$. The mesh is then generated by applying the AMR method. Its characteristics are summarized in Tab 6.3.

The inlet in $x/c = -10$ is defined as a uniform flow presenting an angle of attack AoA, a speed norm $U_\infty = 1$ [m/s] and a zero pressure gradient. Regarding the other three edges, a first order Neumann boundary condition for velocities and a zero static pressure are imposed. Lastly, the two faces normal to the spanwise direction are defined as periodic. The flow is assumed incompressible with a unit density and the kinematic viscosity is computed as $\nu = 1/Re$.

Eventually, the stagnation points and the transition locations are extracted from the empirical data related to the F1 tunnel and summarized in Tab 6.4. The stagnation location is determined by extracting the coordinate of the unit pressure coefficient. From this knowledge, it is thus possible to apply the reinitialization process for the two setups. The resulting level-set function distributions are represented in Fig 6.17.

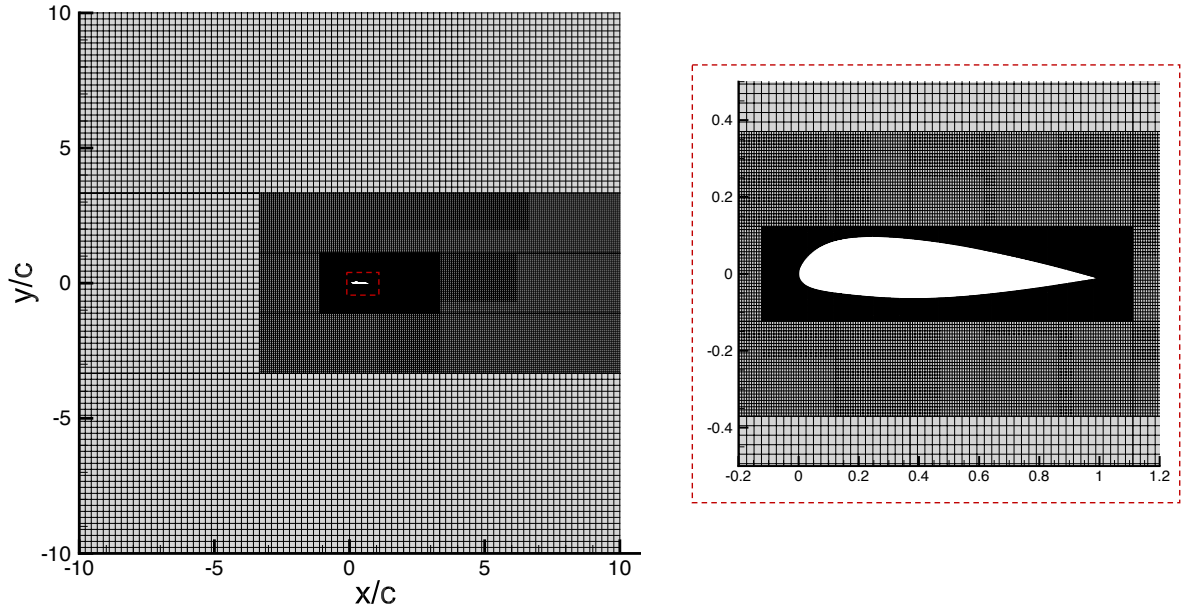

Figure 6.16: Mesh resulting from the AMR method used to simulate the flow around an A-airfoil. Illustration with solid cell blanking.

Initial grid resolution: $N_x \cdot N_y \cdot N_z$		$30 \cdot 30 \cdot 40$
Number of refinement steps		4
Refinement ratio		3
Total nbr of cells		$3.78 \cdot 10^6$
Airfoil contour	$\Delta_{x,y}/c$	$2.8 \cdot 10^{-3}$
	Δ_z/c	$7.5 \cdot 10^{-3}$
	Nbr of cut cells	$33.8 \cdot 10^3$

Table 6.3: Characteristics of the mesh resulting from the AMR method for the A-airfoil.

	C3	C13
Re	$3.1 \cdot 10^6$	$2.1 \cdot 10^6$
AoA	3.4°	13.3°
x_{st}/c	0.003 (press. side)	0.031 (press. side)
x_t/c (suc. side)	0.22	0.12
x_t/c (press. side)	No data	0.3

Table 6.4: Flow characteristics for the C3 and C13 configurations relying on the empirical data from the F1 tunnel [91]. x_{st} and x_t respectively correspond to the stagnation and the transition x-coordinate.

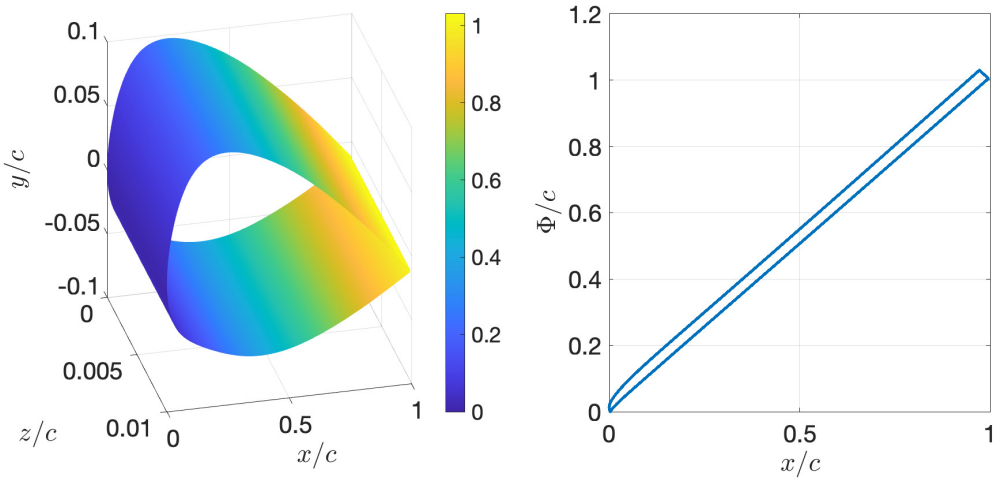

(a) C3 case with a stagnation line imposed in $x/c = 0.003$.

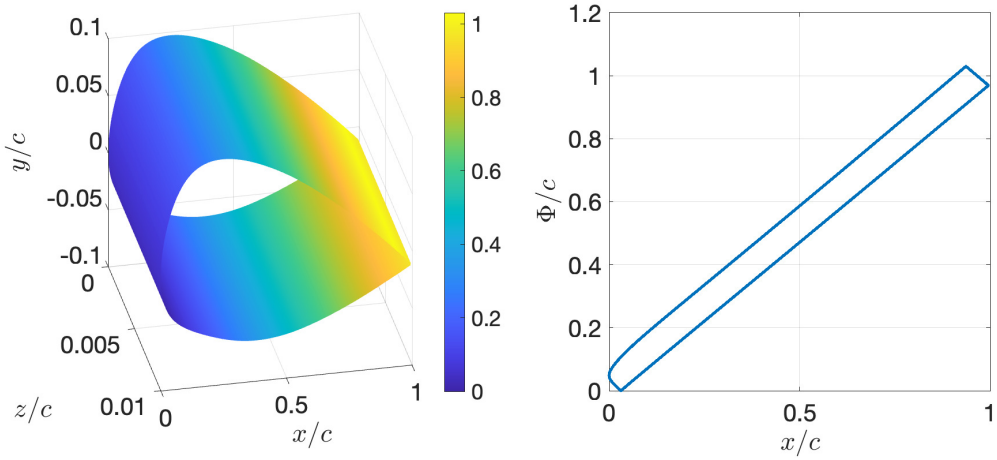

(b) C13 case with a stagnation line imposed in $x/c = 0.031$.

Figure 6.17: Results from the improved reinitialization process 4 for the A-airfoil defined in Fig 6.15. Level-set function divided by the chord length Φ/c over the geometry in 3D (left side) and with respect to the x-coordinate (right side).

6.3.1 C3 Configuration: Hard-Coded Transition

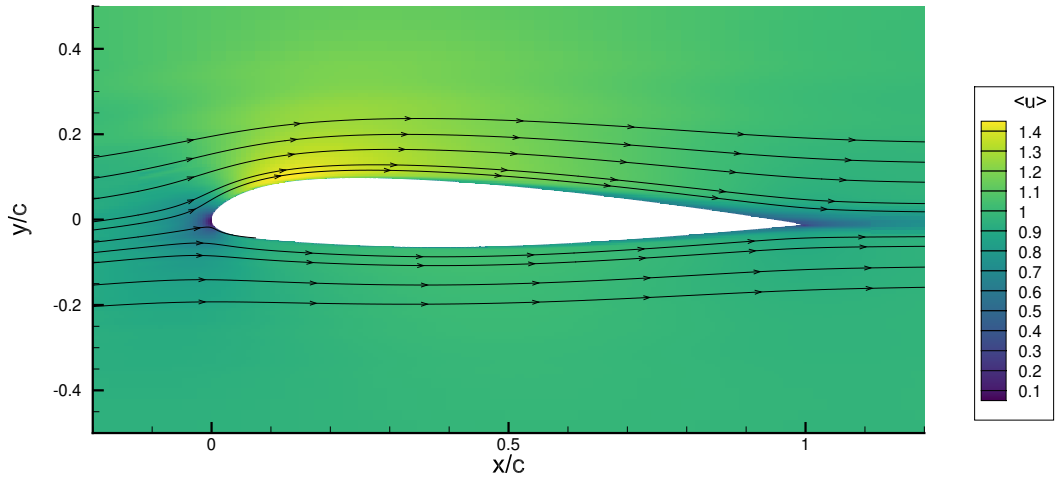

(a) Averaged velocity field $\langle u \rangle$ aligned with the x-direction.

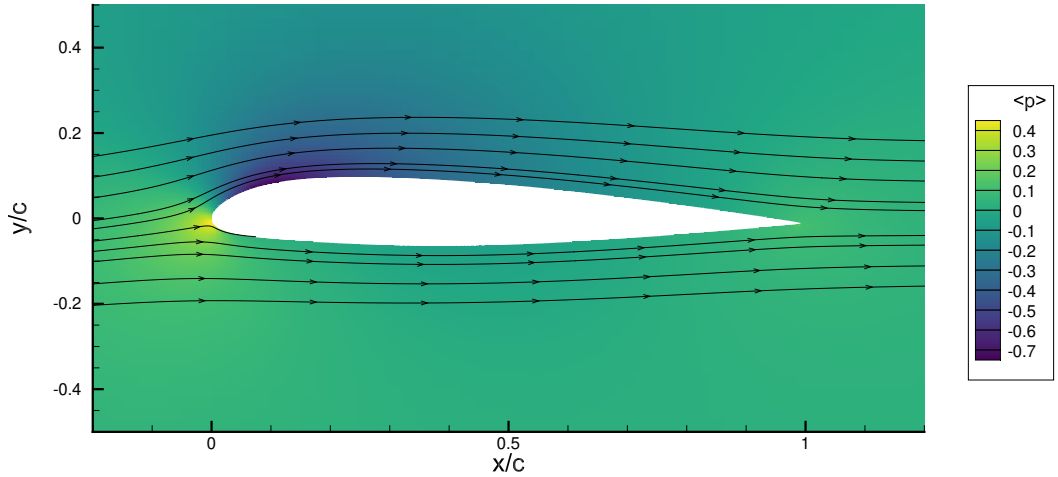

(b) Averaged pressure field $\langle p \rangle$.

Figure 6.18: A-airfoil in C3 configuration: HWM with hard-coded transition. Averaged solution illustrated with streamlines (black lines).

The C3 flow is first considered by hard-coding the transition point. As specified in Tab 6.4, the empirical data from the F1 tunnel enables to obtain a reliable transition point estimate on the suction side around $x/c = 0.22$. However, no measurements have been carried out on the pressure side. In order to complete the reference data set, the solution obtained from the European computational aerodynamic research project named Parallax [91] is taken into account. In this work, the turbulent zone is solved with the $k - \varepsilon$/Chien RANS model [93] and the details about the solver are specified in [94]. Additionally, the transition is imposed in $x/c = 0.2$ on the suction side and in $x/c = 0.3$ on the pressure side. It is important to remind that this last transition location corresponds to the one obtained from the empirical data of the C13 configuration. It is, however, unlikely that the transition point remains unchanged with an angle of attack reduced by 10° and a Reynolds number increased by 10^6. Due to the drastic reduction in inclination, a transition further downstream would seem more physical. Nevertheless, in order to fit with this setup, the transition will be imposed in $x/c = 0.3$ on the pressure side. It is therefore important to take the results related to the lower side with care due to the lack of high-fidelity data.

First, the resulting averaged flow is illustrated in 6.18. The changes mainly occur on the suction side with an acceleration region until $x/c \simeq 0.1$ followed by a deceleration. The pressure side shows a narrow deceleration zone at the stagnation vicinity and then a hardly visible weak acceleration. Subsequently, the mean flow remains attached on both sides. Regarding the speed fluctuations, the Reynolds stress component $\langle u'u' \rangle$ is shown in Fig 6.19. It gradually grows on the suction side from the leading edge to the trailing edge. A similar behavior occurs on the pressure side but only from $x/c \simeq 0.6$ and with a much weaker amplitude. There is, however, no significant Reynolds stress rise translating a well defined turbulent transition on both sides, mainly due to the mesh coarseness.

Then, the velocity field in the x-direction after $22c/U_\infty$ and at the middle slice of the domain is shown in Fig 6.20. It reveals the existence of upstream oscillations, as observed in Sec 6.2.1 for the flow around a NACA0012. It is therefore necessary to keep that in mind regarding the sensor.

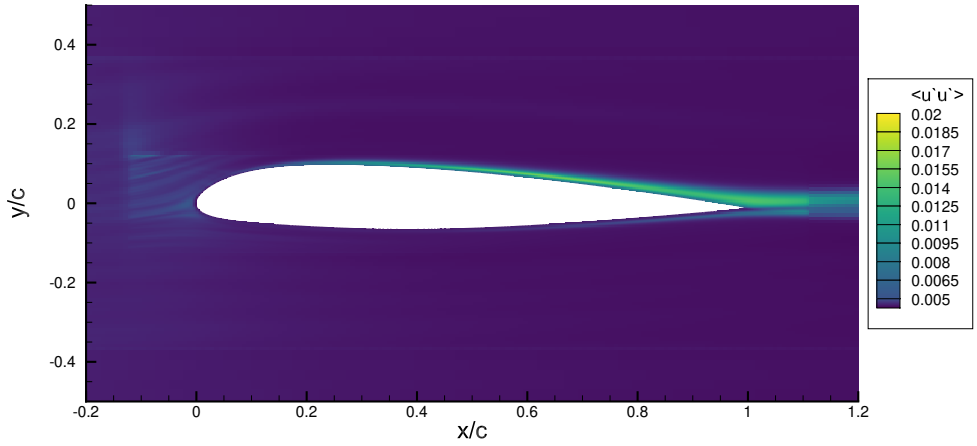

Figure 6.19: A-airfoil in C3 configuration: HWM with hard-coded transition. Reynolds stress component $\langle u'u' \rangle$ with u' the speed fluctuation in the x-direction.

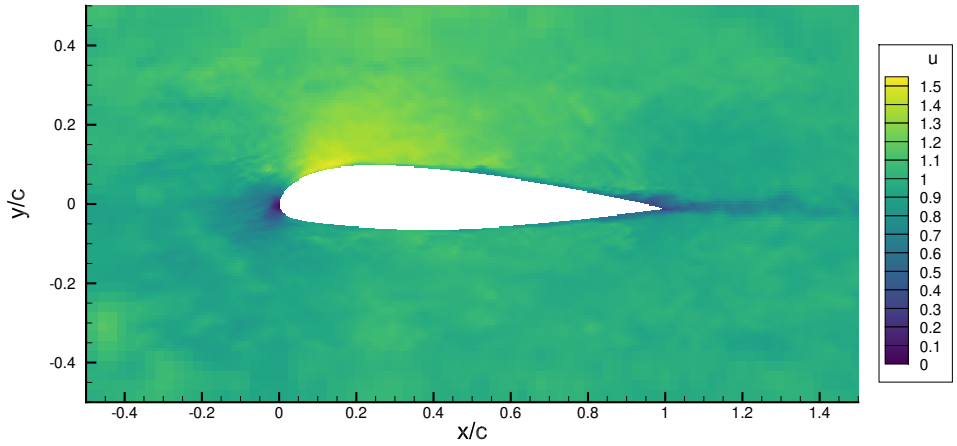

Figure 6.20: A-airfoil in C3 configuration: HWM with hard-coded transition. Instantaneous velocity field aligned with the x-direction, in $t = 22c/U_\infty$ and at the middle slice of the domain.

The analysis is now focused on the wall vicinity by comparing the pressure coefficient with respect to the empirical distribution in Fig 6.21a and 6.21b. It brings out an underestimation of the suction peak and the existence of wiggles in this same region. However, the offset with respect to the empirical data is of the order of $\Delta c_p \simeq 0.1$, which should lead to a slight underestimation of the inviscid speed computed by the LWM in this area. The rest of the suction side presents an offset attenuating towards the trailing edge. Regarding the pressure side, the stagnation point is positioned around $x/c \sim 0.0019$, i.e. slightly upstream of the empirical one located in $x/c \sim 0.003$. It is important to remind that the level-set function provided is computed with respect to this last location. Hence, the offset between both predictions introduces an error in the LWM. Then, a relatively good match is observed until $x/c = 0.3$, followed by a weak underestimation up to the trailing edge. Lastly, it is possible to observe the effect of the trailing edge cut, which implies a sudden drop in pressure around $x/c = 0.996$. Globally, the correspondence between the two distributions remains, nevertheless, acceptable taking the mesh resolution into account.

Afterwards, the wall-shear stress on the suction side is considered in Fig 6.21c and 6.21d and compared with friction from Parallax and the empirical data. Concerning the laminar part, the estimated friction matches relatively well with the one from Parallax until $x/c = 0.1$. Then, Parallax obtains a boundary layer tending towards separation around the transition location, whereas the self-similar model predicts a much weaker decrease in friction. On the other side, the turbulent part brings out an excellent agreement between the GWF, the $k - \varepsilon$/Chien model and the empirical data. Next, a similar comparison is achieved on the pressure side in Fig 6.21e and 6.21f. It reveals that the LWM shows an acceptable match with the solution obtained from Parallax, whereas the GWF predicts a higher friction in the turbulent part compared to the RANS model.

It is important to bear in mind that the comparison with Parallax is not to be taken as a rigorous validation. This project also introduces strong assumptions due to the RANS modeling and does not have the reliability of a high-fidelity solver or empirical data. On the other side, the results from the F1 tunnel enable to conclude that the HWM with hard-coded transition seems to give interesting results on the suction side despite the mesh resolution. It therefore seems relevant to go further by aiming to predict the transition with a sensor.

Considering the solution after $22c/U_\infty$ with a hard-coded transition, the related sensors are presented in Fig 6.22a and 6.22b, each with a given time factor τ and thus a given characteristic time of averaging $T = \tau \cdot c/U_\infty$. This reveals that for both faces, the time factor has a strong impact on the sensor distribution. In order to understand this, the related turbulent kinetic energy k/U_∞^2 and averaged skin friction from the GWF $\langle c_f \rangle$ are respectively represented in Fig 6.22c - 6.22d and in Fig 6.22e - 6.22f.

Starting with $\langle c_f \rangle$, the time factor τ only has an effect on the smoothness of the friction fields, but does not imply any significant numerical change. Conversely, the turbulent kinetic energy distributions reveal that the averaging time has to be sufficiently long in order to catch the mean flow and related fluctuations. If τ is too weak, the sensor is not able to correctly estimate the turbulent energy such that, considering a sensor threshold $s_{\mathrm{w,thr}}$ above 2, either no clear transition is predicted or one is detected but further downstream. Nevertheless, it is necessary to limit this parameter in order to avoid an excessive simulation time, as in practice the sensor distribution converges only after some multiples of T. Hence, given that the solution is considered in $t = 22c/U_\infty$, the maximum time factor has been limited to $\tau = 1$.

Due to the lack of high-fidelity data about the pressure side, the sensor analysis is now restricted to the suction side in Fig 6.22a. It enables to conclude that a time factor $\tau = 1$ combined with a threshold $s_{\mathrm{w,thr}} = 2$ seems to be suitable to obtain a transition around $x/c = 0.22$. It is important to mention that such a threshold is below the interval [2.5 ; 4] predicted by Bodart et al. [86]. This can be explained by the fact that the mesh related to WMLES is not able to capture all the turbulent scales and therefore leads to an underestimation of the turbulent kinetic energy. Thus, it seems consistent to impose a threshold slightly weaker to 2.5.

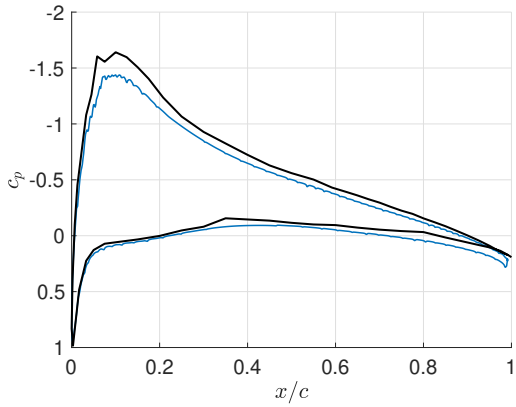

(a) Pressure coefficient.

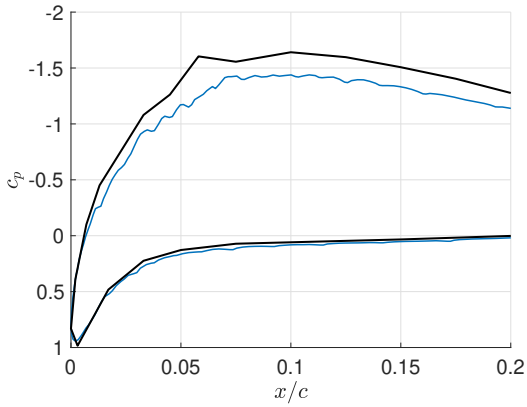

(b) Zoom of c_p in the laminar part.

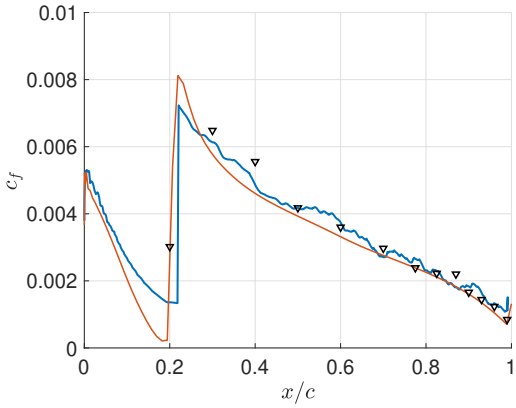

(c) Skin friction coefficient on the suct. side.

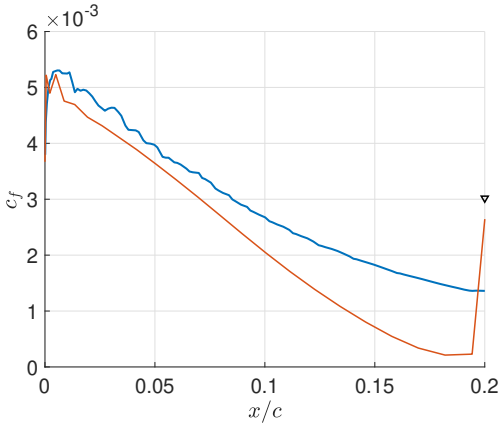

(d) Zoom of c_f in the laminar part on the suct. side.

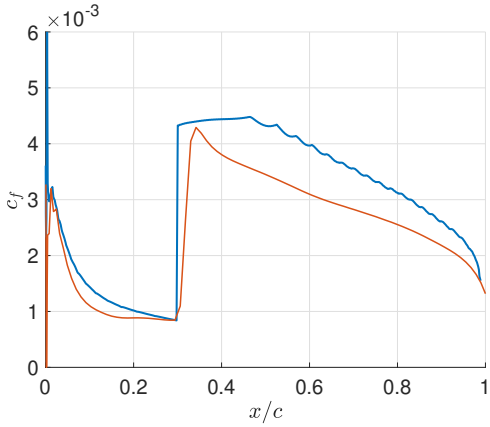

(e) Skin friction coefficient on the press. side.

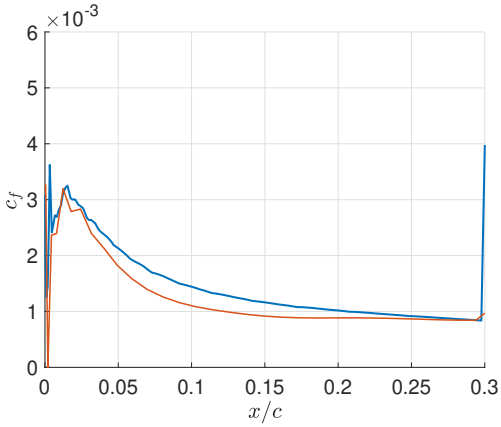

(f) Zoom of c_f in the laminar part on the press. side.

Figure 6.21: A-airfoil in C3 configuration. Skin friction and pressure related to the HWM with hard-coded transition (blue line), to Parallax using the $k-\varepsilon$/Chien RANS model in the turbulent regions [91] (orange line) and to the F1 tunnel [91] (black line and black triangles).

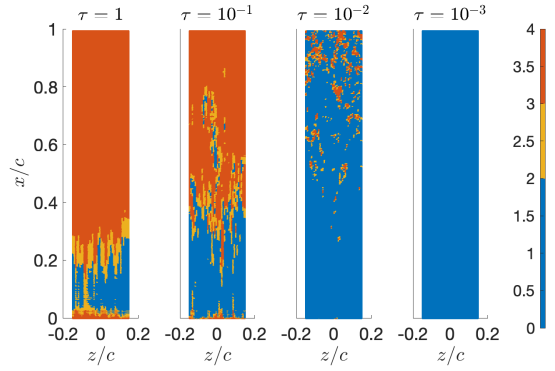

(a) Sensor s_w on the suct. side.

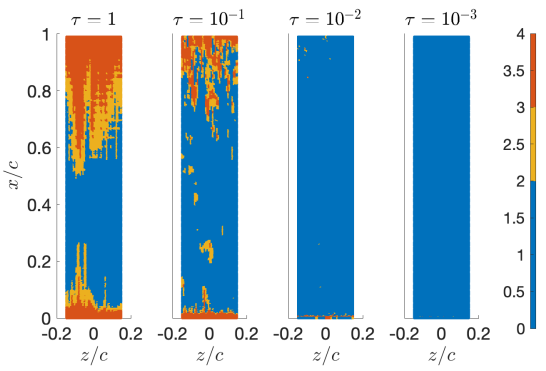

(b) Sensor s_w on the press. side.

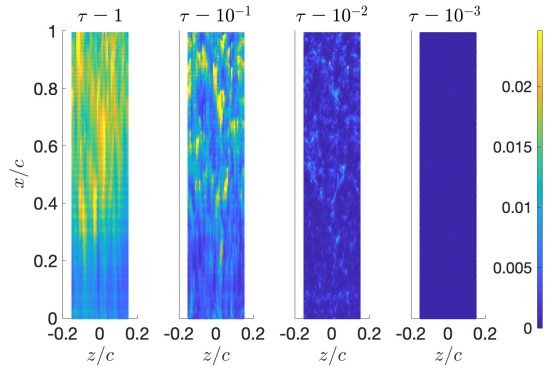

(c) k/U_∞^2 on the suc. side.

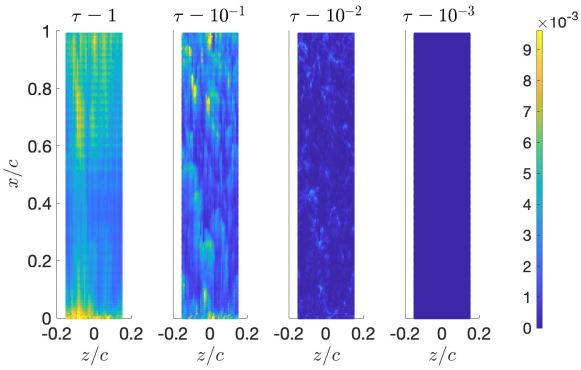

(d) k/U_∞^2 on the press. side.

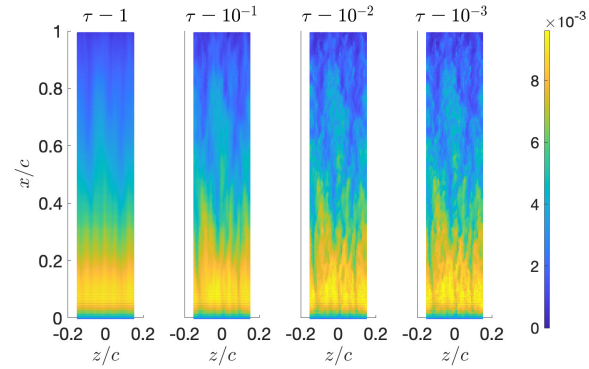

(e) $\langle c_f \rangle$ on the suct. side.

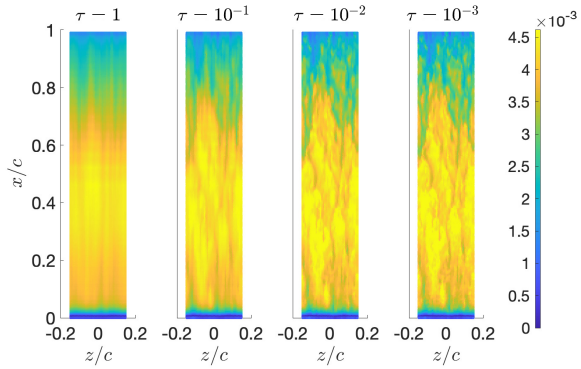

(f) $\langle c_f \rangle$ on the press. side.

Figure 6.22: A-airfoil in C3 configuration: HWM with hard-coded transition. Sensor distribution s_w, turbulent kinetic energy k/U_∞^2 and averaged skin friction coefficient from the GWF $\langle c_f \rangle$ in $t = 22c/U_\infty$ for different time factors τ.

6.3.2 C3 Configuration: Transition Detection

Relying on the sensor study in Sec 6.3.1, the HWM with transition detection is now applied by imposing a time factor τ and a threshold $s_{\mathrm{w,thr}}$ as

$$\tau = 1 \qquad \text{and} \qquad s_{\mathrm{w,thr}} = 2.$$

The resulting pressure distribution is first shown in Fig 6.23a and 6.23b. It brings out that the activation of the sensor does not lead to significant changes with respect to the hard-coded case. Both distributions present an underestimation of the suction peak, only slightly more pronounced with the transition detection. Regarding the pressure side, the difference between the two cases is hardly visible and the two stagnation points are located in $x/c \simeq 0.0019$.

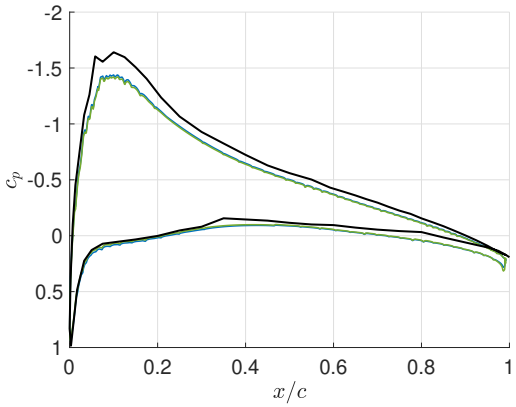

(a) Pressure coefficient.

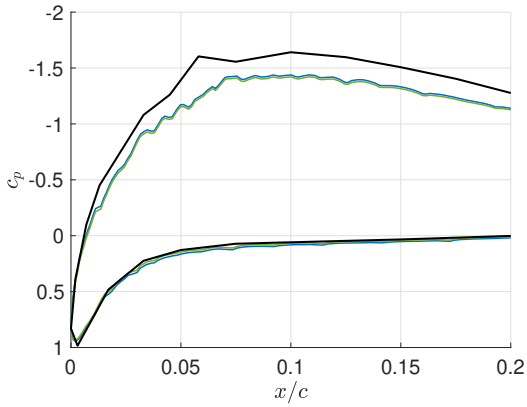

(b) Zoom of c_p in the laminar part.

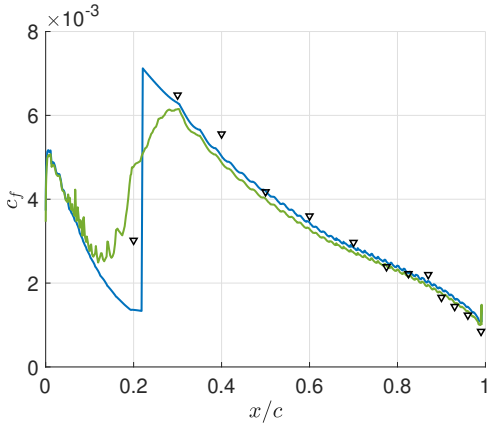

(c) Skin friction coefficient on the suct. side.

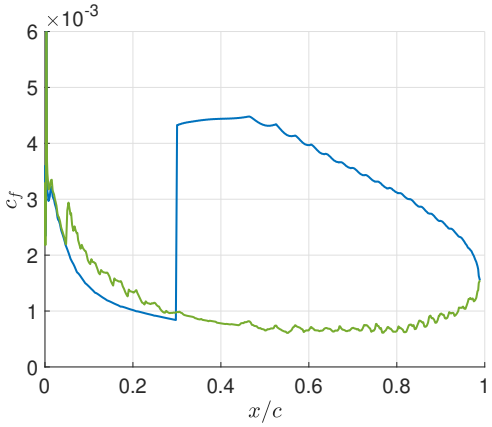

(d) Skin friction coefficient on the press. side.

Figure 6.23: A-airfoil in C3 configuration. Skin friction and pressure related to the HWM with transition detection (green line), to the HWM with hard-coded transition (blue line) and to the F1 tunnel [91] (black line and black triangles).

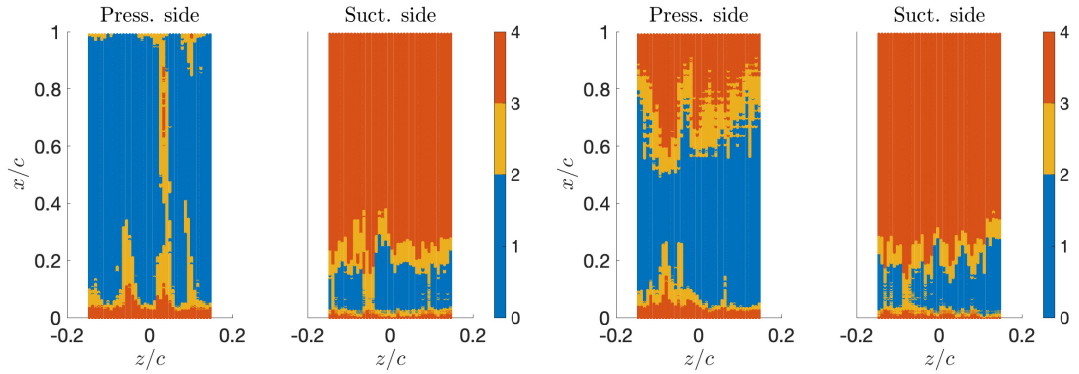

(a) HWM with transition detection.

(b) HWM with hard-coded transition.

Figure 6.24: A-airfoil in C3 configuration. Sensor distribution in $t = 22c/U_\infty$ and with $\tau = 1$.

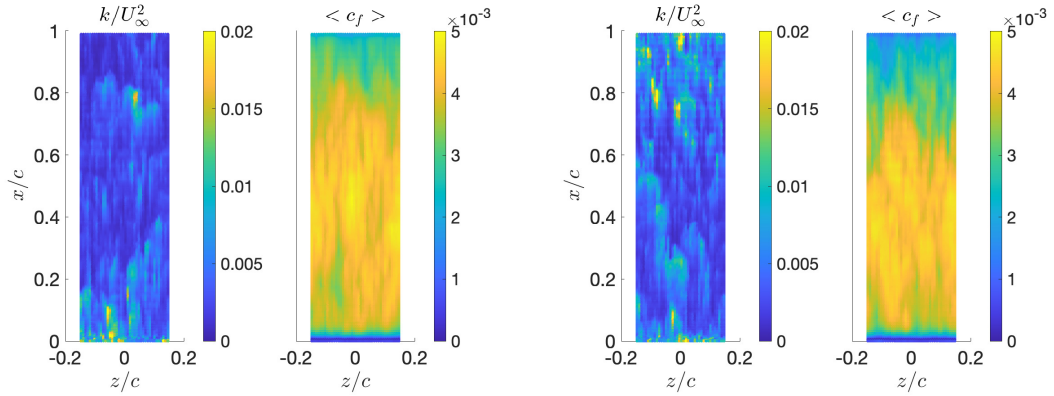

(a) HWM with transition detection.

(b) HWM with hard-coded transition.

Figure 6.25: A-airfoil in C3 configuration. Turbulent kinetic energy k/U_∞^2 and averaged skin friction coefficient from the GWF $\langle c_f \rangle$ on the pressure side in $t = 22c/U_\infty$ and with $\tau = 1$.

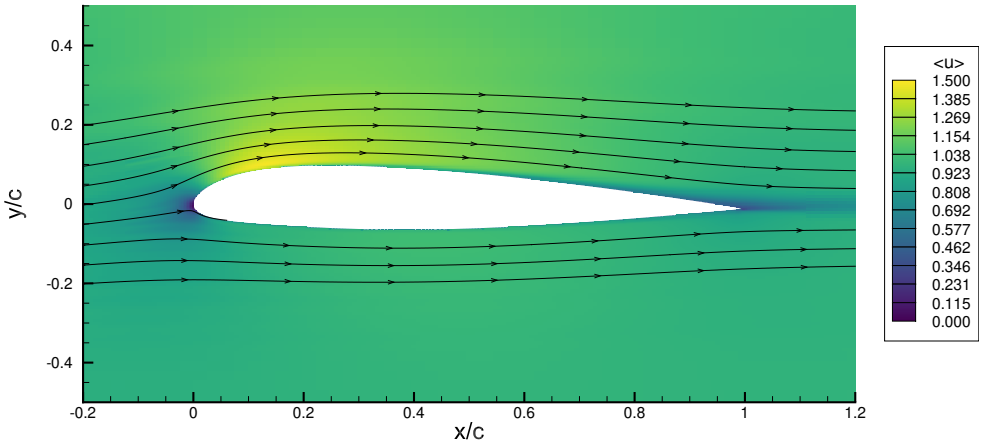

(a) HWM with transition detection.

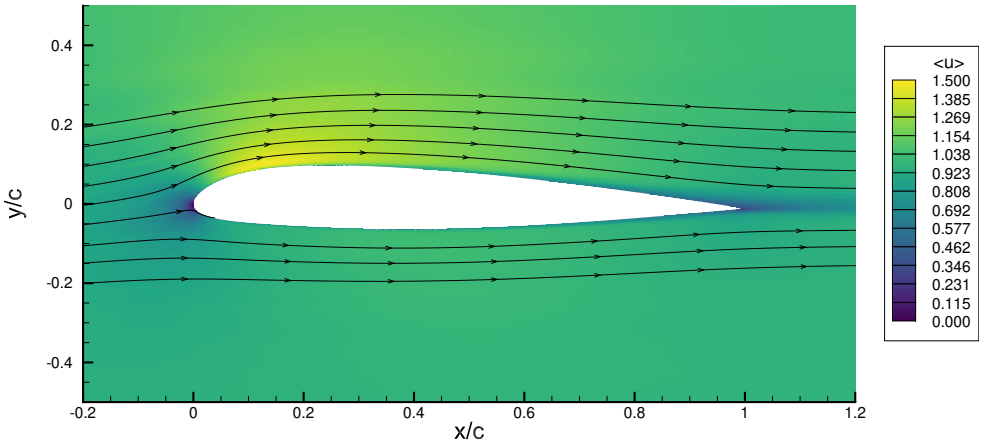

(b) HWM with hard-coded transition.

Figure 6.26: A-airfoil in C3 configuration. Averaged velocity field $\langle u \rangle$ aligned with the x-direction and illustrated with streamlines (black lines).

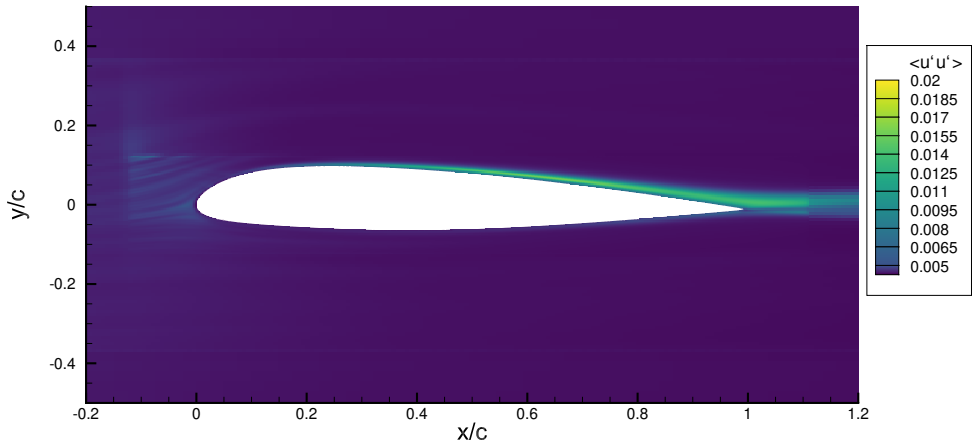

(a) HWM with transition detection.

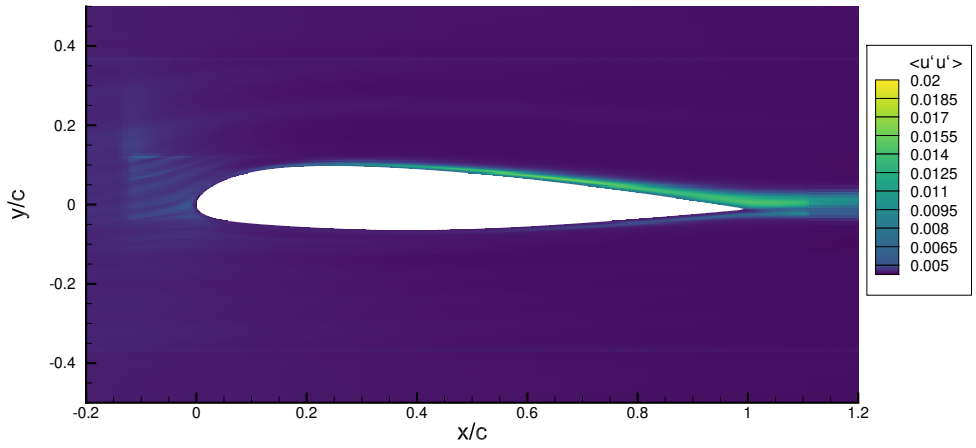

(b) HWM with hard-coded transition.

Figure 6.27: A-airfoil in C3 configuration. Reynolds stress component $\langle u'u' \rangle$ with u' the speed fluctuation in the x-direction.

Afterwards, Fig 6.23c reveals that the HWM with transition detection provides interesting results on the suction side in terms of friction coefficient. The use of the sensor leads to a transition region located around $x/c \simeq 0.22$, which is in line with the experiment. Upstream, the results match relatively well with the prediction from the LWM. Concerning the turbulent part, a good correspondence is observed with the GWF and the empirical data from $x/c \simeq 0.3$. Subsequently, the sensor distribution on the suction side after $22c/U_\infty$, see Fig 6.24a, is strongly similar to the one obtained with hard-coded transition in Fig 6.24b. Thus, the activation of the sensor, in this case, does not imply any significant change in sensor distribution compared to hard-coding transition.

An analogous analysis is achieved on the pressure side. Beginning with the friction, Fig 6.23d does not show any well defined transition. The related sensor distribution in Fig 6.24a presents some turbulent fringes across the domain but no clear turbulent region. There is therefore a complete change of physics compared to the hard-coded case in Fig 6.24b. To understand this, the turbulent kinetic energy k/U_∞^2 and the averaged friction from the GWF $\langle c_f \rangle$, both over the pressure side, are illustrated in Fig 6.25 for the two transition approaches. It reveals that the hard-coding method implies a significant increase in turbulent kinetic energy downstream, whereas both friction distributions remain similar. The most likely cause of such a higher energy zone is the change of wall model imposed in $x/c = 0.3$: the resulting wall-shear stress discontinuity

implies flow fluctuations and thus triggers a turbulent area downstream. As specified previously, the transition location has been imposed only to align with the Parallax project settings [91] and cannot be taken as a high-fidelity reference. It is therefore preferable not to consider the sensor on the pressure side related to the hard-coded transition.

Regarding the pressure side with transition detection, despite the lack of reference data, such a fully laminar prediction seems puzzling due to the considered flow conditions. One plausible explanation is the mesh resolution which is not sufficiently fine to capture enough turbulent frames on this side. This statement could be refuted by the fact that the resolution is fine enough to predict a turbulent transition on the suction side, but it is important to remind a fundamental difference between these two faces: conversely to the pressure side, the suction side presents an adverse pressure gradient favoring the transition [95] and thus leading to more developed turbulent structures, and tending to increase the boundary-layer thickness [96]. It therefore seems that the required mesh resolution to predict a turbulent transition must be finer on the pressure side than on the suction side. This discussion is, nevertheless, limited due to the lack of high-fidelity data.

Finally, in order to get a more global perspective, the averaged velocity fields, respectively obtained using the HWM with transition detection and with hard-coded transition, are shown in Fig 6.26. This enables to conclude that the sensor activation does not introduce any significant change in mean flow. It is indeed hard to distinguish a difference between the two statistics in the broad sense of the term.

A similar comparison is then achieved with respect to the Reynolds stress component $\langle u'u' \rangle$ in Fig 6.27. Beginning with the suction side, it is once again possible to claim that the sensor activation does not introduce any major modification. Nevertheless, one can notice a change on the pressure side. Compared to the hard-coded transition, the use of the sensor leads to weaker Reynolds stress values from $x/c \sim 0.6$. This observation is in line with the discussion about the sensor distributions and the effect of the hard-coding transition method.

6.3.3 C3 Configuration: HWM Capabilities

To sum up the analysis of the C3 configuration, the friction from the HWM with hard-coded transition shows a good match with the experiment regarding the suction side. Due to the lack of empirical data on the pressure side, no relevant conclusion can be drawn for this face. Additionally, an acceptable correspondence with the friction from the RANS solver is observed, except in the turbulent region on the pressure side where the GWF leads to a higher wall-shear stress. It is important to keep in mind that this second comparison does not constitute a reliable validation due to the simplifications introduced by the RANS modeling. It would be interesting to extend this study by completing the reference data set and imposing a more reliable transition point estimate on the pressure side.

Regarding the sensor related to the HWM with hard-coded transition, its analysis with respect to the time factor τ enables to understand the effect of the characteristic time of averaging $T = \tau \cdot c/U_\infty$. This latter simply has to be large enough in order to correctly capture the flow fluctuations with respect to the mean solution. It is, nonetheless, necessary to limit it in order to obtain a converged solution in an acceptable computational time. Finally, the sensor distribution over the suction side reveals that imposing $\tau = 1$ and $s_{\mathrm{w,thr}} = 2$ enables to fit with the empirical transition location.

It is on the basis of this last conclusion that both sensor parameters are frozen in order to automatically determine the flow regime. For such values, the HWM with transition detection enables to predict a turbulent transition on the suction side matching relatively well with the one from the experiment. Regarding the pressure side, no clear transition is predicted, while the sensor related to the hard-coded case shows a clear turbulent region. This highlights one potential effect of the discontinuity imposed in the friction field, which can lead to a change of physics from hard coding to the use of the sensor. In addition, given the considered flow conditions, the absence of transition on the pressure side seems surprising. One plausible explanation is that the mesh resolution is not fine enough to predict a turbulent region on the pressure side but apparently sufficient regarding the suction side and this, due to the adverse pressure gradient leading to more developed turbulent structures and a larger boundary layer.

It is thus possible to conclude that the HWM, with or without transition detection, presents a good match with respect to the empirical data on the suction side and seems promising in both cases. Regarding the sensor, it would nevertheless be important to question and assess its robustness with respect to the sensor threshold for different test cases and mesh resolutions.

6.3.4 C13 Configuration: Hard-Coded Transition

The C13 configuration stands for an interesting limit case. Relying on the measurement from the F1 wind tunnel [91], this setup is located close to the maximum lift point in 15.1°. Numerous studies about this particular case are available in the literature. A deep investigation was carried out by Davidson et al. in the context of Project LESFOIL [97]. More recently, Tamaki et al. [98] conducted both wall-modeled (WM-) and wall-resolved (WR-) large eddy simulations (LES). The resulting WRLES skin friction on the suction side will be taken as a reference in the rest of this study.

The empirical data [91] enables to consider the transition points as known *a priori*: $x/c = 0.12$ on the suction side and $x/c = 0.3$ on the pressure side. It is therefore possible, in the first instance, to apply the HWM with hard-coded transition. As a starting point, the resulting averaged flow is shown in Fig 6.28. The velocity field reveals that the flow remains attached in the averaged sense. The negative values at the stagnation point vicinity only translate the change of flow direction towards the suction side. In terms of fluctuations, Fig 6.29 underlines a high Reynolds stress region on the suction side reaching a maximum around $x/c \sim 0.4$. In contrast, the pressure side does not seem to present significant fluctuations compared to Reynolds stress values on the upper side.

For such an inclination, it seems puzzling not to detect any separation region within the mean flow on the suction side. In order to investigate that, the wall-shear stress distribution from the HWM and the state of the flow, either attached or separated, are both illustrated in $t = 17c/U_\infty$ in Fig 6.30. Note that the separation is simply detected from the velocity field interpolated in $x_n = 1 \cdot \min(\Delta_x, \Delta_y, \Delta_z)$. This brings out that the friction significantly drops from the transition until reaching some separation spots near the trailing edge. The latter are, nevertheless, erased during the averaging process. It is thus legitimate to question the mesh resolution. However, in order to keep an acceptable computational cost, the rest of this study will be carried out with the current grid resolution.

The analysis is then re-centered at the wall vicinity by considering the pressure distribution in Fig 6.31a and 6.31b. Regarding the pressure side, the solution corresponds relatively well with the empirical data. On the other side, the comparison reveals an important underestimation of the suction peak of about $\Delta c_p = 1$. It is therefore important to keep in mind that such an error leads to an underestimation of the external flow velocity computed by the LWM. Finally, the stagnation point is located in $x/c = 0.0261$, whereas the measurements from the F1 wind tunnel predict $x/c = 0.03$. As underlined for the previous C3 setup, the offset between these two estimates has consequences on the LWM through the level-set function provided with respect to the empirical point.

Afterwards, the obtained wall-shear stress on the suction side is compared to the empirical data and to the WRLES friction in Fig 6.31c. The wall-shear stress from the WRLES first shows a laminar separation bubble followed by a turbulent reattachment. By contrast, the LWM is not able to predict flow separation, which is a direct consequence of the self-similarity assumption implying a fully attached boundary layer. This results in a strong overestimation of friction in the laminar region. Then, the transition jump is underestimated by the GWF compared to the two reference solutions and the friction remains undervalued until $x/c \sim 0.7$. One plausible explanation is the difference in physics upstream: the absence of laminar separation could explain the underestimation of the turbulent friction peak. Subsequently, both WRLES and empirical data reveal a flow separation close to the trailing edge, whereas the HWM predicts a fully attached flow in the averaged sense. Such a prediction is in line with the turbulent wall-shear stress underestimation upstream: the skin friction accumulation is not sufficient to trigger a flow separation in the mean solution, but only some separation spots distributed in the spanwise direction, as previously illustrated with the instantaneous solution in Fig 6.30.

Concerning the pressure side in Fig 6.31d, due to the absence of reference data, no conclusion can be drawn about the validity of the results. Nevertheless, this case enables to illustrate the consequence of the stagnation point hard-coding during the pre-processing: the laminar skin friction curve presents a discontinuity in $x/c \sim 0.031$, which corresponds to the empirical stagnation point imposed during the level-set function computation. In addition to this discontinuity, the use of a level-set function defined with respect to a stagnation point downstream of the actual one implies a lower FS wall-shear stress through the entire laminar part on the suction side and to a larger one on most of the pressure side since $\tau_{w,FS} \sim \sqrt{1/x_s}$. In order to avoid this, it would be relevant to improve the LWM in such a way that the stagnation points are directly detected from the velocity field and not considered as known *a priori*.

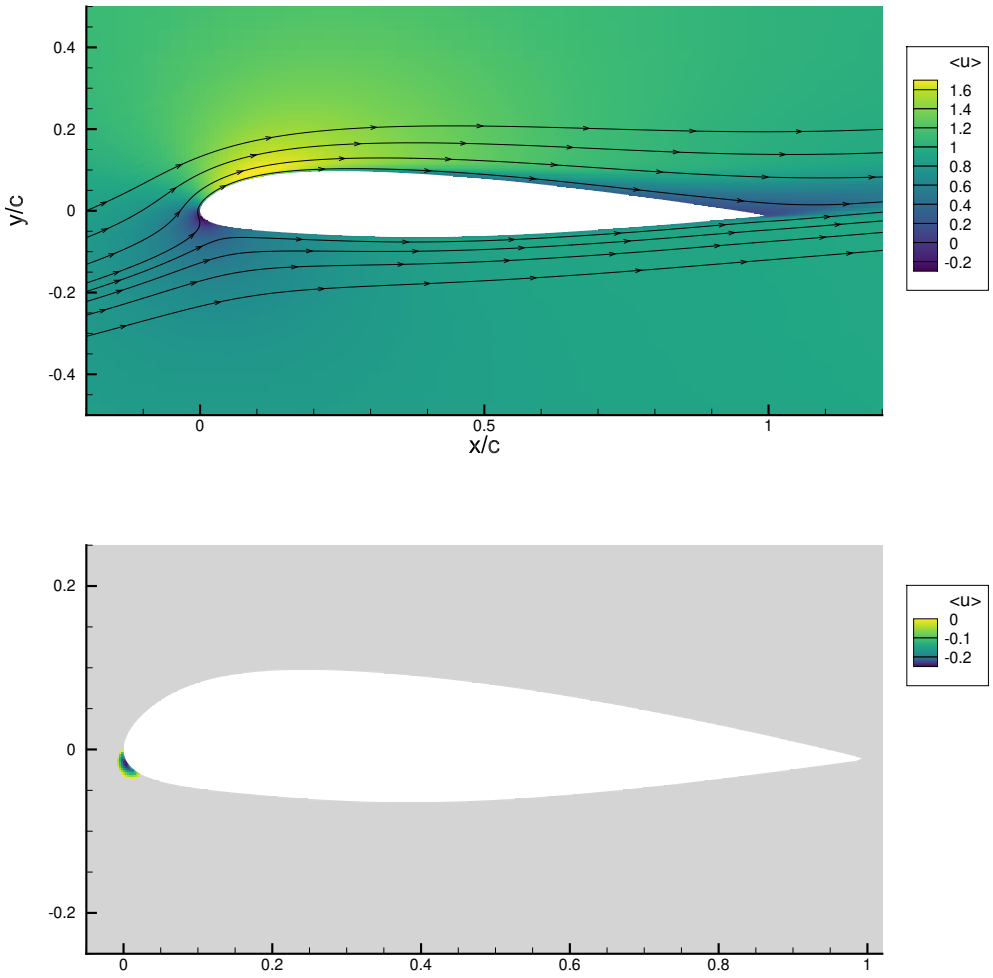

(a) Averaged velocity field $\langle u \rangle$ aligned with the x-direction.

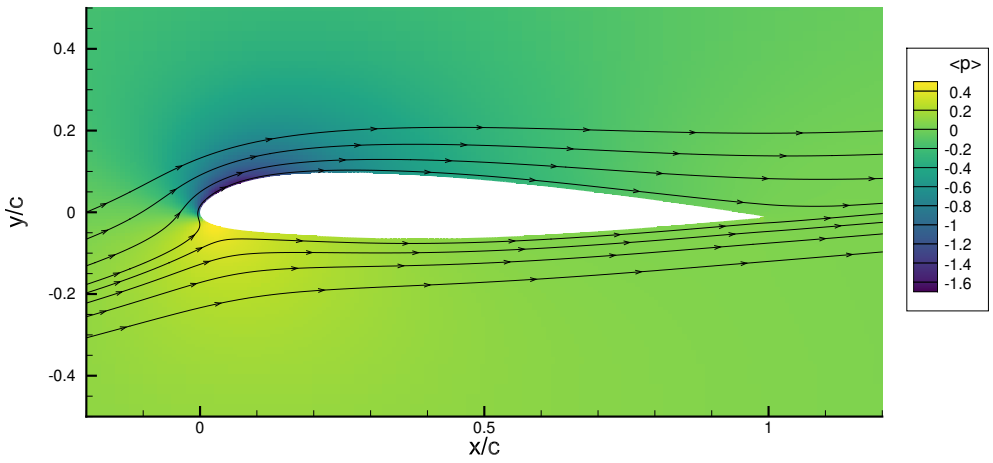

(b) Averaged pressure field $\langle p \rangle$.

Figure 6.28: A-airfoil in C13 configuration: HWM with hard-coded transition. Averaged solution illustrated with streamlines (black lines).

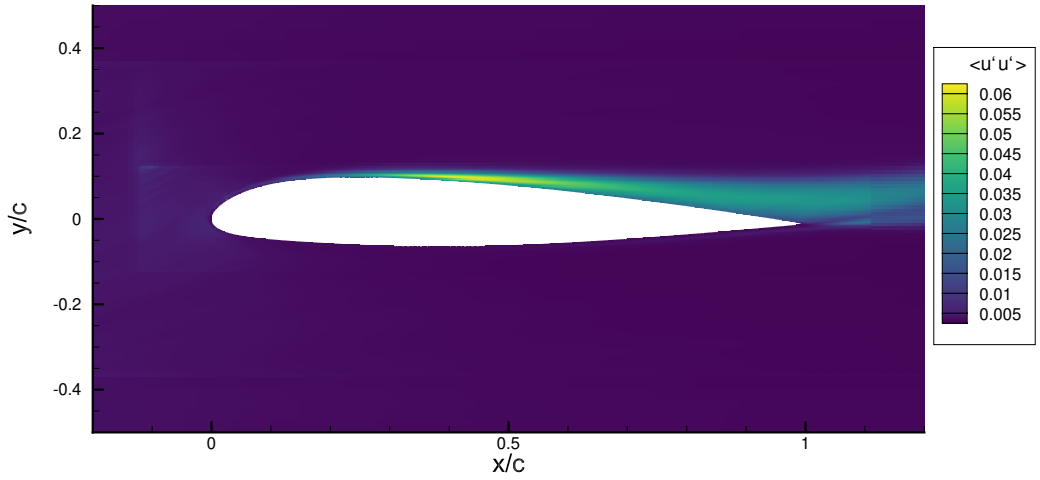

Figure 6.29: A-airfoil in C13 configuration: HWM with hard-coded transition. Reynolds stress component $\langle u'u' \rangle$ with u' the speed fluctuation in the x-direction.

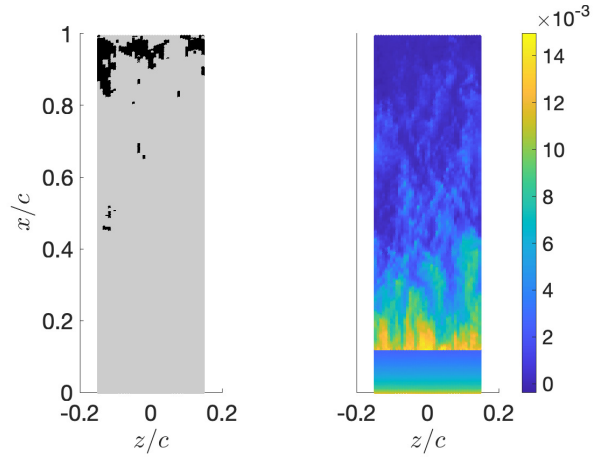

Figure 6.30: A-airfoil in C13 configuration: HWM with hard-coded transition. Separation points (left side; black points) and instantaneous skin friction coefficient distribution from the HWM (right side) on the suction side in $t = 17c/U_\infty$.

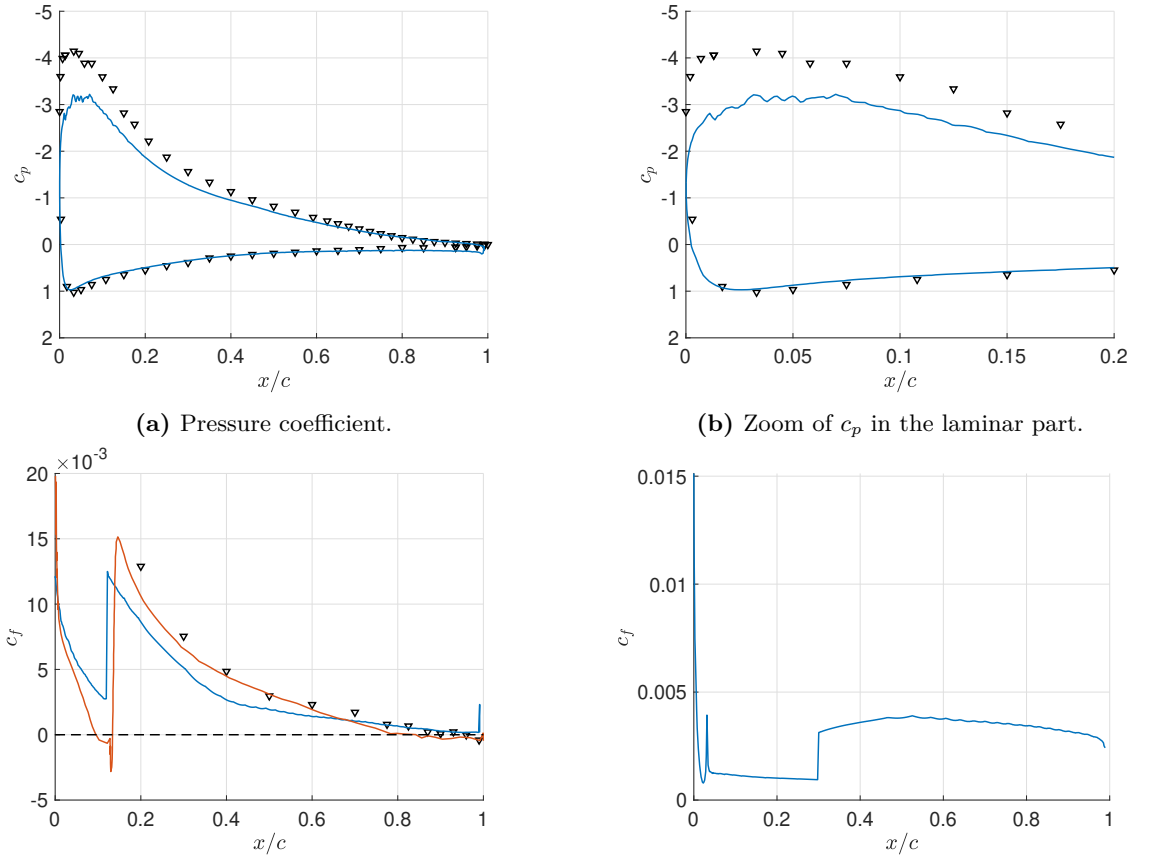

(a) Pressure coefficient.

(b) Zoom of c_p in the laminar part.

(c) Skin friction coefficient on the suct. side.

(d) Skin friction coefficient on the press. side.

Figure 6.31: A-airfoil in C13 configuration. Skin friction and pressure related to the HWM with hard-coded transition (blue line), to the WRLES [98] (orange line) and to the F1 tunnel [91] (black line and black triangles).

6.3.5 C13 Configuration: Transition Detection

In a second step, the model with transition detection is applied to the C13 configuration. For the sake of generality, the same sensor parameters as imposed in Sec 6.3.2 are used, i.e. $\tau = 1$ and $s_{\mathrm{w,thr}} = 2$. The resulting pressure and friction distribution are then compared with the hard-coded case and the reference data in Fig 6.32.

Beginning with the pressure distribution in Fig 6.32a and 6.32b, it is possible to conclude that the sensor activation does not imply any significant change but only a slightly more pronounced underestimation of the suction peak. Then, Fig 6.32c shows that the skin friction in the laminar part of the suction side is now much higher compared to the LWM and the WRLES reference solution. The related sensor in Fig 6.33a reveals that there is no well-defined laminar region with such an imposed threshold, but only some laminar fringes, as observed with the sensor related to the hard-coded case in Fig 6.33b. In order to obtain a better correspondence with the empirical transition in $x/c = 0.12$, it would be more suitable to impose a threshold $s_{\mathrm{w,thr}}$ closer to 3.

Such a difference in the threshold requirement between the C3 and C13 configurations highlights a lack of robustness of the HWM with regard to this parameter. This seems, nevertheless, logical reminding the fact that both cases have the same grid resolution. In fact, despite a lower Reynolds number, the C13 configuration is expected to present more developed and larger turbulent structures due to the much higher inclination. Consequently, with the given mesh size, it seems logical to obtain higher sensor values through the entire surface for the C13 case. It would be interesting to extend this discussion by studying the sensor for different flow conditions and meshes in order to propose a threshold value $s_{\mathrm{w,thr}}$ for a given range of

Reynolds numbers, inclination angles and grid sizes.

Finally, from Fig 6.32d, it is possible to observe a complete change in friction distribution from that obtained with the hard-coded transition. As shown in Fig 6.33a, the sensor predicts a fully turbulent flow in the laminar part and important laminar fringes in the turbulent region. A similar sensor distribution is observed with the hard-coded configuration in Fig 6.33b, which enables to state that the absence of laminar region is not due to the sensor activation. It would be necessary to carry out a mesh study in order to verify if the physics is correctly captured and analyze the evolution of the turbulent kinetic energy distribution.

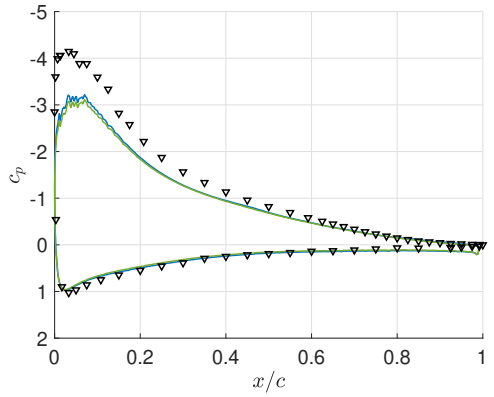

(a) Pressure coefficient.

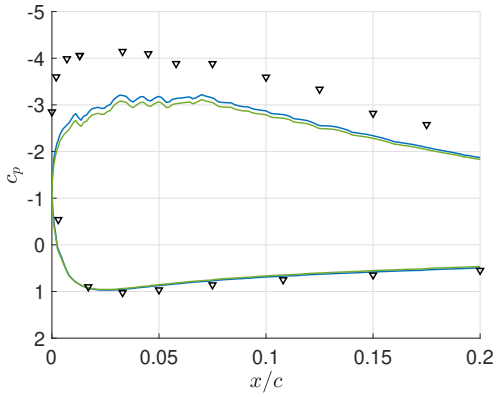

(b) Zoom of c_p in the laminar part.

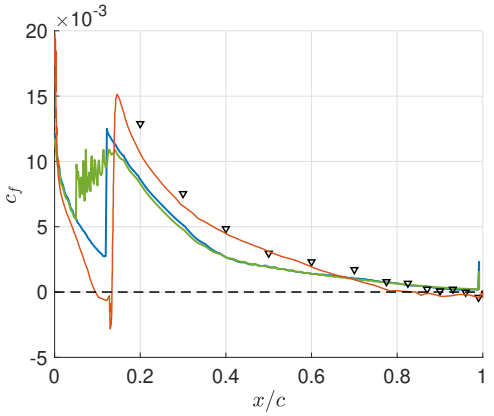

(c) Skin friction coefficient on the suct. side.

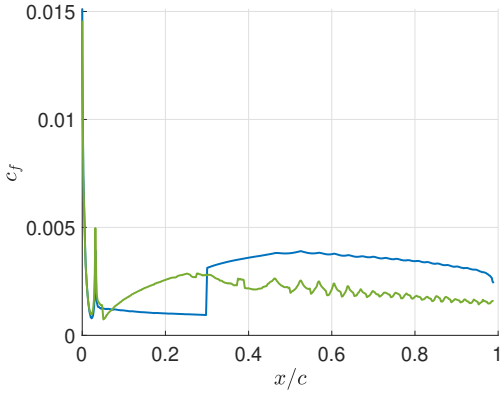

(d) Skin friction coefficient on the press. side.

Figure 6.32: A-airfoil in C13 configuration. Skin friction and pressure related to the HWM with transition detection (green line), to the HWM with hard-coded transition (blue line), to the WRLES [98] (orange line) and to the F1 tunnel [91] (black line and black triangles).

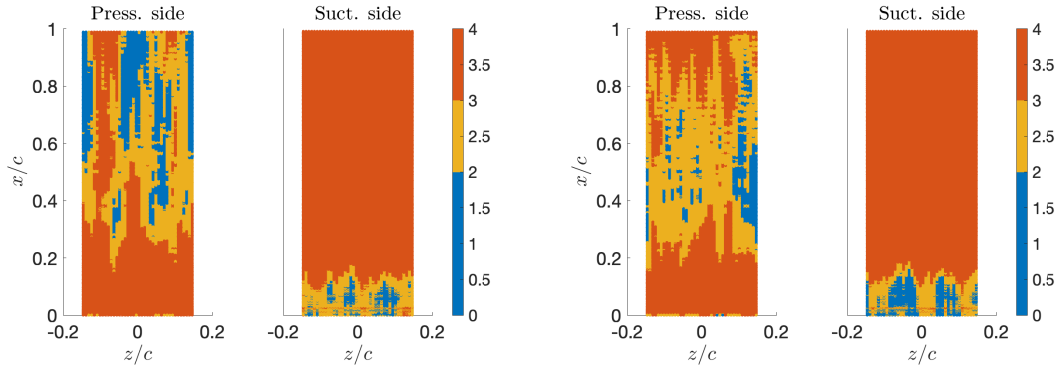

(a) HWM with transition detection.

(b) HWM with hard-coded transition.

Figure 6.33: A-airfoil in C13 configuration. Sensor distribution in $t = 17c/U_\infty$ and with $\tau = 1$.

6.3.6 C13 Configuration: HWM Limitations

The C13 configuration highlights some HWM limitations. Starting with the laminar part, the LWM is not able to predict the laminar separation bubble observed from the WRLES solution, which seems to impact the entire skin friction distribution. Regardless of the resolution, this wall model is not able to estimate such a physics given that the modeling is based on the Falkner-Skan equation assuming a 2D, steady, fully attached, self-similar boundary layer. This prompts to look for future investigations to overcome that. One possibility is to switch from the Falkner-Skan estimate to a linear approximation as soon as a flow separation is detected. Since the scales in a separated region are generally larger than the ones related to a fully attached boundary layer, the linear approximation should be an acceptable wall-shear stress estimate.

Additionally, the impact of the stagnation point hard-coding during the pre-processing is highlighted with the skin friction distribution on the pressure side. The mismatch between the provided stagnation point used by reinitialization process and the actual one leads to a discontinuity in the friction curve. More globally, it affects the Falkner-Skan wall-shear stress estimate on both faces since $\tau_{w,FS} \sim \sqrt{1/x_s}$. A straightforward solution would be to determine the stagnation points directly from the velocity field and recompute the level-set function accordingly.

Finally, the analysis of the sensor reveals a case dependence with respect to the threshold value $s_{\mathrm{w,thr}}$. In order to obtain a well defined laminar region on the suction side in line with the experiment, it would be necessary to impose a larger threshold compared to the C3 configuration. Physically, such a conclusion is not surprising considering the fact that in both cases, the mesh resolution is the same: increasing the inclination of 10°, despite a Reynolds number decreased by 10^6, is expected to lead to a greater turbulent activity and thus to a larger range of turbulent structures captured by the grid. In order to get a better understanding, it would be relevant to study the effect of the angle of attack, Reynolds number and mesh resolution on the sensor distribution and on the required threshold enabling an acceptable match with respect to the corresponding reference transition location.

Chapter 7

Conclusion

In the context of the wall-stress modeling for LES, this work proposes a hybrid wall model (HWM) for laminar, transitional and fully turbulent flows. Proceeding step by step, a laminar wall model (LWM) is first developed by assuming a self-similar boundary layer. To that end, a shooting process and an ODEs solver are implemented to solve the Falkner-Skan (FS) equation and to obtain the shooting angle α involved in the wall-shear stress computation. Both implementations are verified by considering different cases from the literature. This assessment demonstrates the accuracy and the robustness of the codes. At this stage, it is thus possible to estimate the wall-shear stress providing the FS constants and the external flow velocity U_e. Regarding this latter, an expression with respect to the static pressure is derived from Bernoulli's equation for a straight wall and for an aerodynamic profile. The main motivation is to obtain a good robustness in relation to the height of extraction h_w, which is not possible by estimating U_e directly from the velocity field. Hence, by extracting the static pressure at the wall vicinity, the LWM is able to return an estimate of the wall-shear stress.

For verification, the LWM is applied to laminar flows over a straight wall: a flow over a flat plate and the Hiemenz flow. In both cases, a convergence study of the friction as a function of the mesh resolution in the wall-normal direction is carried out for the LWM, a turbulent wall model using the log-law and the wall-resolved approach. On the one hand, the study of the flat plate demonstrates the potential of the LWM with respect to the two other cases regarding the accuracy of the friction estimate for coarse meshes, but this, only far from the leading edge. Near this location, the LWM leads to an underestimation of the friction compared to the wall-resolved (WR) reference solution. Such an error implies a significant undervaluation of both the displacement and the momentum thickness in the whole domain, mainly implied by the overestimation of the tangential velocity at the first grid points off the wall. To overcome this, the wall model is modified in such a way that the Neumann boundary condition corresponds to the maximum between the Falkner-Skan estimate and the linear approximation of the friction using the tangential velocity at the first grid point. With such a procedure, the Neumann boundary condition is provided by the linear approximation in most of the leading edge vicinity, resulting in a much better match in terms of friction, velocity profile and boundary layer thickness with respect to the WR reference solution and this, in the whole domain. Although simple, this setup thereby highlights the importance of verifying the validity of the self-similarity assumption throughout the entire domain for both local and global solution accuracy.

On the other hand, the convergence study for the Hiemenz flow also demonstrates the accuracy of the LWM. In addition, it highlights the benefit of feeding the LWM with the pressure field. Although the extraction is achieved at the second point off the wall for all resolutions, the friction obtained from the LWM converges towards the one computed from the WR reference solution. Obviously, this would not have been the case with a model using the velocity field to estimate the external flow velocity. Such a case would have required a succession of trials and errors to find the right height of extraction.

Afterwards, the aim is to extend the applicability of the LWM to curved surfaces defined by triangular meshes. To do this, it is necessary to be able to compute the shortest distance from the stagnation points on such irregular grids, which is, however, not trivial. To overcome that, a method, initially used to compute the signed distance function with respect to an interface defined on a Cartesian grid [59], is adapted to provide such a distance, named level-set function Φ in this work. The first challenge is to compute the

level-set function gradient at each vertex defining the triangular mesh. To that end, the average gradient on star (AGS) method [80] is implemented and a first version of the reinitialization process 3 is proposed. This latter turns out to be highly accurate in the case of a flat plate with a single stagnation line on one of its edges. Nevertheless, the process leads to discontinuities in the case of distance fields presenting local maxima or ridges. In response to this, an improved version is developed, leading to algorithm 4. This algorithm is applied to a flat plate presenting two stagnation lines respectively placed on two opposite edges. Such a configuration highlights the significant improvement brought by this last version compared to the initial one.

Then, in order to assess the robustness of algorithm 4, convergence studies are carried out on the flat plate with two stagnation lines, a cylinder with an axis-parallel stagnation line and a sphere presenting a stagnation point. On the one hand, the analysis reveals a monotonic convergence for the flat plate and the cylinder in terms of mean error and error on the absolute maximum of Φ. On the other hand, the case of the sphere brings to light the importance of the mesh quality with regard to the accuracy of the resulting level-set function: if the refinement process is carried out solely by increasing the number of vertices without concern for the mesh quality, a slight increase in mean relative error can be observed. It would therefore be relevant to examine this in a deeper way by rigorously analyzing the characteristics of the meshes under consideration (such as the triangle elongation, the number of obtuse angles,...) to determine the relevant mesh properties related to this notion of quality. Lastly, the process is applied to a cube presenting a stagnation point at one of its vertices. This example demonstrates the robustness of the process in relation to the abrupt changes in surface direction encountered at each edge of the body. Overall, the analysis reveals that the accuracy and the smoothness of the level-set functions obtained from algorithm 4 seems to be sufficiently good considering that the latter are intended to be used by a wall model.

The last part of this work consists in modeling a transitional flow over an extruded wing. For this purpose, a hybrid wall model (HWM) is built by combining the LWM and a turbulent wall model based on the general wall function (GWF) [85] simplified by neglecting the effect of the pressure gradient. In the first instance, the transition location is hard-coded such that the LWM is applied upstream and the GWF downstream. Then, a sensor measuring the turbulent kinetic energy in viscous units is implemented in order to automatically determine the local type of regime and apply the wall treatment accordingly. Its two main parameters are the time factor τ, determining the characteristic averaging time $T = \tau \cdot c/U_\infty$, and the sensor threshold $s_{\mathrm{w,thr}}$ above which the flow is considered as turbulent. Such a process is applied to three configurations: the NACA0012 with ($Re = 10.25 \cdot 10^6$; AoA $= 0°$) and the A-airfoil with the flow conditions ($Re = 3.1 \cdot 10^6$; AoA $= 3.4°$) and ($Re = 2.1 \cdot 10^6$; AoA $= 13.3°$), respectively denoted as C3 and C13. Note that in all cases, the considered meshes are much coarser compared to traditional LES grids.

The study of the NACA0012 with hard-coded transition first enables to understand the effect of the mesh resolution by considering a coarse and a fine grid. One finds that the mesh refinement mainly implies a major improvement of the friction predicted from the GWF, while no significant change is observed in the laminar part. Globally, the friction and the pressure distribution obtained on the fine mesh matches well with the empirical reference data, which constitutes a first validation of the model performance with hard-coded transition. In addition, the robustness of the LWM with respect to the height of extraction $x_n = h_{w,p}$ is demonstrated by showing that the pressure distribution around the airfoil is only slightly influenced by the wall distance x_n. Lastly, a comparison of the HWM with a fully turbulent modeling using the GWF highlights the significant gain of accuracy in friction estimate provided by the LWM in the laminar part.

Next, the study of the A-airfoil in C3 configuration and with hard-coded transition also shows a good match in terms of wall-shear stress and pressure distribution with respect to the empirical data on the suction side, despite a slight underestimation of the pressure suction peak. It therefore seems relevant to go a step further by considering the same setup, but with transition detection. To that end, the sensor is analyzed in simulations with hard-coded transition. This reveals that the characteristic averaging time T has to be large enough to correctly capture the mean flow and related fluctuations, but on the other hand, has to be limited to obtain a converged sensor distribution in an acceptable computational time. In addition, this analysis enables to deduce that considering $T = c/U_\infty$ and $s_{\mathrm{w,thr}} = 2$ leads to a transition region on the suction side which is in line with the experiment. On this basis, a simulation with transition detection is carried out with the latter values, leading to a friction distribution that corresponds relatively well with the empirical one on the suction side. On the pressure side no transition is predicted. Due to the lack of high-fidelity data,

it is not possible to draw any reliable conclusions, but the absence of transition appeared surprising for the considered flow conditions. One plausible explanation would be mesh coarseness, probably more acceptable on the suction side due to the adverse pressure gradient leading to more developed turbulent structures and a larger boundary layer.

Lastly, the C13 configuration with hard-coded transition is considered in order to bring out the limitations of the HWM. Relying on the reference solution, such a flow presents a laminar separation bubble followed by a turbulent reattachment. Due to the self-similarly assumption, the LWM is not able to predict flow separation. Instead, a fully attached flow is predicted in the laminar region, leading to an overestimation of the wall-shear stress. On the other hand, the study of the friction on the pressure side reveals a discontinuity caused by the offset between the empirical stagnation point used during the reinitialization process and the actual one. More globally, such an offset affects the Falkner-Skan wall-shear stress estimate on both faces since $\tau_{w,FS} \sim \sqrt{1/x_s}$. To avoid this, it would be necessary to directly determine the stagnation points from the velocity field and compute the level-set function accordingly.

Finally, a simulation with transition detection is carried out with the sensor parameters determined from the study of the C3 configuration. The results indicate a case dependence with respect to the imposed threshold $s_{\mathrm{w,thr}}$. For the C13 case, a larger value would have been more suitable to obtain a better correspondence with the experiment. To overcome this, it would be pertinent to carry out a rigorous analysis of the sensor distribution with respect to the Reynolds number, the flow inclination and the mesh resolution in order to get a better understanding of the evolution of the suitable threshold $s_{\mathrm{w,thr}}$ enabling a good match with the corresponding reference transition location.

In all three cases studied, the instantaneous velocity fields show upstream velocity fluctuations, the existence of which seems to be due to the incompressibility assumption. Given that a central non-dissipative spatial discretization scheme is employed, the latter are conserved and transported up to the wall vicinity, which impacts the sensor prediction. Nevertheless, the study of the NACA0012 shows that a mesh refinement enables to strongly reduce their amplitude. As a second general observation, all pressure and friction distributions present wiggles. The main reason seems to be the trilinear interpolation process of the pressure and of the velocity input data at the extraction points. It would be interesting to verify these words by using a higher-order interpolation process.

Overall, the validity and the accuracy of the LWM are demonstrated for the Hiemenz flow and for the self-similar region of the flat plate downstream of its leading edge. For a flow over an extruded wing, the HWM with hard-coded transition shows a good match with the experimental data in the case of a fully attached flow at low inclination and this, despite a coarse grid. An improvement of the LWM would be, nevertheless, interesting to be able to capture the laminar separation bubble commonly encountered at high angles of attack. Subsequently, the sensor is able to predict a turbulent region corresponding relatively well with the experiment, provided a sufficiently fine mesh and a suitable threshold $s_{\mathrm{w,thr}}$ are used. The number of test cases investigated in this work is not sufficient to give a reference value $s_{\mathrm{w,thr}}$ for a given interval of Reynolds numbers, inclinations and mesh resolutions. Further investigations concerning these three parameters would therefore be necessary to overcome this lack of knowledge and to obtain a better robustness in the case of an extruded wing. In addition, such a sensor sensitivity with respect to the imposed threshold questions its applicability to more complex configurations. For instance, considering a simple aircraft or even a twisted wing, finding a suitable overall threshold value seems impossible due to the various flow conditions. It would be relevant to explore other possibilities to predict the local type of regime to gain in generality.

Bibliography

[1] D.R. Chapman. "Computational aerodynamics development and outlook". In: *AIAA J.* 17 (1979), pp. 1293–1313.

[2] U. Piomelli. "Wall-layer models for large-eddy simulations". In: *Progress in Aerospace Sciences* 44 (2008), pp. 437–446.

[3] U.J. Larsson, S. Kawai, J. Bodart, and I. Bermejo-Moreno. "Large eddy simulation with modeled wall-stress: recent progress and future directions". In: *Mechanical Engineering Reviews* 3.1 (2015).

[4] S. Hickel, E. Touber, J. Bodart, and J. Larsson. "A parametrized non-equilibrium wall-model for large-eddy simulations". In: *Proceedings of the 2012 Summer Program, Center for Turbulence Research, Stanford University* (2012).

[5] J.S. Baggett. "On the feasibility of merging LES with RANS in the near-wall region of attached turbulent flows". In: *Annual research briefs, Center for Turbulence Research. Stanford, CA: Stanford University* (1998), pp. 267–77.

[6] U. Piomelli, E. Balaras, H. Pasinato, K.D. Squires, and P.R. Spalart. "The inner-outer layer interface in large-eddy simulations with wall-layer models". In: *Int J Heat Fluid Flow* 24 (2003), pp. 538–550.

[7] A. Keating and U. Piomelli. "A dynamic stochastic forcing method as a wall-layer model for large-eddy simulation". In: *J Turbul* 7.12 (2006), pp. 1–24.

[8] S. Radhakrishnan, U. Piomelli, A. Keating, and A. Silva Lopes. "Reynolds-averaged and large-eddy simulations of turbulent non-equilibrium flows". In: *J Turbul* 7.63 (2006), pp. 1–30.

[9] J. Slotnick, A. Khodadoust, J. Alonso, and D. Darmofal. "CFD Vision 2030 Study: A Path to Revolutionary Computational Aerosciences". In: *NASA/CR-2014- 218178* (2014).

[10] H. Choi and P. Moin. "Grid-point requirements for large eddy simulation: Chapman's estimates revisited". In: *Phys. Fluids* 24.011702 (2012).

[11] C.A. Gonzalez, M. Karp, and P. Moin. "Wall-stress modeling for laminar boundary layers in coarse grids". In: *Annual Research Briefs* (2020).

[12] K. Goc, S. Bose, and P. Moin. "Wall-modeled large eddy simulation of an aircraft in landing configuration". In: *AIAA Paper* (2020), pp. 2020–3002.

[13] E. Dauricio and J. Azevedo. "A Wall Model for External Laminar Boundary Layer Flows Applied to the Wall-Modeled LES Framework". In: *Journal of Computational Physics* (2022).

[14] P. Petersson. *Laser Diagnostics Applied to Lean Premixed Swirling Flames - Simultaneous Flow Field and Scalar Measurements. [Doctoral Thesis (compilation), Combustion Physics].* Lund University: Division of Combustion Physics, Department of Physics, 2014.

[15] S.B. Pope. *Turbulent Flows.* 1st ed. Cambridge, GB: Cambridge University Press, 2000.

[16] M. Labois and D. Lakehal. "Very-Large Eddy Simulation (V-LES) of the flow across a tube bundle". In: *Nuclear Engineering and Design* 241 (2011), pp. 2075–2085.

[17] F. Ries. "Numerical Modeling and Prediction of Irreversibilities in Sub- and Supercritical Turbulent Near-Wall Flows". In: (2018).

[18] J. Smagorinsky. "General Circulation Experiments with the Primitive Equations". In: *Monthly Weather Review* 91.3 (1963), pp. 99–164.

[19] F. Ducros, F. Nicoud, and T. Poinsot. "Wall-Adapting Local Eddy-Viscosity Models for Simulations in Complex Geometries". In: *Numerical Methods for Fluid Dynamics VI* (1998), pp. 293–299.

[20] Z.L. Chen, S. Hickel, A. Devesa, J. Berland, and N.A. Adams. "Wall modeling for implicit large-eddy simulation and immersed-interface methods". In: *Theor. Comput. Fluid Dyn.* (2013).

[21] C. Fureby and F.F. Grinstein. "Large eddy simulation of high-Reynolds number free and wall-bounded flows". In: *J. Comput. Phys.* 181 (2002), pp. 68–97.

[22] F. Grinstein, L. Margolin, and W. Rider. *Implicit large eddy simulation*. Cambridge, GB: Cambridge University Press, 2007.

[23] S. Hickel, N.A. Adams, and J.A Domaradzki. "An adaptive local deconvolution method for implicit LES". In: *J. Comput. Phys* 213 (2006), pp. 413–436.

[24] S. Stolz and N.A. Adams. "An approximate deconvolution procedure for large-eddy simulation". In: *Phys. Fluids* 11.4 (1999), pp. 1699–1701.

[25] S. Hickel and N.A. Adams. "On implicit subgrid-scale modeling in wall-bounded flows". In: *Phys. Fluids* 19 (2007), p. 105106.

[26] S. Hickel and N.A. Adams. "Implicit LES applied to zero-pressure-gradient and adverse-pressure-gradient boundary-layer turbulence". In: *Int. J. Heat Fluid Flow* 29.3 (2008), pp. 626–639.

[27] E. Balaras and C. Benocci. "Subgrid-scale models in finite-difference simulations of complex wall bounded flows". In: *AGARD CP* 551 (1994), pp. 2.1–5.

[28] Z.L. Chen, S. Hickel, A. Devesa, J. Berland, and N.A. Adams. "Wall modeling for implicit large-eddy simulation and immersed-interface methods". In: *Theor. Comput. Fluid Dyn.* 28 (2014), pp. 1–21.

[29] T. von Karman. "Mechanische Ähnlichkeit und Turbulenz". In: *Nachrichten von der Gesellschaft der Wissenschaften zu Göttingen, Fachgruppe 1 (Mathematik)* 5 (1930), pp. 58–76.

[30] I. Bermejo-Moreno, L. Campo, J. Larsson, J. Bodart, D. Helmer, and J.K. Eaton. "Confinement effects in shock wave/turbulent boundary layer interactions through wall-modeled large-eddy simulations". In: *J. Fluid Mech.* 758 (2014), pp. 5–62.

[31] E. Balaras, C. Benocci, and U. Piomelli. "Two-Layer Approximate Boundary Conditions for Large-Eddy Simulations". In: *AIAA J.* 34.6 (1996), pp. 1111–1119.

[32] P. Catalano, M. Wang, G. Iaccarino, and P. Moin. "Numerical simulation of the flow around a circular cylinder at high reynolds numbers". In: *Int. J. Heat Fluid Flow* 24 (2003), pp. 463–469.

[33] M. Wang and P. Moin. "Dynamic wall modeling for large-eddy simulation of complex turbulent flows". In: *Phys. Fluids* 14.7 (2002), pp. 2043–2051.

[34] A. Frère, K. Hillewaert, P. Chatelain, and G. Winckelmans. "High Reynolds Number Airfoil: From Wall-Resolved to Wall-Modeled LES". In: *Flow, Turbulence and Combustion* 101 (2018), pp. 457–476.

[35] F. Örley, V. Pasquariello, S. Hickel, and N.A. Adams. "Cut-element based immersed boundary method for moving geometries in compressible liquid flows with cavitation". In: *J. of Computational Physics* 283 (2015), pp. 1–22.

[36] C.S. Peskin. "Flow patterns around heart valves: a numerical method". In: *J. Comput. Phys.* 10.2 (1972), pp. 252–271.

[37] R. Mittal and G. Iaccarino. "Immersed boundary methods". In: *Annu. Rev. Fluid Mech.* 37.1 (2005), pp. 239–261.

[38] C.S. Peskin. "The immersed boundary method". In: *Acta Numer.* 11 (2002), pp. 479–517.

[39] B.E. Griffith and C.S. Peskin. "On the order of accuracy of the immersed boundary method: higher order convergence rates for sufficiently smooth problems". In: *J. Comput. Phys.* 208.1 (2005), pp. 75–105.

[40] A.M. Roma, C.S. Peskin, and M. Berger. "An adaptive version of the immersed boundary method". In: *J. Comput. Phys.* 153.2 (1999), pp. 509–534.

[41] E.A. Fadlun, R. Verzicco, P. Orlandi, and J. Mohd-Yusof. "Combined immersed-boundary finite-difference methods for three-dimensional complex flow simulations". In: *J. Comput. Phys.* 161.1 (2000), pp. 35–60.

[42] J. Kim, D. Kim, and H. Choi. "An immersed-boundary finite-volume method for simulations of flow in complex geometries". In: *J. Comput. Phys.* 171.1 (2001), pp. 132–150.

[43] S. Kang, G. Iaccarino, and P. Moin. "Accurate immersed-boundary reconstructions for viscous flow simulations". In: *AIAA J.* 47.7 (2009), pp. 1750–1760.

[44] J. Mohd-Yusof. "Combined Immersed-Boundary/B-Spline Methods for Simulations of Flow in Complex Geometries". In: *Technical Report, NASA ARS/Stanford University CTR, Stanford* (1997).

[45] R. Verzicco, J. Mohd-Yusof, P. Orlandi, and D. Haworth. "LES in complex geometries using boundary body forces". In: *AIAA J.* 38 (2000), pp. 427–433.

[46] D.K. Clarke, H. Hassan, and M. Salas. "Euler calculations for multielement airfoils using Cartesian grids". In: *AIAA J.* 24.3 (1986), pp. 353–358.

[47] R. Gaffney Jr. and H.A. Hassan. "Euler calculations for wings using Cartesian grids". In: *25^{th} AIAA Aerospace Sciences Meeting* (1987).

[48] T. Ye, R. Mittal, H. Udaykumar, and W. Shyy. "An accurate Cartesian grid method for viscous incompressible flows with complex immersed boundaries". In: *J. Comput. Phys.* 156.2 (1999), pp. 209–240.

[49] S.A. Bayyuk, K. Powell, and B. Van Leer. "A simulation technique for 2-D unsteady inviscid flows around arbitrarily moving and deforming bodies of arbitrary geometry". In: *AIAA Paper 93-3391-CP* (1999).

[50] M. Kirkpatrick, S. Armfield, and J. Kent. "A representation of curved boundaries for the solution of the Navier-Stokes equations on a staggered three-dimensional Cartesian grid". In: *J. Comput. Phys.* 184.1 (2003), pp. 1–36.

[51] R.B. Pember, J.B. Bell, P. Colella, W.Y. Curtchfield, and M.L. Welcome. "An adaptive Cartesian grid method for unsteady compressible flow in irregular regions". In: *J. Comput. Phys.* 120.2 (1994), pp. 278–304.

[52] P. Colella, D.T. Graves, B.J. Keen, and D. Modiano. "A Cartesian grid embedded boundary method for hyperbolic conservation laws". In: *J. Comput. Phys.* 211.1 (2006), pp. 347–366.

[53] X.Y. Hu, B.C. Khoo, N.A. Adams, and F.L. Huang. "A conservative interface method for compressible flows". In: *J. Comput. Phys.* 219.2 (2006), pp. 553–578.

[54] E. Lauer, X.Y. Hu, S. Hickel, and N.A. Adams. "Numerical modelling and investigation of symmetric and asymmetric cavitation bubble dynamics". In: *Comput. Fluids.* 69 (2012), pp. 1–19.

[55] M. Meyer, A. Devesa, S. Hickel, X.Y. Hu, and N.A. Adams. "A conservative immersed interface method for Large-Eddy Simulation of incompressible flows". In: *J. Comput. Phys.* 229.18 (2010), pp. 6300–6317.

[56] M. Meyer, S. Hickel, and N.A. Adams. "Assessment of implicit large-eddy simulation with a conservative immersed interface method for turbulent cylinder flow". In: *Int. J. Heat Fluid Flow* 31.3 (2010), pp. 368–377.

[57] K. Duraisamy, P. R. Spalart, and C. L. Rumsey. "Status, Emerging Ideas and Future Directions of Turbulence Modeling Research in Aeronautics". In: *NASA/TM–2017–219682* (2017).

[58] R.H. Bush, T. Chyczewski, K. Duraisamy, B. Eisfeld, C.L. Rumsey, and B.R. Smith. "Recommendations for Future Efforts in RANS Modeling and Simulation". In: *NASA/TM–2017–219682* (2017).

[59] E. Lauer. "Numerical simulation and investigation of high-speed bubble-dynamics in cavitating flow". In: (2013).

[60] V. Pasquariello, G. Hammerl, F. Örley, S. Hickel, C. Danowski, A. Popp, W. A. Wall, and N. A. Adams. "A cut-cell finite volume–finite element coupling approach for fluid–structure interaction in compressible flow". In: *Journal of Computational Physics* 307 (2016), pp. 670–695.

[61] A.O. Başkaya, M.C. Capriati, D. Ninni, F. Bonelli, G. Pascazio, A. Turchi, T. Magin, and S. Hickel. "Verification and Validation of Immersed Boundary Solvers for Hypersonic Flows with Gas- Surface Interactions". In: *AIAA AVIATION 2022 Forum* 307 (2022), pp. 670–695.

[62] Delft High Performance Computing Centre (DHPC). *DelftBlue Supercomputer (Phase 1)*. https://www.tudelft.nl/dhpc/ark:/44463/DelftBluePhase1. 2022.

[63] C.-W. Shu. "Total-variation-diminishing time discretizations". In: *SIAM J. Sci. Stat. Comput.* 9.6 (1998), pp. 1073–1084.

[64] F.H. Harlow and J.E. Welsh. “Numerical calculation of time dependent viscous incompressible flow with free surface”. In: *Phys. Fluids* 8 (1965), pp. 2182–2189.

[65] A. Asaithambi. “Solution of the Falkner–Skan equation by recursive evaluation of Taylor coefficients”. In: *J. Comput. Appl. Math* 176 (2005), pp. 203–214.

[66] J. Zhang and B. Chen. “An iterative method for solving the Falkner–Skan equation”. In: *Applied Mathematics and Computation* 210 (2009), pp. 215–222.

[67] J.R. Dormand and P.J. Prince. “A family of embedded Runge-Kutta formulae”. In: *J. Comp. Appl. Math* 6 (1980), pp. 19–26.

[68] L.F. Shampine and H.A. WATTS. “Global error estimation for ordinary differential equations”. In: *ACM TOMS* 2.2 (1976), pp. 172–186.

[69] L.F. Shampine and M.W. Reichelt. “The MATLAB ODE Suite”. In: *SIAM Journal on Scientific Computing* 18 (1997), pp. 1–22.

[70] A.A. Salama. “Higher-order method for solving free boundary-value problems”. In: *Numer. Heat Transfer, Part B: Fund* 45 (2004), pp. 385–394.

[71] I.G. Currie. *Fundamental Mechanics of Fluids*. 4th ed. Boca Raton: CRC Press, 2012.

[72] D.F. Rogers. *Laminar Flow Analysis*. Cambridge, GB: Cambridge University Press, 1992.

[73] H. Schlichting. *Boundary-Layer Theory*. 7th ed. New York, U.S.A.: McGraw Hill, 1979.

[74] G.K. Batchelor. *An Introduction to Fluid Dynamics*. Cambridge, GB: Cambridge University Press, 1967.

[75] *STL (STereoLithography) File Format Family*. https://www.loc.gov/preservation/digital/formats/fdd/fdd000504.shtml. Accessed: 2023-04-05.

[76] J.A. Sethian. *Level set methods and fast marching methods : evolving interfaces in computational geometry, fluid mechanics, computer vision, and materials science*. 2nd ed. Cambridge, GB: Cambridge University Press, 1999.

[77] R. Kimmel and J.A. Sethian. “Computing geodesic paths on manifolds”. In: *Proc. Natl. Acad. Sci. USA.* (1998), pp. 8431–8435.

[78] K. Crane, C. Weischedel, and M. Wardetzky. “Geodesics in heat: A new approach to computing distance based on heat flow”. In: *ACM Trans Graph* 32.5 (2013), 152:1–152:11.

[79] S. Osher and C.W. Shu. “High order essentially non-oscillatory schemes for Hamilton- Jacobi equations”. In: *SIAM J. Numer. Anal.* 28 (1991), pp. 902–921.

[80] C. Mancinelli, M. Livesu, and E. Puppo. “A Comparison of Methods for Gradient Field Estimation on Simplicial Meshes”. In: *Computers & Graphics* (2019).

[81] C.D. Correa, K. Ma, and R. Hero. “A comparison of gradient estimation methods for volume rendering on unstructured meshes”. In: *IEEE Transactions on Visualization and Computer Graphics* 17 (2019), pp. 305–319.

[82] E. Sozer, C. Brehm, and C.C. Kiris. “Gradient Calculation Methods on Arbitrary Polyhedral Unstructured Meshes for Cell-Centered CFD Solvers”. In: *AIAA Journal* (2014).

[83] G. Thrmer and C.A. Wthrich. “Normal computation for discrete surfaces in 3d space”. In: *Computer Graphics Forum* 16.3 (1997), pp. C15–C26.

[84] C. Geuzaine and J.-F. Remacle. “Gmsh: a three-dimensional finite element mesh generator with built-in pre- and post-processing facilities”. In: *International Journal for Numerical Methods in Engineering* 79.11 (2009), pp. 1309–1331.

[85] T.-H. Shih, L.A. Povinelli, and N.-S Liu. “Application of generalized wall function for complex turbulent flows”. In: *Journal of Turbulence* 4.015 (2003).

[86] J. Bodart and J. Larsson. “Sensor-based computation of transitional flows using wall-modeled large eddy simulation”. In: *Center for Turbulence Research Annual Research Briefs* (2012).

[87] C. Meneveau, T.S. Lund, and W.H. Cabot. “A Lagrangian dynamic subgrid-scale model of turbulence”. In: *J. Fluid Mech.* 319 (1996), pp. 353–385.

[88] *Xfoil documentation, Description*. https://web.mit.edu/drela/Public/web/xfoil/xfoil_doc.txt. Accessed: 2023-04-04.

[89] J.V. Becker. "Boundary-Layer Transition on the NACA 0012 and 23012 Airfoils in the 8-Foot High-Speed Wind Tunnel". In: *National Advisory Committee for Aeronautics, Special Report* 137 (1940).

[90] W. Haase, F. Brandsma, E. Elsholz, M. Leschziner, and D. Schwamborn. "EUROVAL: A European Initiative on Validation of CFD Codes." In: *Notes on Numerical Fluid Mechanics* 42 (1993).

[91] W. Haase, E. Chaput, E. Elsholz, M. Leschziner, and U. Miiller. "ECARP - European Compuational Aerodynamics Research Projects: Validation of CFD-codes and Assessment of Turbulence Models". In: *Vieweg Verlag* 58 (1997).

[92] R. Houdeville, O. Piccin, and D. Cassoudesalle. "Opération décrochage — Mesures de frottements sur profils AS239 et AS240 à la soufflerie F1 du CFM". In: *RT-DERAT* 19.5025 (1987).

[93] *$k-\varepsilon$/Chien model, Description*. https://turbmodels.larc.nasa.gov/ke-chien.html. Accessed: 2023-02-06.

[94] *Parallax project, Description*. https://www.kbwiki.ercoftac.org/w/index.php/UFR_2-05_Test_Case. Accessed: 2023-02-05.

[95] Vincent Terrapon. "Lecture 8 of the Aerodynamics course at Uliège". In: (2022).

[96] F.H. Abernathy. "Film Notes for Fundamentals of Boundary Layers". In: (1970).

[97] L. Davidson, D. Cokljat, J. Frohlich, M.A. Leschziner, C. Mellen, and W. Rodi. "LESFOIL: Large Eddy Simulation of Flow Around a High Lift Airfoil". In: *Notes on Numerical Fluid Mechanics and Multidisciplinary Design (NNFM)* 83 (2003).

[98] Y. Tamaki, Y. Fukushima, Y. Kuya, and S. Kawai. "Large-eddy simulation of airfoil flows at near-stall conditions using equilibrium/non-equilibrium wall models". In: *AIAA SciTech Forum* (2019).